UNIVERSIDAD COMPLUTENSE DE MADRID

FACULTAD DE CIENCIAS FÍSICAS
Departamento de Física de Materiales

NEGATIVE AND ANOMALOUS REFRACTION IN METAMATERIALS AND PHOTONIC CRYSTALS.

MEMORIA PARA OPTAR AL GRADO DE DOCTOR

PRESENTADA POR

Juan Luis García Pomar

Bajo la dirección del doctor

Manuel Nieto Vesperinas

Madrid, 2009

- **ISBN:978-84-692-6015-9**

Negative and anomalous refraction in metamaterials and photonic crystals

A thesis presented

by

Juan Luis García Pomar

under the supervision of

Manuel Nieto Vesperinas

Profesor de Investigación

Instituto de Ciencia de Materiales de Madrid (CSIC)

to

Facultad de Ciencias Físicas

Departamento de Física de Materiales

Universidad Complutense de Madrid

Madrid 2008

A mis padres

Thesis advisor
Manuel Nieto Vesperinas

Author
Juan Luis García Pomar

Negative and anomalous refraction in metamaterials and photonic crystals

Abstract

Left handed materials, also called metamaterials because they are artificial and are not present in Nature, are characterized by having both permittivity and permeability negative. With these properties, metamaterials have a negative refractive index due to which they produce negative refraction making them good candidates to form images.

However, since their early fabrication in the microwave range, losses in metamaterials have been considerable, thus being their refractive and image formation properties highly affected by them.

In the first chapter of this thesis I overview and analyze the basic characteristics and properties of the left handed materials, just likewise addressing progress to carry the negative refractive index into the optical range where losses are still the main problem for image formation and beam steering due to absorption within slabs of the order of the wavelength. I explain how physics imposes the existence of dispersion in these materials, with an intrinsic limit which gives a measure of losses as a result of causality and the Kramers−Kronig relations. For this reason, I have studied in Chapter 2 the influence of losses in the refraction of a prism of left-handed material by using numerical calculations based on finite elements, within a model of effective medium. I have found that in experiments of negative refraction in prisms both the scattering and edge diffractive effects are considerable since the size of the sample is of the order of the wavelength. Likewise I believe that these effects are suppressed by confining the prism sample between walls of absorbing material. Also, I have established a law of refraction bearing in mind the absorption observed in the experiments, though the change of the angle of refraction is insignificant when losses are considered, we observe that the wave inside the metamaterial is in general inhomogeneous, thus being more accurate to calculate the angle of refraction from the planes of constant phase.

Later, I analyze image formation through a slab of material. In this case, I observe changes in the position and spot size of the focus when the imaginary part of the index of refraction (losses) and the impedance of the metamaterial varies. This is of substantial consequence for future experimental works. On the other hand, in order to study imaging quality and thus the spatial invariance of the system, I have analyzed the transfer function of metamaterial slabs, verifying that the results agree with the early theory proposed on the basis of geometrical optics. Finally, I undertake a numerical systematic study by varying both real and imaginary parts of the index of refraction with respect to the ideal value -1, thus assessing how this affects the

image of an extended object and showing that the resolution deteriorates. The best resolution being for the cases in which $n_1 < -1$, n_1 being the real part of the index of refraction, rather than for those cases of $n_1 > -1$.

A possibility to avoid the problem of losses, due to the metallic character of the metamaterials, is to obtain negative refraction by using photonic crystals based on dielectric materials. A photonic crystal is a material consisted of dielectric or metallic structures placed periodically. Nevertheless, photonic crystals and metamaterials have several differences, since for the former the theory of effective medium is not valid and the process turns out to be diffractive as the wavelength is of the order of the lattice parameter. A way to examine the process of refraction by a photonic crystal is observing the isofrequency lines which yield the permitted $\vec{k}$ wavevectors. The isofrequency line provides the group velocity which is perpendicular to it and appears according to the gradient of the dispersion curve. To analyze the process of image formation produced by these systems, we have studied imaging of extended objects in some two-dimensional structures of photonic crystal slabs. By means of an analysis of the transfer function we have demonstrated that this system is isoplanatic, although the image suffers aberrations due to the distortions of the isofrequency lines with respect to a perfect circumference. This leads to a dependence of the refraction with the angle of incidence. We have compared the width of the transfer function in photonic crystals with that of quasi-ideal left−handed materials observing such lack of superresolution in photonic crystals. Finally, we show that the condition for the existence of surface waves which might lead to superresolution is that the wavevector follow the hyperbolic profile of the correct isofrequency in the complex space, and the experimental conditions must be in the electrostatic limit. This actually is impossible to reach since the lattice parameter is of the order of the wavelength, and, therefore, the dispersion relation does not reach an enough width spectrum of transversal wavevectors. In spite of this, the preliminary works on negative refraction in photonic crystals claimed superresolution in the images however, in Chapter 4, I demonstrate that the results obtained in these works involve a wrong interpretation and actually the output intensity distributions are a combination of two effects: self-waveguiding and field concentration in the dielectric cylinders. Self-waveguiding in a photonic crystal is due to anomalous refraction provided by the flat zone of the isofrequency line, which makes the group velocity of most of the permitted wavevectors in the photonic crystal to point in the ΓK direction. The field concentration in the cylinders is due to an operation in the first band of the gap and to the high dielectric index. Hence,I have proved in several examples that the early interpretation of superresolution is an artifact, it is actually due to a superconcentration of the self−waveguided field in the surface elements close to the exit interface. With these sequence of we have proposed an alternative use of these structures where Gaussian beams are waveguided, bent and splitted by means of diffraction as a consequence of the isofrequency lines. We study a new phenomenon: The beam shift in the total internal reflection in a self-waveguiding photonic crystal. For this study, I have per-

formed an experiment in the microwave range for a two−dimensional photonic crystal composed of a square lattice of cylinders of flint glass. This total internal reflection is produced at an unique angle (45°) due to the crystal symmetry and to the higher Bragg orders. This shift depends on the permitted surface mode. Another point of view interprets it based on the truncation of the cylinders in the exit interface. This varies the dispersion relation of the evanescent surface modes. Finally I have proposed an application of these two effects using the system as a scanning device or as a subwavelength superconcentrator.

Another way to overcome the problem of losses is coupling a gain medium. In Chapter 5 I have discussed and analyzed an intuitive model of the resonance of a metamaterial (bosonic system) connected by means of the interactions of the local fields to a resonance of a gain medium consisting of a system of two levels (fermionic system). By applying this model, I have obtained the electric susceptibility fruit of the coupling which allows us to calculate the transmission and reflection coefficients of the system. In addition, by an analogy to a classic system consistily of a split ring resonator and a dispersive Lorenzt medium with gain we can compare the linear response of the system calculated with the model to that numerically calculated with finite elements in the time domain. From the model we also calculate the stationary state of the system of profit and the stationary value for the occupation. In this respect, we analyze the interesting dynamics of the model, similar to that of a laser, finding the necessary pumping in order that the system behaves like a laser and the stationary values of polarizations and occupation.

Finally, in Chapter 6 I have carried out a study based on an analogy of the theory applied to photonic crystals with that of a two-dimensional system of electrons: graphene. This material is a two-dimensional crystal consisting of a hexagonal lattice of carbon atoms. Its band structure at low energy and in filled situation is described by Dirac's equation without mass. As a consequence, a great deal of the electronic and transport properties of this system are different from those of semiconductors of usual dimensionality. Three properties turn out to be important: 1) the conical bands with a junction point (Dirac's point) between the band of hollows and the band of electrons, 2) the great transmission of electrons in $p-n$ junctions due to the conservation of "chirality", and 3) the separation of electrons in valley K and K' and its break of symmetry at high energies. The conical bands of graphene give rise to negative refraction of electrons in a $p-n$ junction. $p-n$ junctions can be obtained placing on the graphene a metallic door (gold) that changes the chemical potential by field effect. If we raise the energy to higher values than 0.6 eV we will start obtaining a trigonal distortion that finally produce flat Fermi surfaces. Hereby, using the flat zones in this case of Fermi surfaces, we manage to separate two beams of electrons, each one corresponding to a valley. In this way, I propose an experimental device to obtaining polarized beams in the degree of freedom of valley using the trigonal distortion that appears at moderated energies in the π bands of graphene. My proposal simplifies previous works in which the geometry was considered to be special,

such geometries as an immersed contact in a band of finite thickness of graphene. This geometry has the principal disadvantage of being experimentally not realizable up to this date, since this device needs a concrete type of edges (edges in zigzag) that could contain zero modes, which generate an imbalance in the population of both cones and, therefore, of a polarized current in the valley. The proposal is to use as device an $n - p - n^{-}$ junction. This junction, easily obtainable experimentally, consists simply of a barrier of potential. The innovation is to consider in one of the sides of the barrier such a potential that the trigonal distortion of the band should be valuable. This distortion, due to considering the next term in the series expansion of the band of moments, makes that the surfaces of constant energy, which in case of Dirac were perfect circumferences, now possess triangular form, breaking the isotropy of the medium, and what is more interesting, making that the anisotropy in every cone be different. The transmission of electrons across the graphene in these conditions of selective anisotropy between valleys, makes that the transmitted current takes different directions for every valley, producing to them a phenomenon of separation of polarized beams in the valley; the angular separation of both beams, in the most favorable circumstance, being of approximately 20 degrees. The effect of separation of beams is not the only one that I find, since it depends on the relative orientation between the barrier of potential and the lattice. Another extreme effect, also consequence of the different form of the surfaces of constant energy, consists of a collimation towards one of the two cones, and an angular dispersion of the bundle corresponding to the other cone. Though qualitatively the response of every cone in this case is very different due to the curvature of the Fermi surface and the necessary difference of energies between a part of the barrier and the other making that the curvature of Fermi surface in the zone of trigonal distortion (trigonal warping) be sufficiently small in order that this difference of effects is not very pronounced. To demonstrate this theory, at the end of the chapter I have realized numerical simulations in two-dimensional photonic crystals with dispersion bands similar to those of Dirac. In this way, within this optical analogy, I have simulated a $p - n$ junction using crystals with different index of refraction and I have verified the separation of beams and the collimation.

Resumen

Los materiales zurdos, también llamados metamateriales porque son de carácter artificial y no existen en la naturaleza, se caracterizan por tener tanto la permitividad dieléctrica como la permeabilidad magnética negativas. Con estas propiedades se consigue refracción negativa en los metamateriales lo cual los hacen unos buenos candidatos para la formación de imágenes.

Sin embargo, desde su temprana fabricación en el rango de microondas, las pérdidas en estos metamateriales han sido considerables, siendo la imagen resultante y las propiedades refractivas seriamente afectadas.

En el primer capítulo de esta tesis analizamos las características y propiedades de los materiales zurdos así como los progresos que se han hecho para llevar el índice de refracción negativo hasta valores cercanos al rango óptico en donde todavía las pérdidas siguen siendo el principal problema en la formación de imágenes ya que la absorción sigue siendo bastante grande con rangos comparables a la longitud de onda. Explicamos la necesidad física de tener dispersión en estos materiales al igual que la existencia de un límite intrínseco al valor de pérdidas en un material zurdo debido a la causalidad derivada de las relaciones de Kramers−Kronig.

Por ese motivo hemos estudiado en el capítulo 2 la influencia de las pérdidas en la refracción de un prisma de material zurdo usando cálculos numéricos de elementos finitos bajo un modelo de medio efectivo. Hemos encontrado que en el experimento de refracción negativa por un prisma los efectos de borde y difractivos son considerables al ser el tamaño de la muestra del orden de la longitud de onda, asimismo encontramos que estos efectos son suprimidos si emparedamos el prisma entre paredes de material absorbente. También hemos establecido una ley de refracción teniendo en cuenta la absorción que se observa en los experimentos, si bien la variación del ángulo de refracción es insignificante con la introducción de pérdidas, sí observamos que la onda a la salida es en general inhomogénea y es más exacto calcular el ángulo de refracción observando los planos de fase constante.

Posteriormente, analizamos la formación de imagen a través una lámina plana de material. En este caso, observamos como varía la posición del foco y su tamaño variando la parte imaginaria del índice de refracción (pérdidas) así como la impedancia del metamaterial y como la variación tanto de tamaño como de profundidad son sustanciales y de considerable atención para futuros trabajos experimentales. Por otro lado, para estudiar la invariancia espacial del sistema hemos analizado la función de transferencia del metamaterial, comprobando que los resultados concuerdan con la teoría previamente propuesta. Por último, realizamos un estudio numérico sistemático de la variación de tanto la parte real e imaginaria del índice de refracción con respecto al valor de -1 viendo como es afectada la imagen de un objeto extenso mostrando como empeora la resolución según nos apartamos del valor $n = -1$ siendo la resolución mejor para los casos de $n_1 < -1$, siendo n_1 la parte real del índice de refracción, que

para los casos de $n_1 > -1$.

Una posibilidad para evitar el problema de las pérdidas, debido al carácter metálico de los metamateriales, es la utilización de cristales fotónicos con materiales dieléctricos para obtener refracción negativa. Un cristal fotónico es un material compuesto de estructuras dieléctricas situadas periódicamente. Sin embargo, los cristales fotónicos y los metamateriales tienen grandes diferencias, en este caso la teoría de medio efectivo deja de ser valida y el proceso pasa a ser difractivo ya que la longitud de onda es del orden del parámetro de red. Una forma de examinar el proceso de refracción en un cristal fotónico es atendiendo a la curva de dispersión que nos proporciona los vectores $\vec{k}$ permitidos dentro del cristal a una determinada frecuencia, llamada isofrecuencia. La isofrecuencia nos proporciona la velocidad de grupo, la cual es perpendicular a ésta y apunta según el gradiente de la curva de dispersión. Para analizar el proceso de formación de imagen producido por estos sistemas, hemos estudiado la propagación de objetos extensos en algunas estructuras bidimensionales de cristal fotónico. Por medio de un análisis de la función de transferencia hemos demostrado que el medio es isoplanático si bien la imagen formada sufre aberraciones debido a las imperfecciones que presentan las isofrecuencias con respecto a una circunferencia perfecta lo que conlleva una dependencia de la refracción con el ángulo. Hemos comparado los anchos de la función de transferencia de estos cristales fotónicos con los materiales zurdos con superresolución observando que en el caso de los cristales fotónicos estos carecen de ella. Finalmente, observamos que para que existan ondas superficiales en la superficie de salida del cristal fotónico que recuperen la imagen, el vector de onda debe seguir la correcta isofrecuencia hiperbólica en el plano complejo y las condiciones experimentales deberían estar dentro del límite electrostático cosa que no puede suceder por la propia limitación del parámetro de red que, como hemos dicho anteriormente, es del orden de la longitud de onda y por lo tanto en la relación de dispersión no se alcanza un espectro suficientemente amplio en los vectores de onda transversales. A pesar de lo indicado anteriormente, los primeros trabajos sobre refracción negativa en cristales fotónicos reclamaban haber conseguido superresolución en las imágenes obtenidas, sin embargo en el capítulo 4 demostramos que el resultado obtenido por estos trabajos fue una mala interpretación y realmente se trata de una superconcentración debido principalmente a dos efectos: el autoguiado y la concentración de campo en los cilindros dieléctricos. El autoguiado dentro del cristal fotónico se debe a la refracción anómala provocada por la forma plana de la isofrecuencia que hace que para la mayor parte de los vectores de onda permitidos dentro del cristal la velocidad de grupo que es perpendicular a la isofrecuencia apunte en la dirección ΓK, y la concentración del campo en los cilindros se debe a que estamos operando en la primera banda y el material dieléctrico de alto índice de refracción concentra el campo eléctrico. Así hemos probado con varios ejemplos que la superresolución conseguida es en realidad una superconcentración del campo en los elementos de la intercara de salida. Hemos propuesto a estos efectos un uso alternativo donde conseguimos guiar y doblar haces Gaussianos dentro del cristal por medio de los fenómenos difractivos

derivados de la forma de las isofrecuencias, así como separar los haces en dos. Estudiamos un fenómeno nuevo: el desplazamiento del haz en la reflexión total interna de un cristal fotónico con autoguiado, el cual, en su mayor parte, es debido a los modos superficiales que se producen en la interfase. Para este estudio hemos propuesto y realizado un experimento en el rango de las microondas para un cristal bidimensional compuesto de cilindros de vidrio, cuyos resultados están muy próximos a los cálculos teóricos realizados. Esta reflexión total se produce sólo a un único ángulo (45°) debido a la simetría del cristal y a la refracción producida a otros ángulos por los diferentes órdenes de Bragg y el desplazamiento producido en la reflexión depende de los modos de superficie permitidos o lo que es lo mismo de la diferente cantidad truncada a los cilindros de la intercara que nos varía la dispersión de estos modos evanescentes de superficie. Finalmente, hemos sugerido aunar estos efectos y usar el sistema como una herramienta para el escaneado de superficies o para concentrar haces Gausianos por debajo de su longitud de onda.

Otra manera de intentar superar el problema de las pérdidas en los metamateriales es acoplarles un sistema con ganancia. Así pues, en el capítulo 5 hemos discutido y analizado un modelo intuitivo de la resonancia de un metamaterial (sistema bosónico) acoplado por medio de las interacciones de los campos locales a una resonancia de un medio de ganancia por un sistema de dos niveles. Aplicando este modelo hemos obtenido la susceptibilidad eléctrica fruto del acoplamiento, lo cual nos permite calcular la transmisión y la reflexión del sistema. Además haciendo una analogía con un sistema clásico compuesto de un resonador de anillo abierto y un medio tipo Lorenzt dispersivo con ganancia, podemos comparar la respuesta lineal del sistema calculado con el modelo al calculado numéricamente con elementos finitos en el dominio tiempo. A partir del modelo calculamos también el estado estacionario del sistema de ganancia y el valor estacionario para la ocupación. Con este respecto, analizamos la interesante dinámica del modelo, similar a la de un sistema láser, encontrando el bombeo necesario para que el sistema sea láser y los valores estacionarios de polarizaciones y ocupación.

Finalmente, en el capítulo 6 hemos realizado una analogía de la teoría aplicada en cristales fotónicos a un sistema bidimensional de electrones: el grafeno. El grafeno es un cristal bidimensional consistente en una red hexagonal de átomos de carbono. Su estructura de bandas a baja energía y en situación de medio llenado viene descrita por la ecuación de Dirac sin masa. Este hecho hace que gran parte de las propiedades electrónicas y de transporte que presenta este sistema sean diferentes a aquellas que se encuentran en los semiconductores de baja dimensionalidad usuales. Tres propiedades resultan muy importantes para el desarrollo efectuado: 1) las bandas cónicas con un punto de unión (punto de Dirac) entre la banda de huecos y de electrones, 2) la gran transmisión de electrones en uniones $p-n$ debido a la conservación de "quiralidad", y 3) la separación de electrones en valle K y K' y su ruptura de simetría a altas energías. Las bandas cónicas del grafeno hacen que en una unión $p-n$ se produzca refracción negativa de electrones. Las uniones $p-n$ se pueden conseguir situando

sobre el grafeno una puerta metálica (oro) que cambia el potencial químico por efecto campo. Si elevamos la energía a valores más altos de 0.6 eV empezaremos a obtener una distorsión trigonal que finalmente nos proporcionará superficies de Fermi planas. De esta manera, utilizando las zonas planas en este caso de las superficies (curvas) de Fermi conseguimos separar dos haces de electrones cada uno correspondiente a un valle. Así pues, proponemos un dispositivo experimental para la obtención de haces polarizado en el grado de libertad de valle empleando la distorsión trigonal que aparece a energías moderadas en las bandas π de grafeno. Nuestra propuesta simplifica la anterior en la que se consideraban geometrías especiales, tales como un contacto inmerso en una banda de espesor finito de grafeno. Esta geometría tiene el principal inconveniente de ser experimentalmente irrealizable a día de hoy, ya que este dispositivo necesita un tipo concreto de bordes (bordes zig-zag) que puedan contener modos cero, responsables de generar un desequilibrio en la población de ambos conos y por tanto, de una corriente polarizada en el valle. Nuestra propuesta es utilizar como dispositivo una unión $n-p-n^-$. Esta unión, fácilmente obtenible experimentalmente, consiste simplemente en una barrera de potencial. La novedad consiste en considerar en uno de los lados de la barrera un potencial tal que la distorsión trigonal de la banda sea apreciable. Esta distorsión, correspondiente a considerar el siguiente término en el desarrollo en serie de momentos de las bandas, hace que las superficies de energía constante, que en el caso de Dirac eran circunferencias perfectas, ahora posean forma triangular, rompiéndose la isotropía del medio, y lo que es más interesante, la anisotropía en cada cono es diferente. La transmisión de electrones a través del grafeno en estas condiciones de anisotropía selectiva entre valles hace que la corriente transmitida tome direcciones diferentes para cada valle, produciéndose un fenómeno de separación de haces polarizados en el valle, siendo la separación angular de ambos haces, en la circunstancia más favorable, de aproximadamente 20 grados. El efecto de separación de haces no es el único que encontramos, ya que depende de la orientación relativa entre la barrera de potencial y la red. El otro efecto extremo, también consecuencia de la distinta forma de las superficies de energía constante, consiste en una colimación hacia delante de uno de los dos conos, y una dispersión angular del haz correspondiente al otro cono. Aunque cualitativamente la respuesta de cada cono en este caso sea muy diferente, al estar ligada a la curvatura de la superficie de Fermi, la diferencia de energías necesaria entre una parte de la barrera y la otra hace que la curvatura de la superficie de Fermi en la zona de distorsión trigonal sea lo suficientemente pequeña como para que esta diferencia de efectos no sea muy pronunciada. Para demostrar esta teoría, al final del capítulo hemos realizado simulaciones numéricas a cristales fotónicos bidimensionales con bandas de dispersión similares a las de Dirac. Así, dentro de esta analogía óptica, hemos simulado una unión $p-n$ usando cristales con diferente índice de refracción y hemos comprobado la separación de haces y la colimación.

Contents

Citations to Work of this Thesis Previously Published

The main contents of this thesis can be found in the following publications:

- **Chapter 2**
  - J.L. Garcia-Pomar and M. Nieto-Vesperinas *Transmission study of prisms and slabs of lossy negative index media*, Optics Express **12**,2081 (2004)
  - J.L. Garcia-Pomar and M. Nieto-Vesperinas *Imaging of extended objects by a negative refractive index slab*, New Journal of Physics **7** 160 (2005)
  - J.L. Garcia-Pomar and M. Nieto-Vesperinas *Imaging properties of photonic crystals*, Optics Express, **15**, 7786, (2007)
- **Chapter 3**
  - J.L. Garcia-Pomar and M. Nieto-Vesperinas *Imaging properties of photonic crystals*, Optics Express, **15**, 7786, (2007)
- **Chapter 4**
  - J.L. Garcia-Pomar and M. Nieto-Vesperinas *Waveguiding, collimation and subwavelength concentration in photonic crystals*, Optics Express **13**; 7997, (2005)
  - J.L. Garcia-Pomar, J. Gollub, A. Thapa, D.R. Smith and M. Nieto-Vesperinas *Experimental visualization of total internal reflection beam lateral shift in a self-collimated photonic crystal*, (to be published)
  - J.L. Garcia-Pomar and M. Nieto-Vesperinas *Wave propagation in self-waveguiding and negative refracting photonic crystals*, Proc. of SPIE **6593**, 659317 (2007)
- **Chapter 5**
  - M. Wegener, J. L. Garcia-Pomar, C. M. Soukoulis, N. Meinzer, M. Ruther, S. Linden *Toy model for plasmonic metamaterial resonances coupled to two-level system gain*, arXiv:0809.0487v2 (Opt. Express in press)
- **Chapter 6**
  - J.L. Garcia-Pomar, A. Cortijo and M. Nieto-Vesperinas *Valley polarized electronic beam splitting in graphene*, Phys. Rev. Lett. **100**, 236801 (2008)

Acknowledgments

First at all, I would like to express my deepest gratitude to my advisor Manuel Nieto Vesperinas. I have been very privileged to have undoubtedly the most intuitive, with better knowledge about Optics and supportive advisor anyone could ask for. Manuel always found the time to discuss with me about my work. I have highly taken into account his wisdom advices which always are very estimate and useful. I have been stimulated and excited by his constant flow of good ideas.

In his group, I have always received help. Thanks to Suzana Sburlan, Raquel Gómez and specially Luis Blanco who always had time to spend in my problems and doubts and finally he became a great friend.

Throughout these year of PhD I have met good scientists. I am grateful to Carlos Pecharroman for introducing me in the finite element method. I am indebted to M.A.H. Vozmediano by her help an useful comments in the topic of graphene and Ramon Aguado by share his experience with us and finally to Alberto Cortijo my friend in the career, and my friend in the ICMM and finally a professional collaboration which is part of this thesis. I am sure that together new ideas and papers will come.

My fascination with the physical scientific career is undoubtedly due to my tutor María del Carmen Sánchez Trujillo. She gave me the opportunity of work in her lab in my last year in the university and she introduced me in the scientific research, also I must thank to the collaborators in her group C. Aroca and E. López and specially and with warm to Óscar de Abril and Lucas Pérez. Also, I want to thank to the department of Materials Physics at the Univerisdad Complutense de Madrid that gave me the possibility of making the PhD courses and to CSIC by the financial support.

I am also very grateful to my hosts during my foreign short stays: David R. Smith at Duke University in North Carolina and his collaborators Jack Mock, David Schurig and specially Marco Rahm who gave me friendly discussions about physics and soccer and I hope we could work together in THz optics. Finally, I want to thank to Jonah Gollub, I always remember how we made a photonic crystal with $20 and a lot of work and ingenious. And, also I am very grateful to Martin Wegener at Karlsruhe University who teach me another way to work and introduce me in Quantum Optics, and his group made me fell one more. I worked there with Stefan Linden, Nina Meinzer and Matthias Ruther, specially thank to the later we shared several conversations about the coupled model and we advanced together in the development of those.

I spend the mostly of my work in the department of Condensed Matter Theory Department at ICMM. I doubt I will ever again find a working place where I feel so comfortable. I could share my experience, my doubts and my feelings about my PhD with these friends. Thank you so much for everything Leni, Ana, Juan, Virginia, María, Rafas, Belén, Javi, David, Carlos, Fernandos, Samuel, Simone and María José.

I am grateful to my office mates by the great environment and good atmosphere. First, the "128's old boys" Ricardo, Ángel, Félix and César and the present "128's mates" Eduardo, María and specially I am deepest grateful to Débora who helped me with the text editor program, physical doubts about Quantum Optics and shared

with me great moments.

Finally, some words of acknowledgment to my family in my native language: Es un placer y un deber para mí dedicar esta tesis a mis padres y hermanas. Todo lo que soy y pueda llegar a ser algún día es gracias a mi familia. Sobre todo deseo expresar a mis padres que no hay forma de agradecer lo suficiente el cariño y atención que han mostrado a la hora de educarme y ofrecerme todas las oportunidades. Gracias.

Chapter 1

Properties of left handed materials

1.1 Motivation

Negative refraction in left handed materials (LHM's) constitutes a new and interesting physics area which covers several phenomena as dielectric and magnetic properties of those media, as well as consequences for imaging, superresolution, absorption, evanescent waves, diffraction, information processing by handling, surface waves as plasmons and polaritons. This subject has been a hot topic since their early design and fabrication [1]. In this chapter we will introduce the basic properties of LHM's and we shall present the background of the theory of negative refraction.

1.2 Introduction

In 1967 Veselago [2] theoretically studied the properties of a medium with dielectric permittivity ϵ and magnetic permeability μ both negative and, in consequence, negative refractive index n, (as we explain in section 1.3). Materials with this property are referred to as *doubly negative* by the double negativity of the permittivity and permeability , left handed materials (LHM), or simply as metamaterials, the last term connoting the fact that the only media known to have both $\epsilon < 0$ and $\mu < 0$ are purposefully fabricated rather than naturally occurring. The term LHM stems from the left-handed orientation of the triad: electric $\vec{E}$ and magnetic $\vec{H}$ field vectors and the wavevector $\vec{k}$. This is discussed next [3].

We will show that the double negative nature of the constitutive parameters, ϵ and μ, results in the propagation of electromagnetic waves exhibiting antiparallel phase and group velocities, namely, *left handed waves*. For this purpose, we start by writing

Maxwell's equations

$$\nabla \times \vec{E} = -\frac{\partial \vec{B}}{\partial t} - \vec{M}_s \tag{1.1}$$

$$\nabla \times \vec{H} = -\frac{\partial \vec{D}}{\partial t} - \vec{J}_s \tag{1.2}$$

$$\nabla \cdot \vec{D} = \rho_e \tag{1.3}$$

$$\nabla \cdot \vec{B} = \rho_m \tag{1.4}$$

where $\vec{E}$ (V/m) is the electric field vector, $\vec{H}$ (A/m) denotes the magnetic field vector, $\vec{D}$ (C/m^2) is the electric flux density, $\vec{B}$ (W/m^2) stands for the magnetic flux density, $\vec{M}_s$ (V/m^2) is the (fictitious) magnetic current density, $\vec{J}_s$ (A/m^2) is the electric current density, ρ_e (C/m^3) is the electric charge density, and ρ_m (C/m^3) is the (fictitious) magnetic charge density. In addition, if the medium is linear (ϵ,μ do not depend on $\vec{E}$ or $\vec{H}$) and in the approximation of either weakly dispersive, or nondispersive media (i.e. ϵ,μ not depending on ω), the vectors in the pairs $[\vec{D}, \vec{E}]$ and $[\vec{B}, \vec{H}]$ are related by the constitutive equations

$$\vec{D} = \epsilon_0 \vec{E} + \vec{P} = \epsilon_0 (1 + \chi_e) \vec{E} = \epsilon_0 \epsilon_r \vec{E} = \epsilon \vec{E} \tag{1.5}$$

$$\vec{B} = \mu_0 \vec{H} + \vec{M} = \mu_0 (1 + \chi_m) \vec{H} = \mu_0 \mu_r \vec{H} = \mu \vec{H} \tag{1.6}$$

where $\vec{P} = \epsilon_0 \chi_e$ and $\vec{M} = \mu_0 \chi_m$ are the electric and magnetic polarizations, respectively, χ_e and χ_m are the electric and magnetic susceptibilities, respectively, $\epsilon_0 = 8.854 \cdot 10^{12}$ (F/m) and $\mu_0 = 4\pi \cdot 10^7$ (H/m) are the permittivity and permeability of free space, respectively, and $\epsilon = \epsilon_0(1 + \chi_e)$ and $\mu = \mu_0(1 + \chi_m)$. The latter can be written in the form

$$\epsilon = \epsilon_1 + i\epsilon_2 \tag{1.7}$$

$$\mu = \mu_1 + i\mu_2 \tag{1.8}$$

Assuming harmonic fields with the time dependence $e^{-i\omega t}$ and defining the corresponding generic phasor $\vec{F}(r)$ as

$$\vec{F}(\vec{r}, t) = Re\left[F(\vec{r}) e^{-i\omega t}\right], \tag{1.9}$$

where F represents any of the physical quantities in Maxwell's equations, then these equations as well as the constitutive equations can be written as

$$\nabla \times \vec{E} = i\omega\mu\vec{H} - \vec{M}_s \tag{1.10}$$

$$\nabla \times \vec{H} = -i\omega\mu\vec{E} - \vec{J}_s \tag{1.11}$$

$$\nabla \cdot \vec{D} = \rho_e \tag{1.12}$$

$$\nabla \cdot \vec{B} = \rho_m \tag{1.13}$$

$$\tag{1.14}$$

and

$$\vec{D} = \epsilon\vec{E}, \tag{1.15}$$
$$\vec{B} = \mu\vec{H}, \tag{1.16}$$

respectively. Let us consider now the plane wave

$$\vec{E} = \vec{E}_0 e^{i\vec{\beta}\cdot\vec{r}} \tag{1.17}$$
$$\vec{H} = \frac{\vec{E}_0}{Z} e^{i\vec{\beta}\cdot\vec{r}} \tag{1.18}$$

where $Z = |E|/|H|$ denotes the wave impedance and $\beta = 2\pi/\lambda_0 n$. Because any of these physical quantities can be expressed as a superposition of plane wave components by means of the Fourier transform, the consideration of an isolated component will provide information on the fundamental response of the medium. This information is directly obtained by introducing the Fourier integral expressions into the first two Maxwell's equations. For simplicity, let us consider a lossless medium ($\epsilon_2 = \mu_2 = 0$) in regions without sources ($\vec{M}_s = \vec{J}_s = 0$). In the case of a right handed medium (RHM), $\epsilon, \mu > 0$, and therefore each component satisfies

$$\vec{\beta} \times \vec{E} = +\omega\mu\vec{H} \tag{1.19}$$
$$\vec{\beta} \times \vec{H} = -\omega\epsilon\vec{E} \tag{1.20}$$

which builds the familiar right-handed triad $(\vec{E}, \vec{H}, \vec{\beta})$ shown in Fig. 1.1 (a). By contrast, in the case of a LHM, $\epsilon, \mu < 0$, and since then $|\epsilon| = -\epsilon > 0$ and $|\mu| = -\mu > 0$, one has the unusual left-handed triad $(\vec{E}, \vec{H}, \vec{\beta})$ shown in Fig. 1.1 (b) . Thus, the frequency being always a positive quantity, the phase velocity

$$\vec{v}_p = \frac{\omega}{\beta}\hat{\beta}, \qquad \left(\hat{\beta} = \frac{\vec{\beta}}{|\beta|}\right) \tag{1.21}$$

in a LHM, Eq. (1.21), points opposite to the phase velocity in a RHM, Eq. (1.19), (1.20). Moreover, whereas the wave number β is known to be positive in a RHM (outward propagation from the source), it is negative in a LHM (inward propagation to the source):

$$\vec{\beta} \times \vec{E} = -\omega|\mu|\vec{H} \tag{1.22}$$
$$\vec{\beta} \times \vec{H} = +\omega|\epsilon|\vec{E} \tag{1.23}$$

$$RHM: \quad \beta > 0 \quad (v_p > 0), \tag{1.24}$$
$$LHM: \quad \beta < 0 \quad (v_p < 0), \tag{1.25}$$

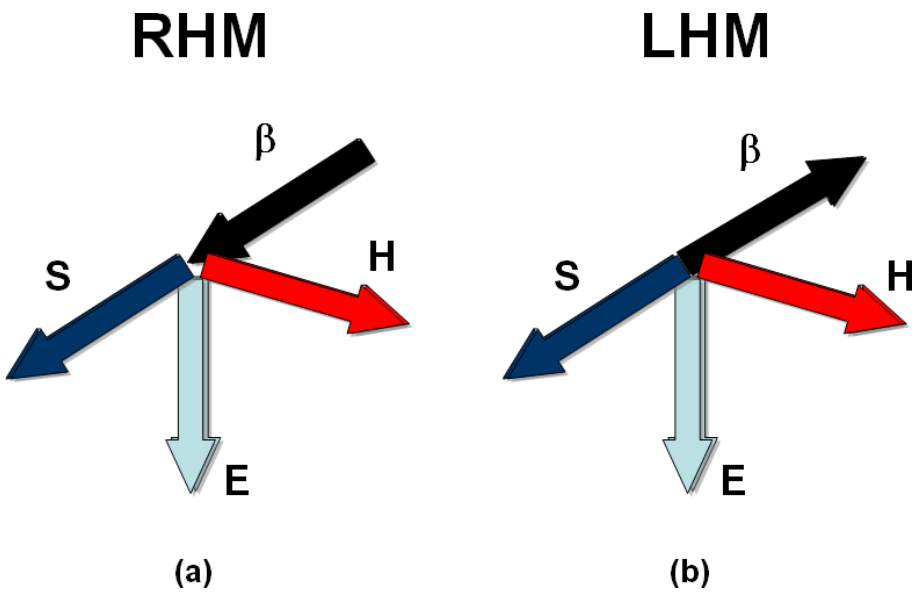

Figure 1.1: Orientation of field quantities $\vec{E}$, $\vec{H}$, Poynting vector $\vec{S}$, and wavevector number $\vec{\beta}$ in right-handed media (RHM) and left-handed media (LHM).

It follows from Eqs. (1.23), (1.25) and Fig. 1.1(b) that, in a LHM the phase, which is related to phase velocity v_p, propagates backward to the source in the opposite direction to that of power, related to the group velocity v_g.

The power flow P_0 is related to the magnitude of the Poynting vector $\vec{S}$, defined as

$$\vec{S} = \vec{E} \times \vec{H} \tag{1.26}$$

$\vec{S}$ is oriented along the direction of propagation of energy over time and is therefore parallel to the group velocity [4]

$$\vec{v}_g = \nabla_{\vec{\beta}}\omega, \tag{1.27}$$

which may be broadly defined as the velocity of a modulated signal in a distortionless medium. Thus, in contrast to the wave vector $\vec{\beta}$, the Poynting vector is not dependent on the constitutive parameters ϵ and μ of the medium, but only on $\vec{E}$ and $\vec{H}$. This conclusion completes the characterization of RHM's and LHM's (Fig. 1.1), which may be summarized as follows, considering positive the direction of the power flow

$$RHM : v_p > 0 \qquad (\beta > 0) \quad and \quad v_g > 0, \tag{1.28}$$

$$LHM : v_p < 0 \qquad (\beta < 0) \quad and \quad v_g > 0. \tag{1.29}$$

The fact that the phase velocity is negative ($v_p < 0$) might seem troubling at first glance. However, this appears more acceptable if one remembers that phase velocity

simply corresponds to the propagation of a perturbation and not of energy [5]. By contrast, a negative group velocity ($v_g < 0$) would violate causality, as it would correspond to transfer of energy toward the source! If often negative-gradient dispersion curves $\omega(k)$ associated with positive values of k (i.e., apparently negative group velocity modes) are observed in standard representations of dispersion diagrams, these curves should be interpreted as the eigen-solutions of the wave equation corresponding to the situation where the source is placed at the end of the medium (the energy transfer thus going from positive to negative values of the space variable).

The work of Veselago and others [2] on negative refraction did not attract much interest until the publication of a theoretical paper by Pendry [6] entitled "Negative Refraction Makes a Perfect Lens", stimulated the first experimental observations of a negative refractive index by Smith et al [1, 7]. General and authoritative reviews of work in this field in the few years following these publications are given by Pendry [8] and Pendry and Smith [9]. Pendry [6] based on the fact that the resolution of a conventional lens is limited by evanescent waves that do not contribute to the image, showed that in planar negative-index slabs (see sections 1.5 an 1.7), these decaying evanescent waves would become growing with distance, so that all spatial frequency components could, in principle, contribute to the image. However, this sparked a controversy about the physical need of losses and the real capability of producing amplification of evanescent waves by such a LHM slab. Through this chapter, we explain these physical problems and characteristics.

1.3 Negative refractive index

At first thought, it would seem that having $\epsilon < 0$ and $\mu < 0$ should not affect the refractive index $n = \sqrt{\epsilon\mu}$. However, ϵ, μ, and n are complex, and we can write

$$\epsilon = r_\epsilon e^{i\theta} \tag{1.30}$$

$$\mu = r_\mu e^{i\phi} \tag{1.31}$$

and

$$n = \sqrt{\epsilon\mu} = \sqrt{r_\epsilon r_\mu} e^{i(\theta+\phi)/2} \tag{1.32}$$

The requirement that the imaginary part of n be positive for a passive (non-absorbing) medium implies that

$$0 \leq \frac{1}{2}(\theta + \phi) < \pi \tag{1.33}$$

if the real parts of ϵ and μ are both negative, i.e. $\cos\theta < 0$ and $\cos\phi < 0$, then

$$\frac{\pi}{2} \leq \frac{1}{2}(\theta + \phi) < \frac{3\pi}{2} \tag{1.34}$$

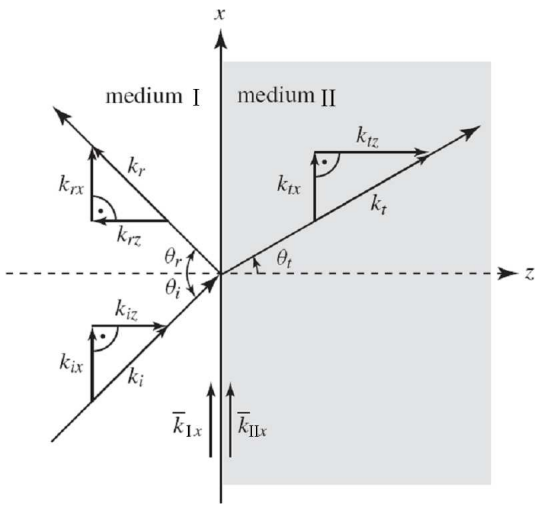

Figure 1.2: Phase-matching at the boundary between two media. The angles θ_i, θ_r, and θ_t are the incident, reflected, and transmitted (or refracted) angles, respectively.

To satisfy both Eq. (1.33) and Eq. (1.34), we must have

$$\frac{\pi}{2} \leq \frac{1}{2}(\theta + \phi) < \pi, \tag{1.35}$$

and, therefore, we obtain a negative real part of the refractive index:

$$n_1 = Re[n] = \sqrt{r_\epsilon r_\mu} \cos\frac{1}{2}(\theta + \phi) < 0. \tag{1.36}$$

Thus, the requirement that n has a positive imaginary part leads to the conclusion that, if ϵ and μ have negative real parts, the real part of n must also be negative.

1.4 Flat lens

In this section, we will show the consequences of negative refractive index when the LHM is interfaced with a RHM. Let us consider a plane wave incident upon the boundary between two homogeneous media, illustrated in Fig. 1.2. In general, from the incident wave, $e^{ik_i \cdot r}$, in medium I, a reflected wave, $e^{ik_r \cdot r}$, in medium I, and a transmitted (or refracted) wave in medium II, $e^{ik_t \cdot r}$, are generated. The boundary condition requires that the tangential components of $\vec{E}$ and $\vec{H}$ be continuous at $z = 0$ for all x and y. Calling the magnitudes of the tangential incident, reflected, and transmitted electric field $E_{i,tan}$, $E_{r,tan}$ and $E_{t,tan}$, respectively, we must have (at $z = 0$) in all possible cases

$$E_{i,tan}e^{-i(k_{ix}x+k_{iy}y)} + E_{r,tan}e^{-i(k_{rx}x+k_{ry}y)} = E_{t,tan}e^{-i(k_{tx}x+k_{ty}y)}, \tag{1.37}$$

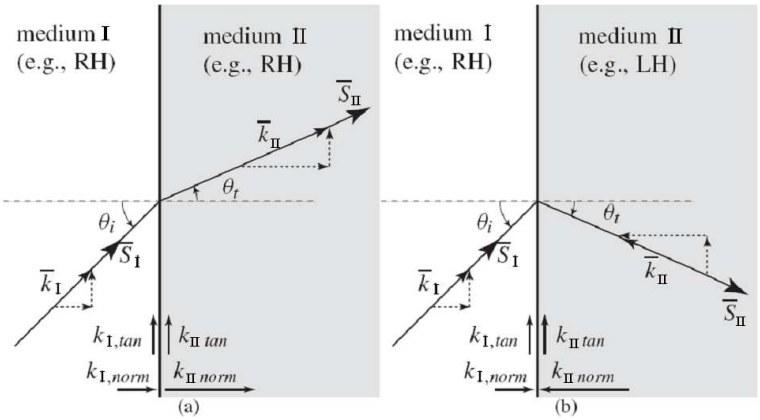

Figure 1.3: Refraction of an electromagnetic wave at the interface between two different media. (a) Case of two media of same handedness (either RHM or LHM): positive refraction. (b) Case of two media of different handedness (one RHM and the other one LHM): negative refraction.

since the total field is the sum of the incident and reflected field in medium I and the transmitted field in medium II. The only way that this equation can be satisfied for all x and y of the interface is that $E_{i,tan} + E_{r,tan} = E_{t,tan}$, and therefore

$$k_{ix} = k_{rx} = k_{tx} = k_x, \tag{1.38}$$

$$k_{iy} = k_{ry} = k_{ty} = k_y, \tag{1.39}$$

which show that the tangential component of the wave number $\vec{k}_{tan} = k_x x + k_y y$ is continuous at the interface between two media

$$\vec{k}_{1,tan} = \vec{k}_{2,tan}. \tag{1.40}$$

This relation is the phase matching-condition, which is a direct consequence of the continuity of the tangential components of E and H and which also holds at the interface between a RHM and a LHM since the continuity of $\vec{E}$ and $\vec{H}$ is conserved in this case. Another consequence from the phase matching condition is that the incident, reflected, and transmitted wave vectors must all lie in the plane of incidence, which is the plane determined by $\vec{k}_i$ and the normal to the interface (z axis). The tangential components of the wave numbers can be expressed as a function of their corresponding angle with the help of Fig. 1.3. For instance, for the x components we have

$$k_{ix} = k_i sin\theta_i, \quad k_{rx} = k_r sin\theta_r, \quad k_{tx} = k_t sin\theta_t, \tag{1.41}$$

where the wave numbers are

$$k_i = \frac{\omega\sqrt{\epsilon_{r1}\mu_{r1}}}{c} = \frac{\omega n_1}{c} = k_r = k_I \quad k_t = \frac{\omega\sqrt{\epsilon_{r2}\mu_{r2}}}{c} = \frac{\omega n_2}{c} = k_{II} \tag{1.42}$$

Eqs. (1.40) and (1.41) applied to the incident and reflected waves lead to the relation $k_i sin\theta_i = k_r sin\theta_r$, which, with Eq. (1.42), yields Snell's law of reflection

$$\theta_r = \theta_i. \tag{1.43}$$

This law is hence unchanged at the interface between a RHM and a LHM. However, Eqs. (1.40) and (1.41) applied to the incident and transmitted waves lead to the relation $k_i sin\theta_i = k_t sin\theta_t$, which, with Eq. (1.42), yields Snell's law of refraction

$$n_I sin\theta_I = n_{II} sin\theta_{II}. \tag{1.44}$$

This law is modified at the interface between a RHM and a LHM, due to the apparition of a negative sign in the refractive index of the LHM (Section 2.1). Snell's law of refraction may be written in the more general form

$$s_I|n_I|sin\theta_I = s_{II}|n_{II}|sin\theta_{II}, \tag{1.45}$$

where s_I and s_{II} represent the sign of n_I and n_{II} respectively. It then appears that if the two media are either RHM or LHM, Snell's law is unchanged due to mutual cancelation of the two signs of teach side of the equation. But from (1.45), the reversal of Snell's law at the interface between a RHM and a LHM, illustrated in Fig. 1.3, manifests. A wave incident upon the interface between two media of different handednesses (RHM and LHM) undergoes negative refraction [Fig. 1.3(b)].As a consequence of phase matching [Eq. (1.37)] and of the sign of the refractive index in each of the two media, it is immediately apparent in Fig. 1.3, that although the normal components of the wave vector $\vec{k}_{norm}$ are parallel at a RHM/RHM or LHM/LHM interface they are antiparallel at a RHM/LHM interface. The relation between the normal components of the wave vectors at the interface may be written in the general form

$$s_I|n_I||k_{II,norm}| = s_{II}|n_{II}||k_{I,norm}|. \tag{1.46}$$

Fig. 1.2 also shows the Poynting vectors S_i which, according to Section 1.2, are parallel and antiparallel to the wave vector in RHM and LHM, respectively. Various negative refractive index effects will be illustrated in the following sections.

By applying Snell's law [Eq. (1.45)] to both surfaces of a LHM slab sandwiched between two RHM, also called a LHM "lens", we obtain the double focusing effect depicted in Fig. 1.4 [2]: two radiated rays with equal symmetric angles from a source at distance z_0 from the first interface, are negatively refracted under an angle of the same magnitude to meet at a distance z_1 in the slab; then they focus again after a

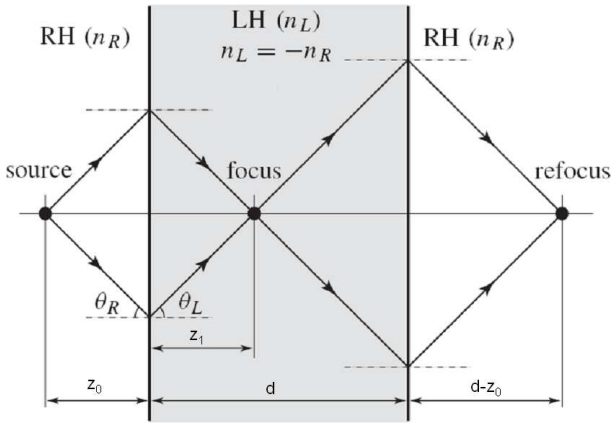

Figure 1.4: Double focusing effect in a "flat lens", which is a LHM slab of thickness d and refractive index n_L sandwiched between two RH media of refractive index n_R with $n_L = -n_R$.

second negative refraction in the second RHM at the distance $d - z_0$ from the second interface, where z_1 is obtained by simple trigonometric considerations as

$$z_1 = z_0 \frac{tan\theta_R}{tan|\theta_L|} \tag{1.47}$$

where θ_R is the incidence angle and θ_L is obtained by Snell's law [Eq. (1.45)], $\theta_L = -sin^{-1}[(n_R/n_L)sin\theta_R]$. Eq. (1.47) shows that if the two media have the same electromagnetic density, that is, refractive indexes of the same magnitude ($n_L = -n_R$), a focus is obtained for all rays at the mirror image of the source, $z_1 = z_0$, since $|\theta_L| = \theta_R$ from Snell's law. Instead of two isolated symmetric plane waves (Fig. 1.4), we now consider a collection of plane waves (or rays), or more generally a cylindrical (2D space) or spherical (3D space) electromagnetic wave, as typically radiated by a point source. It is then necessary to have the two media with the same electromagnetic density to achieve good focusing. In this case, each pair z_0 of symmetric rays with incidence angle θ_R focuses at the same point, because $\theta_L = \theta_R$ so that the focal distances are the same for all pairs of rays, $z_1 = z_0$. If the electromagnetic densities of the two media are different ($|n_L| = n_R$), then rays with different incidence angles refract into different focal points because the ratios $tan\theta_R/tan|\theta_L|$ of the different pairs of rays are all different, leading to different focal distances z_1 . In that case, spherical aberration [10], occurs, and the focal point degenerates into a diffuse focal spot whose area increases with the contrast of refractive indexes, $|n_L|/n_R$

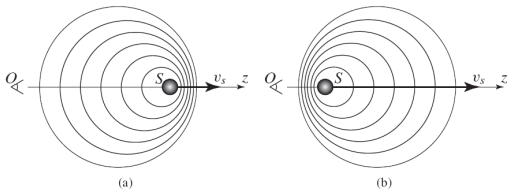

Figure 1.5: Doppler effect. (a) Conventional, in a RHM ($\Delta\omega > 0$). (b) Reversed, in a LHM ($\Delta\omega < 0$). After Ref. [3].

1.5 Reversal of Doppler effect

We consider a source S in motion along a direction z and radiating omnidirectionality an electromagnetic wave with angular frequency ω, as illustrated in Fig. 1.5. In the far-field of the source, the radiated fields have the form [11]

$$\vec{E}(z,t), \vec{H}(z,t) \propto \frac{e^{-i\varphi}}{r} \qquad with \quad \varphi = \omega t - \beta r \tag{1.48}$$

where β represents the wave number in the medium in which S moves and radiates and r the standard radial variable of the spherical coordinates system.

Let us consider what happens to the radiated wave along the direction of the motion of the source, i.e., for $r = z$ (in $\theta = 0$). If the sources moves toward positive values of z with a velocity $v_s = z/t$, its position as a function of time is $z = v_s t$. Consequently, the phase seen by an observer $\mathcal{O}$ located at the left-hand side of S (i.e., looking at S toward positive values of z) may be developed as follows along the z axis:

$$\varphi = \omega t - \beta v_s t = \omega \left(1 - \frac{\beta}{\omega} v_s\right) t = \omega \left(1 - \frac{v_s}{v_p}\right) t = \omega \left(1 - s\frac{v_s}{|v_p|}\right) t \tag{1.49}$$

where s is the handedness sign function. Since $\omega/\beta = v_p$ according to Eq. (2.10). The coefficient of t is the Doppler frequency $\omega_{Doppler}$, which is the difference of the frequency ω of the motionless ($v_s = 0$) source and the Doppler frequency shift, $\Delta\omega$

$$\omega_{Doppler} = \omega - \Delta\omega, \qquad with \quad \Delta\omega = s\frac{v_s}{|v_p|}. \tag{1.50}$$

In a RHM, $\Delta\omega > 0$ since $s = +1$, and therefore the frequency measured by the observer looking at the receding source is shifted downward or "red-shifted", as illustrated in Fig. 1.5(a); on the other hand, an observer located on the right-hand side of the source, i.e., seeing a proceeding source, would measure a frequency shifted upward or "blue-shifted", because the sign of v_s would be changed for that observer. In a LHM, because $s = -1$, the whole phenomenon is reversed, as shown in Fig.

1.5(b): The Doppler frequency of a receding source is blue-shifted, whereas that of a proceeding source is red-shifted. This phenomenon of reversal of Doppler effect in a LHM was pointed out by Veselago back in 1967 as an immediate consequence of left-handedness [2].

1.6 Dispersion

Veselago [2] noted that when there is no frequency dispersion nor absorption $\epsilon < 0$ and $\mu < 0$ are unphysical, since in this case the total energy u would be negative,

$$u = \frac{1}{4}\left[\epsilon|\vec{E}|^2 + \mu|\vec{H}|^2\right] < 0 \tag{1.51}$$

i.e. the permittivity $\epsilon(\omega)$ and permeability $\mu(\omega)$ must depend on the frequency ω, so that for a medium with losses, the term that appears in the conservation of the Poynting vector is the variation of energy u with time

$$\frac{du}{dt} = \omega Im\{\epsilon\}|E|^2 + Re\{\frac{d}{d\omega}(\epsilon\omega)|\vec{E}^*\frac{dE}{dt}\} + \omega Im\{\mu\}|H|^2 + Re\{\frac{d}{d\omega}(\mu\omega)|\vec{H}^*\frac{dH}{dt}\} \tag{1.52}$$

and the field energy density in an ideally lossless dispersive medium becomes [4]

$$u_\omega = \frac{1}{4}\left[\frac{d}{d\omega}(\epsilon\omega)|\vec{E}_\omega|^2 + \frac{d}{d\omega}(\mu\omega)|\vec{H}_\omega|^2\right] \tag{1.53}$$

away from any absorption resonances. The quantity given by Eq. (1.53) is positive because

$$\frac{\partial(\epsilon\omega)}{\partial\omega} > 0 \tag{1.54}$$

$$\frac{\partial(\mu\omega)}{\partial\omega} > 0 \tag{1.55}$$

Hence the consequence is that the LHM must be a dispersive medium in order that the total energy be positive. On the other hand, it is important to understand the limits imposed to negative refraction by losses, always present as required by causality (see section 1.8).

Kramers-Kronig relations connect the real and imaginary parts of the constitutive parameters [12]. Being $\epsilon = \epsilon_1 + i\epsilon_2$ we obtain:

$$\epsilon_1(\omega) - 1 = \frac{2}{\pi}P\int_0^\infty \frac{\omega'\epsilon_2(\omega')}{\omega'^2 - \omega^2}d\omega' \tag{1.56}$$

it follows that

$$2\omega[\epsilon_1(\omega) - 1] + \omega^2\frac{d\epsilon_1}{d\omega} = \frac{4\omega}{\pi}P\int_0^\infty \frac{\omega'^3\epsilon_2(\omega')^2}{\omega'^2 - \omega^2} \tag{1.57}$$

For a passive medium $\epsilon_2 \geq 0$ at all frequencies and the integral is positive. Then [4]

$$\omega \frac{d\epsilon_1}{d\omega} > 2(1 - \epsilon_1) \tag{1.58}$$

and, therefore,

$$\frac{d}{d\omega}(\epsilon_1 \omega) > 2 - \epsilon_1 \tag{1.59}$$

and $d(\epsilon_1\omega)/d\omega > 0$ for $\epsilon_1 < 0$. The corresponding inequality of the permeability μ is derived in the same way. It can also be shown that, away from any absorption resonances, the group index $n_g = n + \omega dn/d\omega$ is positive in a LHM. To see this, write $n = -\sqrt{|\epsilon||\mu|}$, where $\epsilon = \epsilon_1$ and $\mu = \mu_1$, so that together Eqs.(1.54) and (1.55)

$$n_g = -\sqrt{|\epsilon||\mu|} - \frac{\omega}{2}\sqrt{\frac{|\epsilon|}{|\mu|}}\frac{d|\mu|}{d\omega} - \frac{\omega}{2}\sqrt{\frac{|\mu|}{\epsilon|}}\frac{d\epsilon|}{d\omega} = \tag{1.60}$$

$$= -\frac{1}{2}\sqrt{\frac{|\epsilon|}{|\mu|}}\left(|\mu| + \omega\frac{d|\mu|}{d\omega}\right) - \frac{1}{2}\sqrt{\frac{|\mu|}{\epsilon|}}\left(|\epsilon| + \omega\frac{d|\epsilon|}{d\omega}\right) =$$

$$= \frac{1}{2}\sqrt{\frac{|\epsilon|}{|\mu|}}\frac{d}{d\omega}(\mu\omega) + \frac{1}{2}\sqrt{\frac{|\mu|}{\epsilon|}}\frac{d}{d\omega}(\epsilon\omega) > 0 \tag{1.61}$$

Hence, we see that this result is no more that a consequence of causality, in other words the energy of the wave goes in the same direction as the impinging wave, i.e. do not come from the not-source space. On the other hand, one more important consequence of this calculation is that the medium is necessarily dispersive for getting a negative refraction regime.

1.7 Amplification of evanescent waves

It turns out that something more subtle than "light bending the wrong way" happens in a LHM slab: the behavior of evanescent waves is very different than usual. This leads to one of the most intriguing prospects for LHMs, namely the possibility of constructing lenses with subwavelength resolution. In this section, we will briefly review some aspects and consequences for evanescent waves.

Suppose we expand the electric field in the half-space $z > 0$ in terms of spatial and temporal frequency components by means of its angular spectrum of plane waves

$$\vec{E}(x, y, z, t) = \int_0^\infty d\omega \int_\infty^\infty dk_x \int_\infty^\infty dk_y \vec{A}(k_x, k_y, \omega, z) e^{-i(\omega t - k_x x - k_y y)} \tag{1.62}$$

If any sources of radiation are present only in the half-space $z < 0$, we have

$$\nabla^2 \vec{E} - \frac{1}{c^2}\frac{\partial^2 \vec{E}}{\partial t^2} = 0 \tag{1.63}$$

for $z > 0$ and, therefore, the angular spectrum satisfies:

$$\frac{\partial^2 \vec{A}}{\partial z^2} + \left(\frac{\omega^2}{c} - k_x^2 \right) \vec{A}(k_x, k_y, \omega, z) \tag{1.64}$$

which has solutions of the form

$$A(k_x, k_y, \omega, z) \propto e^{\pm i k_z z} \tag{1.65}$$

where

$$k_z = \sqrt{\frac{\omega^2}{c^2} - k_x^2 - k_y^2}. \tag{1.66}$$

k_z can be real or imaginary, depending on whether $k_x^2 + k_y^2 < \omega^2/c^2$ or $k_x^2 + k_y^2 > \omega^2/c^2$. In the latter case, for waves propagating into $z > 0$ we have

$$k_z = i|k_z| \tag{1.67}$$

Then for a field that propagates towards increasing z one has:

$$\vec{E}(x, y, z, t) = \int_0^\infty d\omega \int \int_{k_x^2 + k_y^2 > \omega^2/c^2} dk_x dk_y A_{ord}\left(k_x, k_y, \omega\right) \times e^{i k_x x + k_y y + k_z z - \omega t} \tag{1.68}$$

$$+ \int_0^\infty d\omega \int \int_{k_x^2 + k_y^2 < \omega^2/c^2} dk_x dk_y A_{ev}\left(k_x, k_y, \omega\right) \times e^{i k_x x + k_y y - \omega t} e^{-|k_z| z}$$

The first term on the right-hand side is a superposition of ordinary plane waves propagating in the positive z direction. The second term defines a superposition of evanescent wave components that decay exponentially with z. Evanescent waves have not received much attention in the standard texts on optics or electromagnetism but it is clear from the derivation of (1.68) that they are required for completeness. They are present whenever the field in some plane ($z = 0$) has spatial frequency components k_x, k_y such that $k_x^2 + k_y^2 > \omega^2/c^2$ i.e. whenever the field in this plane varies on a scale smaller than the wavelength. And ultimately, this is always the case when the object is finite. The best known example where evanescent waves occur is total internal reflection when a beam of light is incident from glass, for example, onto a glass/air interface at an angle greater than the critical angle. On the glass side $k_x^2 + k_y^2 < n^2\omega^2/c^2$, corresponding to ordinary propagation, and the variations in the field occur on a scale larger than a wavelength. On the air side, however, $k_x^2 + k_y^2 > \omega^2/c^2$ and the spatial variations of the field are on a scale smaller than a wavelength. An evanescent field, therefore, appears in the air side and its intensity decays with distance z away from the interface as $exp(-az)$, where

$$a = \frac{4\pi n_a}{\lambda} \sqrt{\frac{n_g^2}{n_a^2} sin^2\theta_i - 1} \tag{1.69}$$

n_a and n_g being the refractive indices of air and glass, respectively, θ_i denoting the angle of incidence, and λ is the vacuum wavelength. If a second piece of glass is brought near the first piece, leaving an air gap between them, the internal reflection is "frustrated" and light can propagate into the second glass with a transmission coefficient $t \approx 1$ if the width of the air gap is small compared with the wavelength. A nice demonstration of frustrated total internal reflection is described by Zhu et al [13], who also discuss some of the long history of the subject. The expansion 1.68 shows that the evanescent waves do not undergo any variation of phase in the z direction. This is related to the fact that evanescent waves and their quantum−mechanical analog of tunnelling into a classically forbidden region [13] can exhibit "superluminal" behavior. The only phase variation of the evanescent waves is along their propagation direction, parallel to the interface. An important characteristic of evanescent waves is that they do not transport energy in the direction in which they decay. Consider, for example, the monochromatic evanescent wave with electric field

$$\vec{E} = \vec{x}E_0 cos(ky - \omega t)e^{-Kz}. \tag{1.70}$$

The Poynting vector $\vec{S} = \vec{E} \times \vec{H}$ is

$$\vec{S} = \frac{E_0^2}{\omega\mu}\left[k\vec{y}cos^2(ky - \omega t) - Kzcos(ky - \omega t)sin(ky - \omega t)\right]e^{2Kz} \tag{1.71}$$

and the component of $\vec{S}$ in the z direction has a cycle average of zero. Because of their exponential decay with distance, evanescent waves are said to belong to the near field of the object, as opposed to the "far field" associated with the homogeneous plane-wave components. Near field optics (e.g. a photonic scanning tunneling microscope) involves distances close enough to an object that evanescent waves are captured, giving information about the object that is not available in the far field. Quantization of evanescent waves has been carried out by Carniglia and Mandel [14]. In their approach, each triplet of incident, reflected, and transmitted waves is regarded as a single mode for the purpose of quantization. Experiments have demonstrated that evanescent photons are emitted and absorbed as expected from this theory, so that a single photon can be associated with a homogeneous wave on one side of the interface and an evanescent wave on the other. Expansions in evanescent waves of the field from a uniformly moving charge have been usefully employed to describe Cerenkov, SmithPurcell and related effects. In a LHM the exponent of the evanescent part of the field is increasing, and this increasing involves the restoration in the evanescent Fourier harmonics at the image plane. Fig. 1.6 shows the amplitude pattern for one of these evanescent Fourier harmonics. This restoration is due to the excitation of a physical surface wave at the right interface of the slab [15]. This physical surface wave couples with the evanescent fields generated at the source through the excitation of a nonphysical surface wave (do not satisfy physical boundary conditions at infinity when they are considered in an unbounded system) at the left interface of the slab.

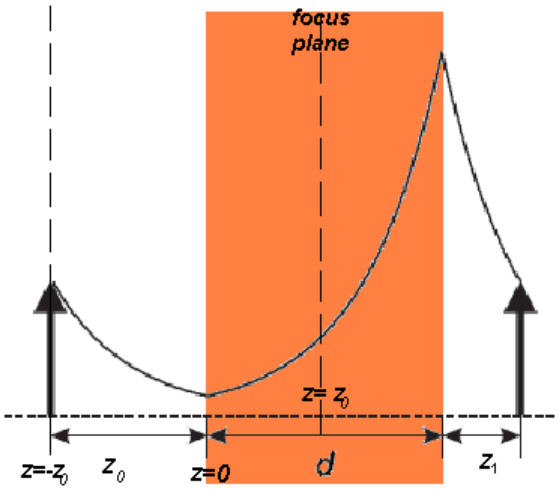

Figure 1.6: Amplitude pattern for an evanescent Fourier harmonic of the perfect lens.

Some considerations should be made at this point. As we approach the back interface of the slab, the density of energy stored by these evanescent waves grows by the exponential factor $exp[2k_z(d-\delta)]$, where δ is the distance to this interface. In the limit $|k_x|, |k_y| \to \infty$ we have that the previous exponent goes to infinity, and, therefore, the density of energy grows to infinity at the slab interface. Therefore, the perfect lens implies a nonphysical divergence of energy [16]; we will return to this point later (see Section 1.8), it should be mentioned here that this apparent difficulty disappears if lossy slabs are considered, however these losses limit and change the imaging process [17](see chapter 2).

1.7.1 The silver slab

When the scale of distances under consideration is deeply subwavelength, the electrostatic limit can be applied. In this case, the electric and magnetic responses of a material decouple, and only one material property (either ϵ or μ) needs to be negative to support resonant surface waves for one specific polarization (transverse magnetic, TM, or transverse electric, TE mode) [6].

This makes noble metals such as silver natural candidates for optical superlensing, because a negative permittivity is easily attainable in them as a consequence of the collective excitation of conduction electrons. Let us consider a superlens consisting of a silver slab separated from an object by a spacer layer, and coated on the opposite side with an imaging material [18], (Fig. 1.7).

For enhanced transmission of evanescent waves, it is found that an asymptotic impedance match ($k_{zi}/\epsilon_i + k_{zj}/\epsilon_j = 0$) has to be met at the surface of silver, known

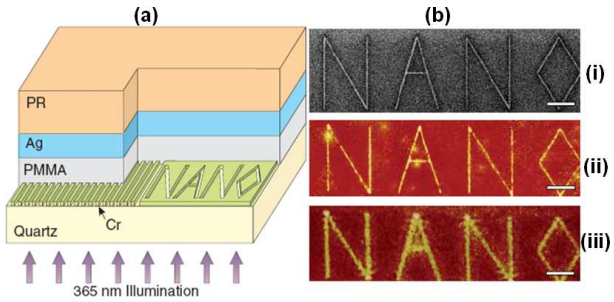

Figure 1.7: An arbitrary object "NANO" was imaged by silver superlens. (i) FIB image of the object. The linewidth of the "NANO" object was 40 nm. Scale bar in (i) to (iii), 2 mm. (ii) AFM of the developed image on photoresist with a silver superlens. (iii) AFM of the developed image on photoresist when the 35-nm-thick layer of silver was replaced by PMMA spacer as a control experiment. After Ref. [18].

as the surface plasmon excitation condition (k_{zi}, cross-plane wave vector in silver; ϵ_i, permittivity of silver; k_{zj}, cross-plane wave vector in dielectric; and ϵ_j, permittivity of dielectric). It is widely known in metal optics that when the two media take the opposite sign in permittivity and $|\epsilon_i| \gg \epsilon_j$, only surface plasmons at the narrow range of in-plane wave vector (k_x) that are close to k_0 can be resonantly coupled. However, less well known is that when $|\epsilon_i| \sim \epsilon_j$ and they are of opposite sign, the excitable surface plasmon band of k_x is significantly broadened, resulting in the superlensing effect.

Hence, for polarization parallel to the plane of incidence, we obtain for the transmission coefficient in the limit $\omega \to 0$

$$t = \frac{4\epsilon exp(ik_z d)}{(\epsilon+1)^2 - (\epsilon-1)^2 exp(2ik_z d} \tag{1.72}$$

with $k_z = i\sqrt{k_x^2 + k_y^2}$. For $\epsilon \to -1$, this becomes

$$t = exp(-ik_z d) = exp(\sqrt{k_x^2 + k_y^2} d) \tag{1.73}$$

Thus, it should be possible, in the limit of large wavelength compared with size scales of interest,

Using a similar scheme the group of Richard J. Blaikie confirmed the superlensing effect in silver films [19, 20] and realized a study about its properties in lithography [21, 22] showing that the superresolution achieved due to these silver slabs is similar or less than that of operation ranges in near field optics or microlens systems. However, this is inherently associated with substantial energy dissipation or loss (that is, the imaginary part of ϵ) and imperfections or roughness in the silver surface, which hinders the resolution of the "perfect image". The term "superlens", by contrast to the initial

"perfect lens" coining [6], is used for lenses that take this practical limit into account. Unlike conventional lenses, the resolution of the superlens is not limited by diffraction, but rather determined by absorption and dispersion which rate how many evanescent modes can be restored. Another consequence of the material loss and imperfections is that the distance between the slab and both the object and its image, as well as the slab's thickness, must all be small compared with the wavelength if we are to obtain meaningful resonant enhancement of the evanescent waves [17], (this superlensing effect will be developed with more details in section 3.5), and hence is limited to the near field.

The superlens experiments discussed so far are only capable of projecting a sub−diffraction−limited image in the near field, as the evanescent waves will continue to decay away from such lenses. A simple slab superlens is "near sighted". Recent studies propose to make the image in the far field by superposing a subwavelength grating onto the silver slab interface. This grating selectively enhances the evanescent waves from the object and also converts them into propagating waves [23]. An alternative approach is the so−called hyperlens [24], it uses an anisotropic medium in curved multilayer stacks. Evanescent waves can tunnel through flat films to produce a high resolution image. The hyperlens essentially works as an optical compressor, or turbine, that continuously compresses or transforms the large wavevectors of the original evanescent waves into smaller ones that propagate to the far field.

1.8 The problem of the amplification: Physics involves losses

Let us consider now the case where an evanescent wave from a source at $z = -z_0 < 0$ is incident from vacuum onto an LHM (Fig. 1.6). For polarization perpendicular to the plane of incidence (yz), we write the incident field as

$$E = E_0 \vec{x} e^{i(k_y y + k_z z)} e^{-i\omega t} \tag{1.74}$$

for $z > -z_0$, where

$$k_z = i\sqrt{k_y^2 - \omega^2/c^2} \qquad (k_y^2 > \omega^2/c^2). \tag{1.75}$$

Similarly, the transmitted field is written as

$$\vec{E'} = E_0' \vec{x} e^{i(k_y' y + k_z' z)} e^{-i\omega t} \tag{1.76}$$

$$k_z' = i\sqrt{k_y^2 - \epsilon\mu\omega^2} \qquad (k_y^2 > \epsilon\mu\omega^2) \tag{1.77}$$

The corresponding expression for the reflected field is written using double primes, as in Ref. [25]. It has been demonstrated [26] that the homogenous part of the divergent

wavefield, propagated from the inner focusing plane to a plane beyond the inner focus in the LHM with $n = -1$ is equal to the homogenous part of the converging field propagated from the plane beyond the inner focus to the plane of the inner focus in a medium with $n = 1$, both fields having the same value $f(x, y)$ in the inner focus $z = z_0$. That is, the exponential factor in the transmitted field increases without limit for $z > z_0$(inner focus position) as $k_x \to \infty$ and $k_y \to \infty$.

Another point of view is observing the transmission coefficients, so, using the expressions for $\vec{D}$ that follow from Maxwell's equations, and enforcing the boundary conditions at $z = 0$, we obtain straightforwardly the amplitude transmission and reflection coefficients t and r, respectively, at the interface ($z = 0$) between vacuum and the LHM:

$$t = \frac{2\mu k_z}{\mu k_z + \mu_0 k'_z} \tag{1.78}$$

$$r = \frac{\mu k_z - \mu_0 k'_z}{\mu k_z + \mu_0 k'_z} \tag{1.79}$$

It appears from the previous equations that t and r diverge as $\epsilon \to -\epsilon_0$ and $\mu \to -\mu_0$, i.e. when the half-space in figure 7.4 has refractive index $n' = -1$. However, as in many situations in physics, a divergence is avoided when dissipation is taken into account. Let us account for absorption in the LHM by writing

$$\epsilon = \epsilon_0(1 - i\delta) \tag{1.80}$$

$$\mu = \mu_0(1 - i\delta) \tag{1.81}$$

with $\delta > 0$. Then the denominator in t and r does not go to zero. Therefore, the losses are an element necessary in a LHM system.

Another interesting criterion which imposes lower limits on the electric and magnetic losses in the region of negative refraction have been developed by Stockman [27] from the fundamental requirement of causality. He considers a material to be an effective medium characterized by macroscopic permittivity $\epsilon(\omega)$ and permeability $\mu(\omega)$. The squared complex refraction index $n^2(\omega) = \epsilon(\omega)\mu(\omega)$ has exactly the same analytical properties as $\epsilon(\omega)$ and $\mu(\omega)$ separately: $n^2(\omega)$ does not have singularities in the upper half-plane of complex ω and $n^2 \to 1$ for $\omega \to \infty$. Therefore, absolutely similar to the derivation of the Kramers−Kronig relations for the permittivity or permeability discussed before, we obtain a dispersion relation for $n^2(\omega)$,

$$Ren^2(\omega) = 1 + \frac{2}{\pi}\mathcal{P}\int_0^\infty \frac{Imn^2(\omega_1)}{\omega_1^2 - \omega^2}\omega_1 d\omega_1 \tag{1.82}$$

where $\mathcal{P}$ denotes the principal value of the integral.

The refractive index n itself does not enter in the Maxwell equations; it is not a susceptibility, and it does not have to obey the causality, while n^2 does. This

theory is based on n^2, not on n; the noncausality of n is irrelevant for these purposes. Now we assume that both at and near the observation frequency ω the material is transparent (e.g., the losses are compensated by gain), which mathematically implies that $Imn^2(\omega) = 0$ and $\partial[Imn^2(\omega)]/\partial\omega = 0$ (this vanishing is required only at the observation frequency). Then the principal value in the right-hand side of Eq. (1.82) can be omitted. Multiplying both sides of this equation by ω^2 and differentiating over ω (one can differentiate under the integral over ω as a parameter, because the point $\omega_1 = \omega$ is not singular anymore), we obtain

$$\frac{\partial\omega^2[Ren^2(\omega) - 1]}{\partial\omega} = \frac{4\omega}{\pi}\int_0^\infty \frac{Imn^2(\omega_1)}{\omega_1^2 - \omega^2}^2 \omega_1^3 d\omega_1 \tag{1.83}$$

The left-hand side of this equation can be expressed in terms of the phase velocity $\vec{v}_p = (\vec{k}/k)\omega/k$, where real wave vector is $k = \sqrt{Ren(\omega)^2}\omega/c$, and c is speed of light, and group velocity $\vec{v}_g = (\vec{k}/k)\omega/k$. In this way, we obtain

$$\frac{1}{\vec{v}_p\vec{v}_g} - \frac{1}{c^2} = \frac{2}{\pi c^2}\int_0^\infty \frac{\epsilon_2(\omega_1)\mu_1 + \mu_2(\omega_1)\epsilon_1(\omega_1)}{(\omega_1^2 - \omega^2)^2}\omega_1^3 d\omega_1 \tag{1.84}$$

where $Imn^2(\omega) = \epsilon_2(\omega)\mu_1(\omega) + \mu_2(\omega)$. In the case of the negative refraction, the directions of the phase and energy propagation are opposite, therefore $\vec{v}_p\vec{v}_g < 0$. Consequently, we obtain from Eq. (1.84) a rigorous criterion of the negative refraction with no (or low) loss at the observation frequency ω as

$$\frac{2}{\pi}\int_0^\infty \frac{\epsilon_2(\omega_1)\mu_1 + \mu_2(\omega_1)\epsilon_1(\omega_1)}{(\omega_1^2 - \omega^2)^2}\omega_1^3 d\omega_1 \leq -1 \tag{1.85}$$

This criterion directly imposes the lower bounds on the dielectric losses $[\epsilon_2(\omega_1) > 0]$, overlapping with the magnetic plasmonic behavior $[\mu_1 < 0]$ and the magnetic losses $[\mu_2 > 0]$ overlapping with the electric plasmonic behavior $[\epsilon_2 < 0]$. The denominator $(\omega_1^2 - \omega^2)^2$ makes the integral to converge for $|\omega_1 - \omega|$ large; it would have diverged at $|\omega_1 - \omega| \to 0$ if the integrand did not vanish at that point. Thus, the major contribution to Eq. (1.85) comes from the lossy, overlapping electric and magnetic resonances close to observation frequency ω.

And, the stability of the system requires that no net gains are present at any frequency, i.e., $\epsilon_2(\omega) \geq 0$ and $\mu_2 \geq 0$ everywhere.

1.9 Fabrication of LHM

The difficulty in realizing simultaneously negative values of ϵ and μ lies in the fact that the resonance frequencies for which $\epsilon < 0$ tend to be much larger than the resonance frequencies for which $\mu < 0$, high frequencies (typically optical or infrared)

in the former case and much lower frequencies in the latter. Moreover, the resonance regions tend to be very narrow in either case.

In this section, we take for granted that ϵ and μ can be simultaneously negative, and we explain the way to achieve this realization.

1.9.1 Negative permittivity

It is well known that plasmas are described by a permittivity function that becomes negative below a plasma frequency ω_p, causing the propagation constant in the plasma to become imaginary. In this frequency region, electromagnetic waves incident on the plasma suffer reactive attenuation and are reflected. Thus, the plasma frequency bears a resemblance to the modal cutoff frequencies of particular electromagnetic waveguides. It is evident that in the construction of electromagnetic structures of any sort in the microwave range, we rely on the properties of metals. Essentially, metals are plasmas, since they consist of an ionized "gas" of free electrons. Below their plasma frequency, the real component of the permittivity of bulk metals can be said to be negative. However, the natural plasma frequencies of metals normally occur in the ultraviolet region of the electromagnetic spectrum, in which wavelengths are extremely short. This condition certainly precludes the use of realizable artificial dielectrics in the microwave range, which, moreover, must operate in the longwavelength regime. Although the permittivity is negative at frequencies below the plasma frequency, the approach toward absorptive resonances at lower frequencies increases the dissipation, hence the complex nature of ϵ. Thus, to observe a negative permittivity with low absorption at microwave frequencies, it would be necessary to somehow depress the plasma frequency of the metal. This problem was addressed by Pendry et al. [28] (and simultaneously by Sievenpiper et al. [29]), who proposed the familiar structure of Rotman consisting of a mesh of very thin conducting wires arranged in a periodic lattice, but approached the problem from a novel standpoint. Due to the spatial confinement of the electrons to thin wires, the effective electron concentration in the volume of the structure is decreased, which also decreases the plasma frequency. More significant, however, is that the self-inductance of the wire array manifests itself as a greatly enhanced effective mass of the electrons confined to the wires. This enhancement reduces the effective plasma frequency of the structure by many orders of magnitude, placing it well into the gigahertz range. Thus, an array of thin metallic wires, by virtue of its macroscopic plasma-like behavior, produces an effectively negative permittivity at microwave frequencies.

1.9.2 Negative permeability

In magnetostatics it is well-known, that a magnetic dipole moment is generated by a circulating current in a coil with an inductance L. The magnetic dipole moment is given by the product of the area of the coil and the current and is orientated perpen-

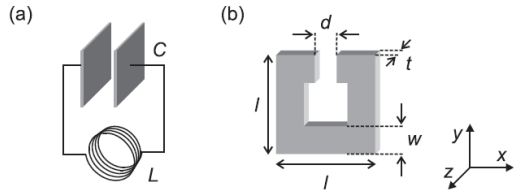

Figure 1.8: (a)Illustration of the analogy between a usual LC circuit, consisting of a capacitance C and a inductance L, and (b) a split-ring resonator (SRR).

dicular to the plane of the coil. Adding a capacitance C to the coil, a LC oscillatory circuit [a schematic illustration is given in Fig. 1.8(a)] with resonance frequency ω_{LC} is obtained. At ω_{LC} one expects a resonantly enhanced current flow and hence a resonantly enhanced magnetic dipole moment. Fig. 1.8(b) exemplarily depicts a LC oscillatory circuit which has been reduced to the limit: It consists of a wire which has been bent to form a coil with only one winding. The ends of the wire form the capacitor. This structure is called split-ring resonator (SRR). The resonance frequency ω_{LC} of such an oscillatory circuit can be roughly estimated making several approximations: We assume that the capacitance can be characterized by the standard formula of a plate capacitor with closely arranged plates ($C/area/distance$) and the inductance by the formula of a "very long" coil with only one winding ($L/area/length$) Thus, taking the nomenclature of Fig. 1.8(b), the capacitance is given by:

$$C = \epsilon_0 \epsilon_C \frac{wt}{d} \tag{1.86}$$

with the permeability of the material between the capacitor plates ϵ_C, and the inductance of a "long" coil with only one winding by

$$L = \mu_0 \frac{l^2}{t} \tag{1.87}$$

Using these values in the equation for the resonance of an LC circuit leads to the eigenfrequency of the SRR

$$\omega_{LC} = \frac{1}{\sqrt{LC}} = \frac{1}{l} \frac{c_0}{\sqrt{\epsilon_r}} \sqrt{\frac{d}{w}} \tag{1.88}$$

or to the LC-resonance wavelength

$$\lambda_{LC} = \frac{2\pi c_0}{\omega_{LC}} = l 2\pi \sqrt{\epsilon_r} \sqrt{\frac{w}{d}} \tag{1.89}$$

Even though this equation is derived with many simplifications, it allows to deduce the basic behavior of SRRs, which will be confirmed by numerical simulations later

in this chapter. Eq. (1.88) indicates that the resonance frequency $\omega_L C$ is inversely proportional to the size of the SRR if all parameters are scaled down simultaneously. For a fixed ratio w/d this translates into a resonance wavelength proportional to the side length l. Next we want to compare the resonance wavelength with the side length l. For typical parameters ($\epsilon_C \geq 1$ and $w \approx d$), the resonance wavelength is about 10 times larger than the side length:

$$\lambda_{LC} \approx 10 \times l \tag{1.90}$$

This allows us to design periodic metamaterials consisting of such SRRs, where the lattice constant a is much smaller than the LC-resonance wavelength. For the SRR samples fabricated by us, they are arranged in a planar square lattice, with nominally identical lattice constants $a_x = a_y$. It is also possible to incorporate more than one capacitance into the circuit, or in other words, more slits into the ring. This obviously reduces the total capacitance $C_{total} = (1/C1 + 1/C2)^{-1}$, which also decreases the resonance wavelength. Thus, the single−slit SRR exhibits the largest ratio of resonance wavelength to SRR size, which means they are best suited for constructing effective metamaterials. This simple model can also be used to obtain an expression for the magnetic permeability $\mu(\omega)$ [30]. We restrict the discussion to the case where the magnetic field is perpendicular to the SRR plane and a coupling via the electric field is not possible. According to Kirchhoff's rule, the sum over all voltage drops in a closed loop is zero. For the case of the LC resonator, the self-induction voltage of the inductance U_L plus the voltage drop over the capacitance U_C and due to the resistance U_R equals the voltage induced by the external magnetic field U_{ind}

$$L\dot{I} + RI + \frac{1}{C}\int I dt = U_{ind} = -\dot{\phi}. \tag{1.91}$$

If we assume a homogeneous magnetic field in the coil, the external magnetic flux is given by $\phi = l^2 \mu_0 H$, with the external magnetic field $H = H_0 e^{-i\omega t} + c.c.$ Taking the time derivative of Eq. (1.91) and dividing by L yields

$$\ddot{I} + \frac{R}{L}\dot{I} + \frac{1}{LC}I = \frac{1}{L}\dot{U}_{ind} = +\omega^2 \frac{\mu_0 l^2}{L} H_0 e^{-i\omega t} + c.c. \tag{1.92}$$

With the ansatz $I = I_0 e^{-i\omega t} + c.c.$ we get the solution for the current. Next, we can calculate the individual magnetic dipole moment $l^2 I$, and the magnetization $M = n - LCl^2 I$, where $n_{LC} = 1/V_{LC} = 1/a_x a_y a_z$ is the density of LC circuits defined by the lattice constants a_i. Finally, using the magnetic susceptibility Eq. (1.87), and $\mu(\omega) = 1 + \chi(\omega)$, we get

$$\mu(\omega) = 1 + \frac{\mathcal{F}\omega^2}{\omega_{LC}^2 - \omega^2 - i\gamma_R \omega} \tag{1.93}$$

Apart from the ω^2 numerator, Eq. (1.93) represents a damped Lorentz-oscillator resonance, with the undamped resonance frequency ω_{LC} according to Eq. (1.88) and

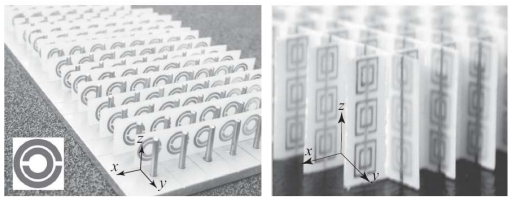

Figure 1.9: First experimental LHM structures, constituted of TWs and SRRs, introduced by the team of UCSD. (a) Monodimensionally LHM structure of [1]. (b) Bidimensionally LHM structure of [7].

the damping due to the Ohmic resistance $\gamma_R = R/L$. Therefore, this model of the SRR can be seen as the magnetic analogue of the usual electric Lorentz oscillator model. The prefactors have been merged into the dimensionless quantity $\mathcal{F}$ with

$$0 \leq \mathcal{F} = \frac{l^2 t}{a_x a_y a_z} = 1 \tag{1.94}$$

Obviously, this can be interpreted as a filling fraction, where the upper bound $\mathcal{F} = 1$ is reached when neighboring SRRs touch each other. If we make the transition to a closed ring with $d \to 0$, we get $\omega_{LC} \to 0$, and Eq. (1.93) reduces to

$$\mu(\omega) = 1 - \mathcal{F} \geq 0. \tag{1.95}$$

Thus, this simple model predicts that without the split in the ring it is not possible to obtain $\mu(\omega) < 0$. However, one has to keep in mind that we have neglected the interaction among the SRRs, which is an allowed assumption as long as $\mathcal{F} \ll 1$.

1.10 Experiments with negative refraction

Smith et al. combined the thin wire and SRR structures of Pendry into the composite structure shown in Fig. 1.9(a), which represented the first experimental LHM prototype. The arguments in [1] consisted of the following: 1) designing a thin wire structure and a SRR structure with overlapping frequency ranges of negative permittivity and permeability; 2) combining the two structures into a composite thin wire-SRR structure, which is shown in Fig. 1.9(a); and 3) launching an electromagnetic wave $e^{i\beta r}$ through the structure and concluding from a fact that a passband (or maximum transmission coefficient, experimentally) appears in the frequency range of interest proves that the constitutive parameters are simultaneously negative in this range on the basis of the fact that $\beta = nk_0 = \pm\sqrt{\epsilon_r \mu_r}$ has to be real in a passband. Although the arguments of [1] were questionable, because it ignored the fact that

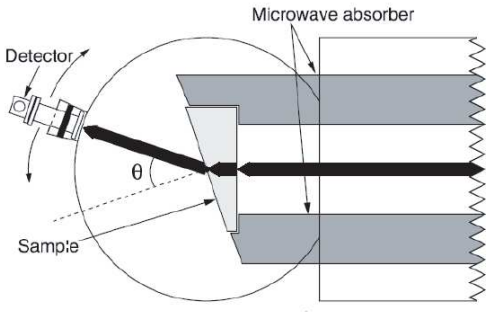

Figure 1.10: Experimental setup used in [7] for the demonstration of left-handedness of the thin wire-SRR structure of Fig. 1.9(b) at around 5 GHz. "The sample and the microwave absorber were placed between top and bottom parallel, circular aluminum plates spaced 1.2 cm apart. The radius of the circular plates was 15 cm. The black arrows represent the microwave beam as would be refracted by a positive index sample. The detector was rotated around the circumference of the circle in 1.5. steps, and the transmitted power spectrum was measured as a function of angle, θ, from the interface normal. The detector was a waveguide to coaxial adapter attached to a standard X-band waveguide, whose opening was 2.3 cm in the plane of the circular plates. θ as shown is negative in this figure. After Ref. [7].

coupling interactions between the two constituent structures could yield properties totally different from the superposition of the properties of each structure taken separately, a vivid experimental demonstration of the LHM nature of the thin wire−SRR was provided in [7]. In this paper, the thin wire−SRR structure of Fig. 1.9(b) was cut into a wedge−shaped piece of metamaterials and inserted into the experimental apparatus depicted in Fig. 1.10. Lefthandedness of the thin wire−SRR structure was evidenced by the fact that a maximum of the transmission coefficient was measured in the negative angle (below the normal in the figure) with respect to the interface of the wedge, whereas a maximum in the positive angle (above the normal) was measured, as expected, when the wedge was replaced by a regular piece of teflon with identical shape. The result reported was in qualitative and quantitative agreement with Snell's law, which reads $k_I \sin\theta_I = k_{II} \sin\theta_{II}$, or, if the two media are isotropic (so that $k_I = n_I k_0$ and $k_{II} = n_{II} k_0$), $n_I sin\theta_I = n_{II} sin\theta_{II}$ where k_i , n_i, and θ_i represent the wavenumber, refractive index, and angle of the ray from the normal to the interface, respectively, in each of the two media considered. The metamaterials described here are anisotropic and characterized by uniaxial permittivity and permeability tensors

$$[\epsilon] = \begin{bmatrix} \epsilon_{xx} & 0 & 0 \\ 0 & \epsilon_{yy} & 0 \\ 0 & 0 & \epsilon_{zz} \end{bmatrix} \tag{1.96}$$

$$[\mu] = \begin{bmatrix} \mu_{xx} & 0 & 0 \\ 0 & \mu_{yy} & 0 \\ 0 & 0 & \mu_{zz} \end{bmatrix} \tag{1.97}$$

The structure shown in Fig. 1.9(a) is monodimensionally LHM, since only one direction is allowed for the doublet (E,H); we have $\epsilon_{xx}(\omega < \omega_{pe}) < 0$ and $\epsilon_{yy} = \epsilon_{zz} > 0$, $\mu_{xx}(\omega_{0m} < \omega < \omega_{pm}) < 0$ and $\mu_{yy} = \mu_{zz} > 0$. The structure shown in Fig. 1.9(b) is bidimensionally LHM because, although E has to be directed along the axis of the wires, two directions are possible for H; then $[\epsilon]$ is unchanged, but $\mu_{xx}, \mu_{yy} < 0$ for $\omega_{0m} < \omega < \omega_{pm}$ and $\mu_{zz} > 0$.

These initial experiments in the range of microwave (GHz) had huge losses and the initial controversy about negative refraction was based on the fact that the zone of negative refraction coincided with that where the prism was thinner and in consequence less lossy. However, negative refraction was finally admitted by the scientific community when higher transmission was obtained in subsequent experiments, for example Aydin et al [38] observed negative refraction at 3.9 GHz with transmission loss $1 - T$ of 1.2dB. In the process to carry out the metamaterials at optical frequencies there are several experiments from the mm wavelength [32] to terahertz [33], mid-infrared [34] and near-infrared [35], also the lower frequencies as radio frequency have been developed [31]. Recently, the "fishnet" structure has gotten hopefully experimental results in the optical frequencies with an estimate figure of merit (FOM$=-Re(n)/|Im(n)| = 3.5$) at $\lambda = 1775nm$ and $n = -1.4$ [36]. This "fishnet"

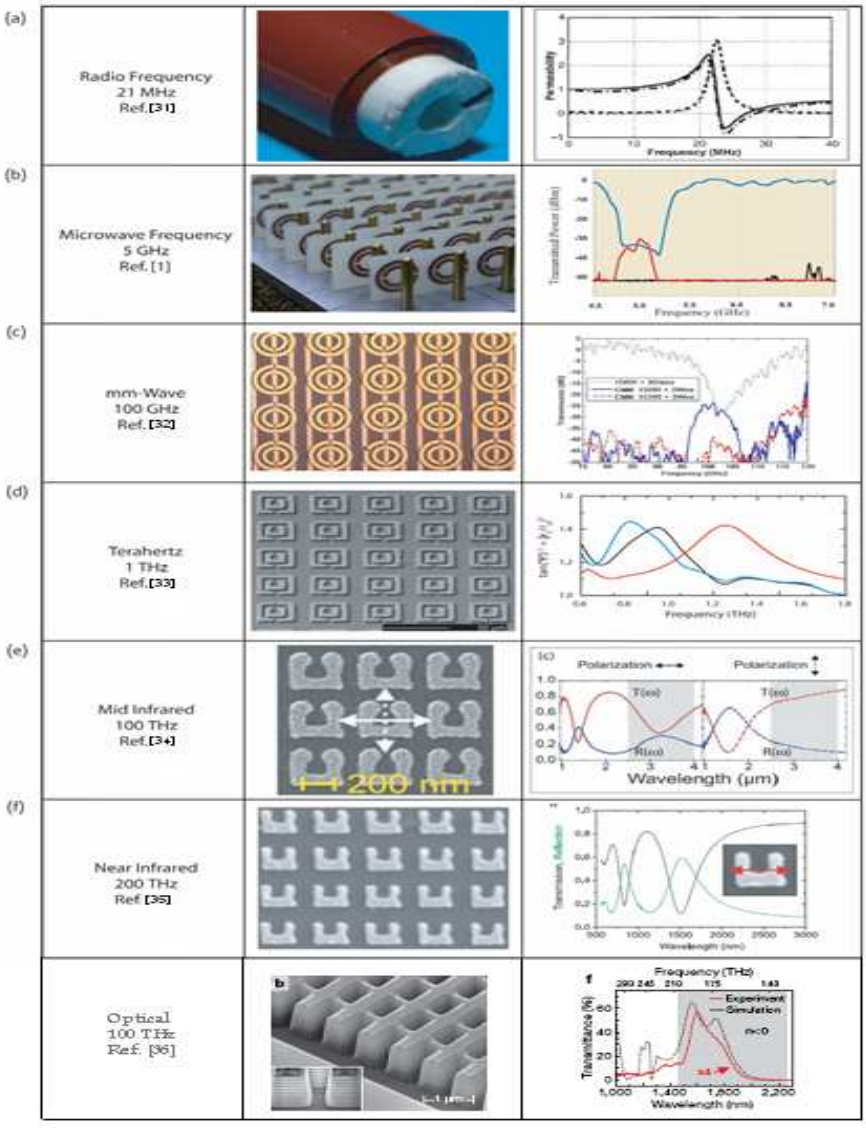

Figure 1.11: In the left column we detail the frequency range in which each metamaterial was demonstrated and note the reference number. The middle column shows a photo of the metamaterial from each publication, and the third column shows some data detailing the metamaterial response. The top row is an investigation of "swiss-roll"-type magnetic structures to guide magnetic flux in magnetic resonance imaging machines [31]. The second row is the original work in which LHM materials were discovered at microwave frequencies [1]. The third row shows some recent work on metamaterials at millimeter-wave frequencies [32]. The next row details the first work extending metamaterials out of the microwave into the terahertz regime [33]. The next two rows show further extension of the SRR magnetic metamaterial medium to MIR and NIR frequencies from Wegener's group [34],[35]. And the bottom row shows the "fishnet" structure for optical frequencies [36]. Figure adapted from [37].

structure consist in staple structures for magnetic [39] resonance and a perpendicular array of metallic wires along the electrical field direction for electrical response, in this way, we obtain a L−C circuit with an inductance associated with both the loop and the electron inertia, and a capacitance formed by the staple footings [40](see Fig. 1.11).

Further applications have been proposed using the so−called *transformation optics* in which a medium is designed with specific values of ϵ and μ throughout its geometry. In this way, recent works speculate with the possibility of rendering invisibility (or cloaking) [41], beam splitting [42], and directional antennas [43].

A second approach to construct negative index metamaterials is based on the concept of transmission line structures, which are common in electrical engineering applications. This approach has been described by Eleftheriades et al. in 2002 [44]. These structures consist of two-dimensional transmission-line (TL) grids loaded with series capacitors (C) and shunt inductors (L) [44]. Using this L-C loaded TL approach, negative refraction [44] and focusing was demonstrated at microwave frequencies [44, 45]. Radiating versions of these media have been used to experimentally demonstrate backward-wave radiation in free space, a characteristic analogue to reversed Cherenkov radiation [46]. The focusing reported in [44, 45] was obtained by lenses utilizing a single interface between a left-handed medium and a homogeneous dielectric. Imaging beyond the diffraction limit could not clearly be observed with these lenses. Subsequently, planar slabs (having two interfaces) of L-C loaded TL left-handed media were theoretically shown to enhance the amplitudes of evanescent waves [47, 48] and to focus propagation waves with subwavelength resolution [48]. In a later study, these theoretical findings were experimentally confirmed [49].

A third approach to obtaining the phenomena of negative refraction and imaging by planar surfaces is to use photonic crystals. By contrast to metamaterials as described above, photonic crystals are periodic structures typically composed of insulators. Therefore they can exhibit low losses, even at the higher (optical) frequencies, a property that can be important in applications. In photonic crystals, the size and spacing of the scattering elements are on the order of the electromagnetic wavelength of interest. Hence, a photonic crystal cannot be regarded as a homogeneous medium and hence its properties cannot be described by an effective permittivity and permeability. Therefore, these structures present several differences in the imaging process. (See chapter 3 and 4).

Chapter 2

Consequence of losses in metamaterials

2.1 Motivation

An important problem with so far designed metamaterials is that they all have a large amount of metal components which produce much absorption and losses of the transmitted wave. In order to get a realistic picture, in this chapter we will analyze how these losses affect imaging and other processes versus the distance of the source with respect the metamaterial, as well as one varies wavelength and the refractive index from $n = -1$.

2.2 Introduction

We saw in chapter 1 that there has been a great deal of effort in studying both experimentally [1], [50] and theoretically [51, 52, 53, 54, 55, 56, 57] the possibility of obtaining negative refraction at microwave frequencies negative index media or LHM, characterized by a negative permittivity ϵ, permeability μ and refractive index n [2]. Since these media do not occur in nature, composite structures of metallic wires and rings of millimeter size were constructed [1], [50] to demonstrate their effect in the microwave region. To this end, a sample with a prism shape was employed. Initial questions [55], [56] on the possible role of absorption of these structures and measurements in the near field region, both of which could affect or even obliterate the observation of a neat refraction, have subsequently been addressed by detection farther from samples and by either attempting to reduce absorption effects [58], [59], or by making separate measurements at two different angled prisms [60].

In addition to absorption, the experiments have been carried out with LHM samples whose sizes (some centimeters) are not much larger than the wavelength (which is about 3 cm). Therefore, to a certain extent they behave in free space like particles for

the microwaves and, hence, scattering and diffraction effects from their edges, should be important. Thus, in principle, one should expect that the transmitted wavefront will have a complicated structure in which not a single beam direction of propagation can be assessed. However, introducing these samples in a waveguide configuration with absorbing walls, like in the experiments of Refs. [1] and [60] should significantly reduce these effects, thus conveying a cleaner main propagation direction to the transmitted beam. Nonetheless, in previous works these questions, as well as the role of different amounts of absorption, have not been fully addressed.

Another characteristic that has been put forward of LHMs is the property of flat slabs of index inverse to that of the surrounding medium, to produce focusing [2]. This has also been the subject of discussion after it was proposed [6] that such a LHM slab could focus with resolution beyond the half wavelength limit through amplification of evanescent waves. Limitations to this effect were subsequently argued [56], [16, 61, 62, 63, 64, 65, 45]. However, the observation of focusing in a LHM slab has so far appeared swamped by high absorption [60] and thus the obtained focus had not a sharp pattern. In addition, the position of the focus did not correspond to what theory would predict for a real refractive index and thus it was questioned the role that either absorption or measurements conditions might have in this respect [66].

In this chapter we shall address the diffraction and scattering effects versus those of refraction in prisms like those used in Ref.[60]. In this way, we analyze, numerically by means of finite elements (see appendix A), further the consequences of that experiment of [60]. We shall show the influence of scattering on the difficulty to observe a refraction direction when those prisms are in a free space environment, and then, by contrast, we shall show how these effects are minimized when the prisms are placed in a waveguide environment with absorbing walls like in configuration used in [60]. Also, the presence of losses in the LHM prisms are accounted for in establishing the refraction law. We shall see that, in general, these losses introduce directions of phase propagation and directions of constant amplitude which are perpendicular to each other in the air. However, we shall show that for the refractive index of the samples used in experiments such as those of Ref. [60], the deviation introduced by the imaginary parts of the refractive index upon the lossless Snell's law are not appreciable.

Further, we shall analyze the effect on focusing of the refractive index of the slabs used in the experiments of Ref. [60]. Thus, we shall study the deviations obtained from those samples of the ideal surface impedance matching with vacuum (i.e. of refractive index -1). In this respect, we shall also address the effect of absorption upon the position, size and intensity of the focus, and hence the aberrations and focus blurring due to this mismatch of the slab surface impedance matching conditions.

2.3 Refraction from an absorbing LHM prism

We first perform numerical experiments in which a plane wave at a frequency $\nu = 10.5GHz$ impinges from the bottom onto a prism, either lossless or absorbing, of LHM in free space (see Figs. 2.1(a) and (c)). We consider the LHM effective complex refractive index $\hat{n}_2 = n_2(1+i\kappa_2)$ [1], κ_2 being the attenuation index [10], and we assume $n_2 = -0.35$, a value similar to that of the samples used in [60].

Since the dimensions of the prism and those of the wavelength are comparable, diffraction and scattering effects are large, so that it is impossible to distinguish a neat refracted beam propagation direction. This situation is improved by placing the prism between absorbing walls in a waveguide configuration (Figs. 2.1(b),(d) illustrate the difference with the previous free-space configuration). On the other hand, Figs. 2.1(c) and 2.1(d) show the large losses of the transmitted wave occurring in the absorbing samples, even within distances that are not much longer than the wavelength.

Neglecting a non-instantaneous response of the medium to excitations, a snapshot of the time-harmonic electric field $E = |E|\cos(\phi + \omega t)$ ($\omega = 2\pi\nu$) at time t_0 is shown in Fig. 2.2. ϕ represents the phase of E.

Next, we address the effect of prism losses on the refraction law at the tilted exit face. In the following analysis we aim to understand the purely refractive effect, aside from diffraction and scattering phenomena associated to the finite size of the prism faces. This refraction is better observed with the prism in the absorbing wall waveguide configuration. For a normally incident plane wave on the entrance interface of the prism, it results a transmitted homogeneous wave propagating in the same direction. Then arriving at the tilted face at an angle of incidence θ_i, which is equal to the real angle of the prism φ. Therefore, if $k(\vec{r}\cdot\vec{s^t})$ is the phase of the plane wave transmitted into the vacuum, ($k\vec{s^t}$ denotes the wavevector), we have at the exit interface:

$$s_x^t = \sin\theta_t = n_2(1+i\kappa_2)\sin\theta_i, \tag{2.1}$$

$$s_z^t = \cos\theta_t = \left(1-\sin^2\theta_t\right)^{1/2} = \left(1-n_2^2\left(1-\kappa_2^2\right)\sin^2\theta_i - i2n_2^2\kappa_2\sin^2\theta_i\right)^{1/2}. \tag{2.2}$$

Eq. (2.17) is the refraction law. It is convenient to write [10]:

$$\cos\theta_t = q\exp(i\gamma). \tag{2.3}$$

Then:

$$q^2\cos 2\gamma = 1 - n_2^2\left(1-\kappa_2^2\right)\sin^2\theta_i, \tag{2.4}$$

$$q^2\sin 2\gamma = -2n_2^2\kappa_2\sin^2\theta_i. \tag{2.5}$$

[1] Here we use the the notation of Ref. [10] where $\kappa = 1/FOM$. From section 2.5 we use again the notation $n = n_1 + in_2$

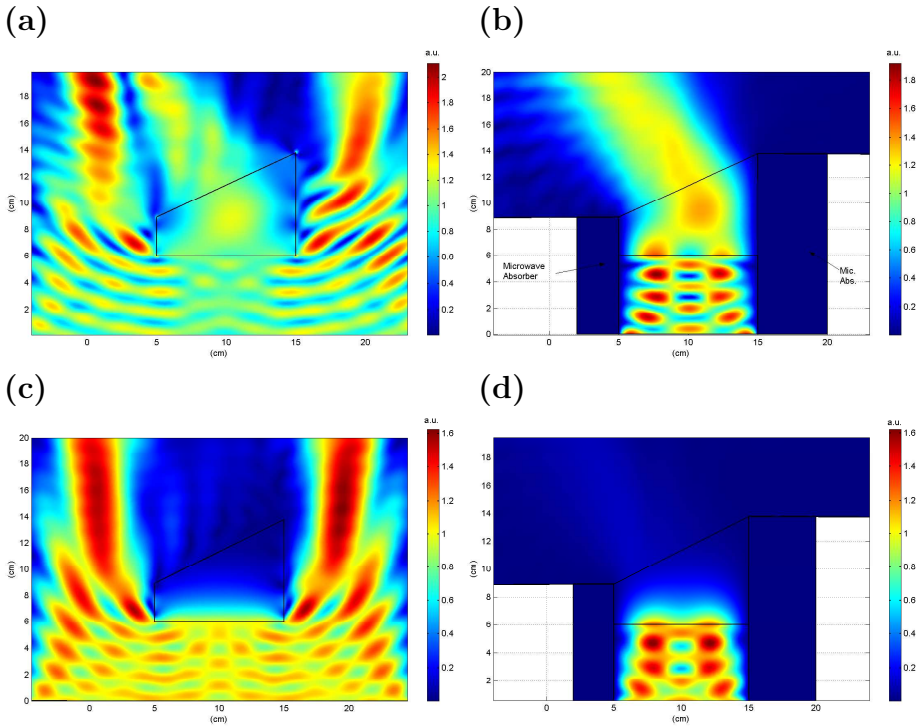

Figure 2.1: Maps of the modulus of the total electric field for (a) a lossless prism ($n_2 = -0.35$) in free vacuum environment and (b) the same prism in a waveguide of absorbing walls, illuminated by a plane wave from below of $\lambda = 3cm$; (c) and (d) the same as (a),(b), respectively, but with an absorbing prism ($n_2\kappa_2 = 0.25$). The dimensions of the prism are seen in the horizontal and vertical axes.

So that:

$$k(\vec{r}\cdot\vec{s^t}) = \frac{\omega}{c}\left(xs_x^t + zs_z^t\right) = \frac{\omega}{c}\left[xn_2\sin\theta_i + zq\cos\gamma + i\left(xn_2\kappa_2\sin\theta_i + zq\sin\gamma\right)\right]. \quad (2.6)$$

From Eq. (2.6) we see that the planes of constant phase are:

$$xn_2\sin\theta_i + zq\cos\gamma = c_1, \quad (2.7)$$

while the planes of constant amplitude are given by:

$$xn_2\kappa_2\sin\theta_i + zq\sin\gamma = c_2. \quad (2.8)$$

c_1 and c_2 being real constants. Due to Eq. (2.5), the planes of Eqs.(2.7) and (2.8) are orthogonal to each other, and the normal to the planes of constant phase makes an angle θ_t' with the interface normal:

$$\sin\theta_t' = \frac{n_2\sin\theta_i}{\sqrt{n_2^2\sin^2\theta_i + q^2\cos^2\gamma}}. \quad (2.9)$$

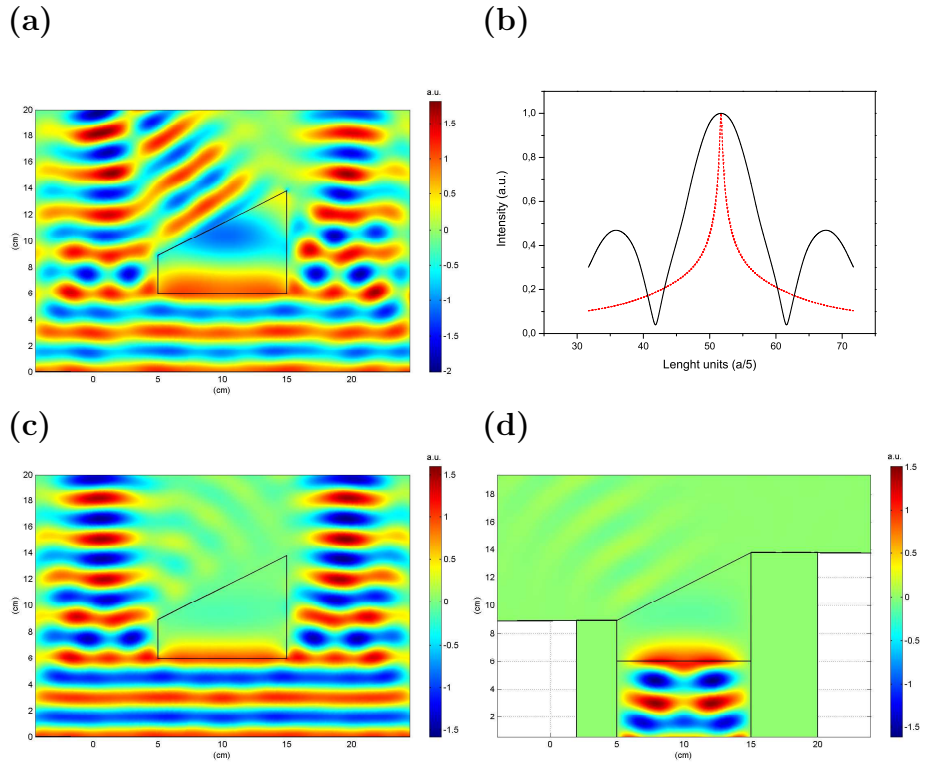

Figure 2.2: Same as Fig. 2.1 but for the electric field of the time-harmonic wave $E = |E| \cos(\phi + \omega t)$ at a time t_0.

Therefore, we observe that this angle of refraction θ_t' for the phase of the transmitted wave implies a refractive index $n' = n_2 / \left(n_2^2 \sin^2\theta_i + q^2 \cos^2\gamma\right)^{1/2}$ which depends on the incidence angle θ_i or, consistently, on the angle of the prism φ. An increase of the losses involves a decrease in the absolute value of the refraction angle θ_t' (Fig. 2.3). This figure shows that, within the range of constitutive parameters used here, this variaton of θ_t' is low and its change due to $n_2\kappa_2$ is within the systematic error of the refraction direction estimation.

Figs. 2.4 (a) and 2.4 (b) show the lines of constant amplitude $|E|$ and those of constant real part of electric field $E = |E| \cos(\phi + \omega t)$ at a time $t = t_0$ for the absorbing prism within the waveguide configuration. Fig. 2.4 (a) shows the difficulties in estimating the refraction angle from the lines of constant amplitude, due to the cross section of the wave in the guide configuration and to edge effects. This direction is better estimated from those planes of constant phase ϕ, (Fig. 2.4 (b)).

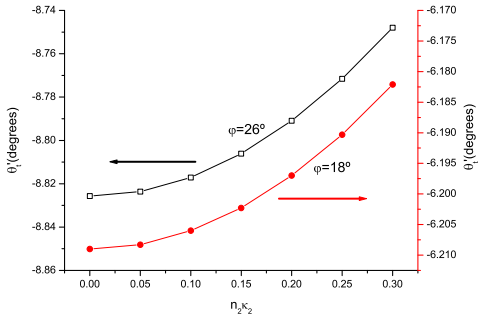

Figure 2.3: Refraction angle θ_t' versus $n_2\kappa_2$ for prisms with φ =18 and 26 degrees ($n_2 = -0.35$).

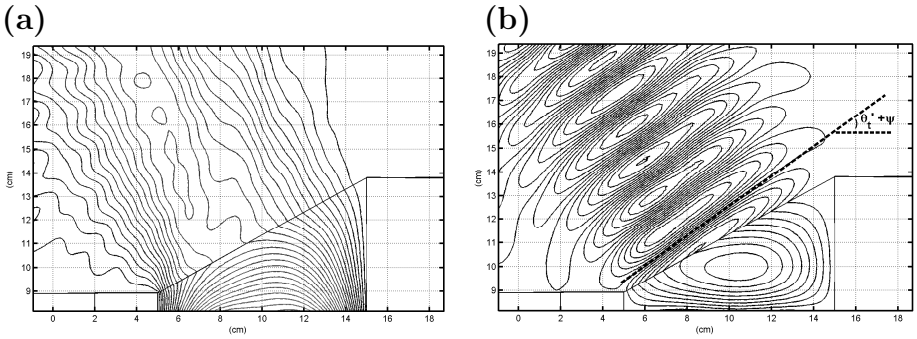

Figure 2.4: Plots of (a) lines of constant amplitude and (b) contour lines of electric field, for a LHM prism with $\hat{n}_2 = -0.35 + 0.10i$ and $\hat{\epsilon} = \hat{\mu}$.

2.4 Imaging with a rectangular LHM slab

We next consider a rectangular slab of lossy LHM , ($n_2\kappa_2 = -0.35$) of thickness 6 cm with a point source at 2 cm from its first interface (cf. Fig. 2.5), like in the experiment of Ref. [60]. In that reference, the role of the losses in the focusing process was not discussed we shall do it next. From Fig. 1 of Ref. [60] we estimate those losses approximately: $n_2\kappa_2 = 0.25$.

The configuration employed is with matched boundary conditions at the vertical boundaries of the slab, which is equivalent to sandwiching the slab across a waveguide of absorbing walls.

We next calculate how the imaginary part of the slab refractive index $n_2\kappa_2$ affects the direction of propagation of the refracted wave, and in turn to the location of the focus. Let a plane wave be incident on the slab:

$$E_i = E_0 e^{i\vec{k}_i\cdot\vec{r}} = E_0 e^{i\frac{\omega}{c}(xn_1\sin\theta_i + zn_1\cos\theta_i)}, \tag{2.10}$$

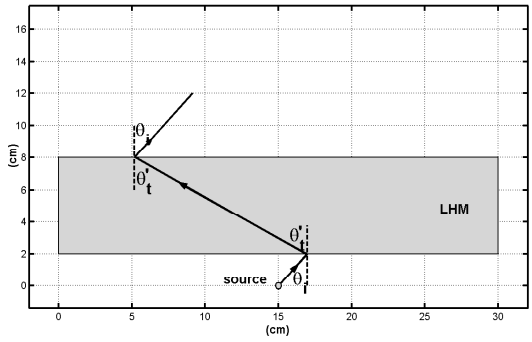

Figure 2.5: Geometry of the numerical simulation for the LHM slab.

in our case $n_1 = 1$, and θ_i is the angle of incidence. The transmitted wave into the LHM slab is:

$$E_i = E_{0t} e^{i(\vec{k}_t + i\vec{a}_t)\cdot\vec{r}}, \tag{2.11}$$

where $\vec{a}_t$ is the attenuation vector and $\vec{k}_t$ is the phase vector in the slab, whose components derived from the boundary conditions are:

$$k_i^x = k_t^x \Rightarrow \sin\theta_t' = \frac{k_i}{k_t}\sin\theta_i, \tag{2.12}$$

$$a_t^x = 0 \Rightarrow a_t^z = a_t, \tag{2.13}$$

$\hat{n}_2 = n_2(1 + i\kappa_2)$ is the complex refractive index of the LHM slab. Then k_t becomes:

$$k_t = k_i \left\{ \frac{1}{2} \left[\sqrt{\left(n_2^2 - n_2^2\kappa_2^2 - \sin^2\theta_i\right)^2 + \left(2n_2^2\kappa_2^2\right)^2} + n_2^2 - n_2^2\kappa_2^2 + \sin^2\theta_i \right] \right\}^{1/2}. \tag{2.14}$$

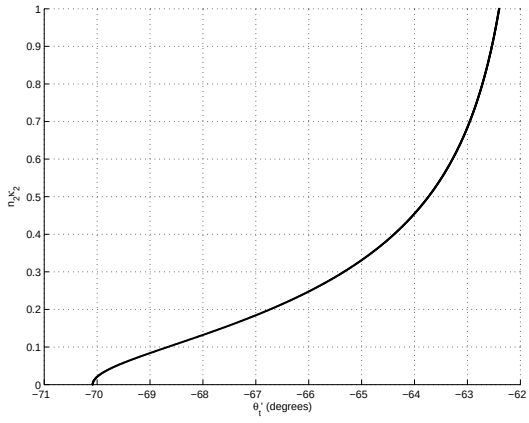

Figure 2.6: Refraction angle θ_t' versus $n_2\kappa_2$ for a $\theta_i = 15$, $n_2 = -0.35$ and $\hat{\epsilon} = \hat{\mu}$.

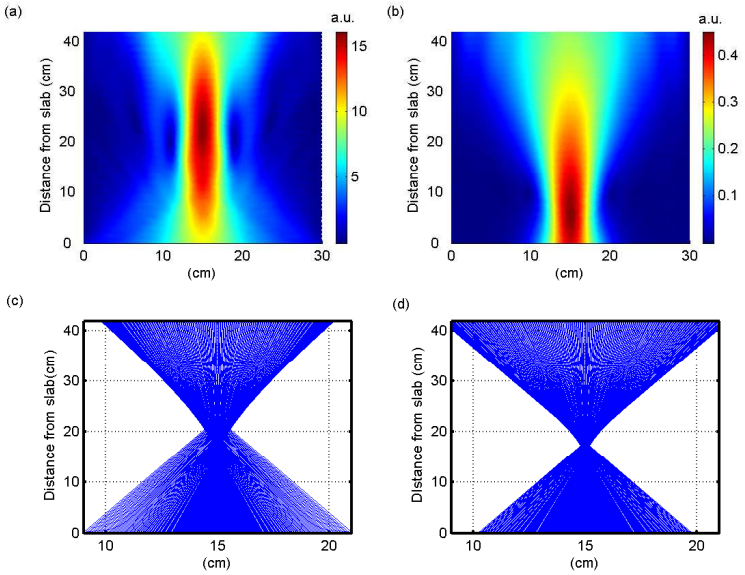

Figure 2.7: Maps of the modulus of the total electric field after passing through a LHM slab of $n_2 = -0.35$ and (a)$n_2\kappa_2 = 0.05$ (b)$n_2\kappa_2 = 0.25$ [compare with Fig. 3(b) of Ref. [60]], $\hat{\epsilon} = \hat{\mu}$ in both cases (c) and(d) ray theory for the cases of (a) and (b), respectively.

Eq. (2.12) constitutes the law of refraction for the phase vector $\vec{k}_t$. From this law, we infer that increasing the losses involves a decrease in the refraction angle into the slab θ_t' in absolute value, (Fig. 2.6), and thus the focus approaches the slab as $n_2\kappa_2$ increases. This is shown by numerical simulations in Figs. 2.7 and 2.8. In figure 2.7 we also show the ray tracing diagram on passing through the LHM slab, taking into account the refraction law given by Eq. (2.12). Thus, we show how the caustic of the focus approaches the slab as absorption increases, in accordance with the numerical simulations of Fig. 2.8. The position of the focus in Fig. 2.7.(b) is very similar to that obtained in Fig. 3(b) of Ref. [60].

Figs. 2.7(a),(b), also show the appearance of a depth of focus. The full width at half maximum (FWHM) of the image does not vary with losses. This FWHM is 1.71λ, thus showing no superresolution, as expected.

The decrease of the peak intensity of the focus normalized to the intensity of the source as the losses increase is shown in Fig. 2.9.

We have made numerical simulations by fixing the real component of the refractive index to $n_2 = -0.35$ and taking $n_2\kappa_2$ either 0.05, 0.10, 0.15. Furthermore, we consider the permeability real: $\hat{\mu} = \mu$ and we vary it. For each $\hat{n}_2$ and μ we have a value of permittivity $\hat{\epsilon}$. So that we get to vary the normalized surface impedance $\hat{z} = (\hat{\mu}/\hat{\epsilon})^{1/2} = (\mu/\hat{n}_2)$. We analyze the resulting image (Fig. 2.10).

We observe that as the permeability μ increases, the distance of the focus to the

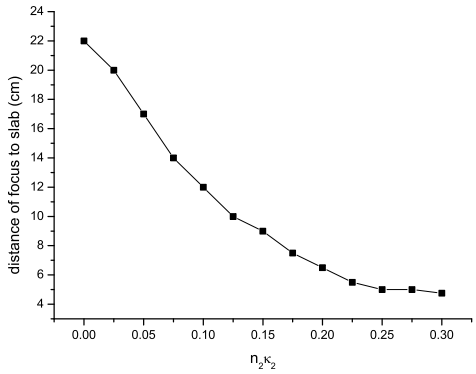

Figure 2.8: Variation of the focus position with the LHM slab absorption $n_2\kappa_2$ ($n_2 = -0.35$ and $\hat{\epsilon} = \hat{\mu}$ in all cases).

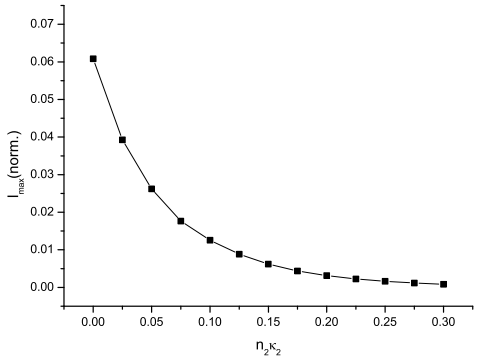

Figure 2.9: Peak intensity of the focus normalized to the source intensity versus $n_2\kappa_2$ for $n_2 = -0.35$ and $\hat{\epsilon} = \hat{\mu}$ in all cases.

slab decreases. If we consider the transmission factor of the slab at TE polarization t_{TE} for the second interface, which is given by:

$$|t_{TE}| = \left| \frac{2\cos\theta_t}{\cos\theta_t + \hat{z}_2 \cos\theta_i} \right| = \left| \frac{2}{1 + (\mu\cos\theta_i)/(\hat{n}_2\cos\theta_t)} \right|, \tag{2.15}$$

where the angles are given by Fig. 2.5, it is clear that as μ increases, the modulus of transmission factor $|t_{TE}|$ decreases. This effect is more critical at high angles and, therefore, the focus is made up mainly of paraxial rays and, consistently, decreasing the distance of the focus to the slab.

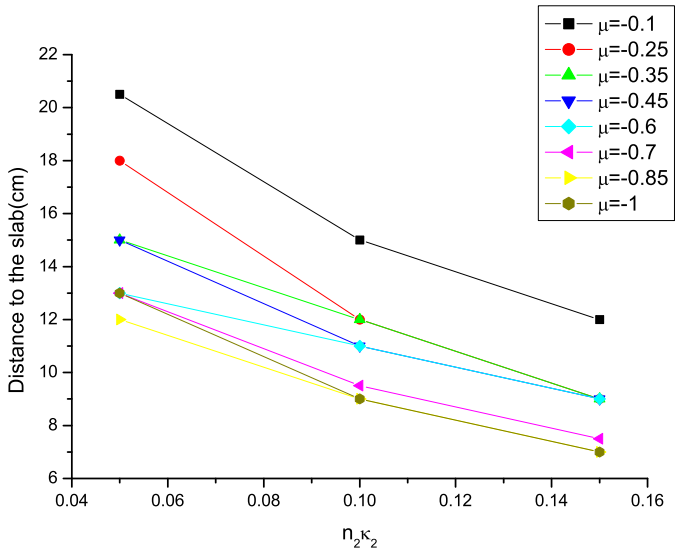

Figure 2.10: Distance of focus to slab for different values of μ as $n_2\kappa_2$ varies ($n_2 = -0.35$ in all cases).

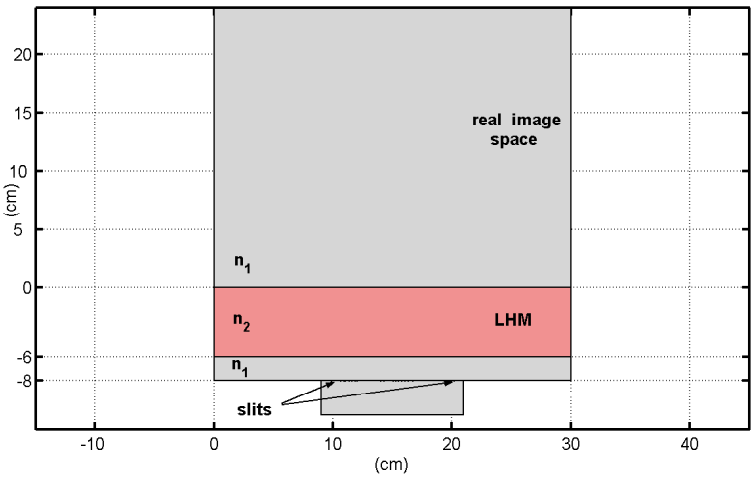

Figure 2.11: Geometry of the numerical simulation with two slits.

2.5 Analysis of the LHM slab isoplanatism

Spatial invariance, or isoplanatism, is a central property of lenses and optical systems. We next investigate the degree of isoplanatism of a LHM slab with different refractive indices.

We simulate a configuration for a slab with the properties of the experiment of Ref. [60] in front of an object constituted by two slits of width $\lambda/20$ ($\lambda = 3cm$)(Fig. 2.11). In a first simulation, the slit centers are separated 10cm, we assume that from both slits emerge the same intensity(Fig. 2.12(c)) and compare a lossless LHM slab ($\hat{n} = -0.35$) (Figs. 2.12(a) and (d)) with that of $\hat{n} = -0.35 + 0.25i$ (Figs. 2.12.(b) and (e)). Then, in a second more stringent test, we consider in one slit an absorber so that different intensities emerge from these slits (Fig. 2.13). Accordingly, in Figs. 2.12 and 2.13 we observe the formation of an image of the slits, which as explained above, approaches the slab as the losses increase. There is a considerable limitation of resolution, and also a lot of intensity is lost in other directions. In Fig. 2.12, we also observe additional structures in other regions above the slab.

Simulation with slits separated 5 cm shows the difficulty to resolve the two slits (Fig. 2.14 and 2.15), even though in the case in which they emit with different intensity, there is a recovery of their image. In both cases of objects, isoplanatism is slightly lost as higher resolution of details is sought. Namely, Fourier optics loses validity as the dimensions of the slab and those of the wavelength become comparable, as expected.

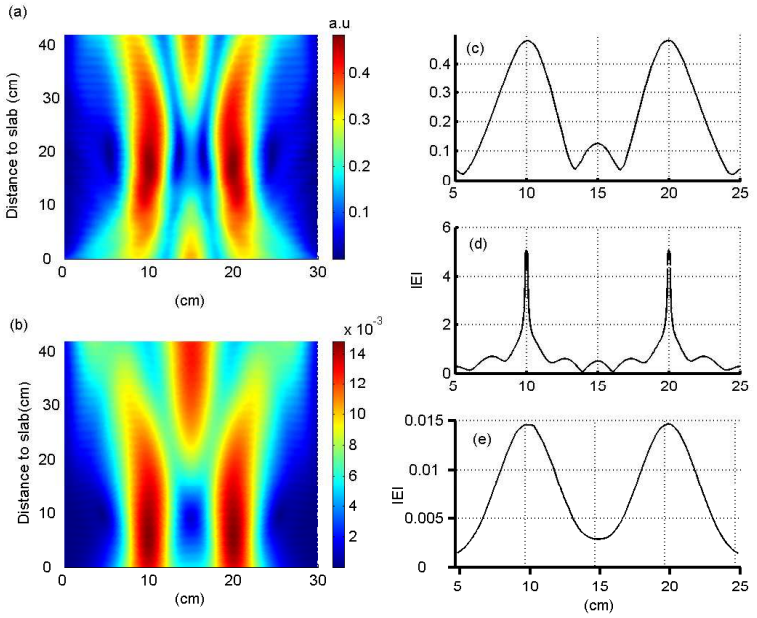

Figure 2.12: Modulus of electric field after passing through the LHM slab according to the geometry of Fig. 2.11 for (a)$n_2\kappa_2 = 0$ and (b)$n_2\kappa_2 = 0.25$ ($n_2 = -0.35$ and $\hat{\epsilon} = \hat{\mu}$). the distance between the centers of the slits is 10cm. (d) Object cross section along the slit plane and (c) cross section of (a) along the image plane situated at 17cm from the slab and (e) cross section of (b) along the image plane situated to 5cm from slab.

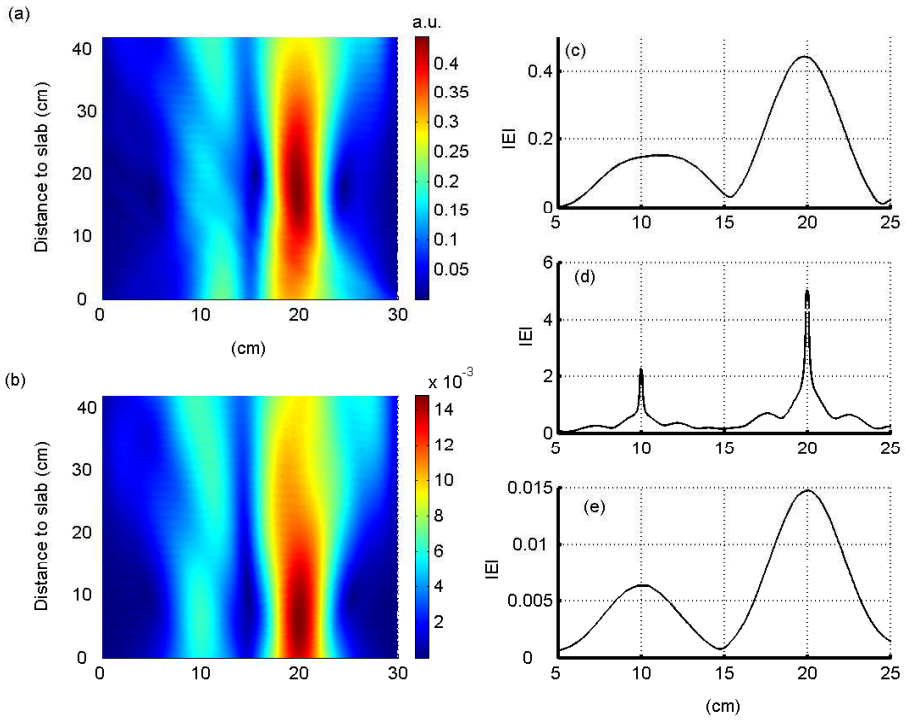

Figure 2.13: Same as Fig. 2.12 but for two slits of different intensity.

Finally, we show by contrast with the former cases a more favorable situation of a slab with a refractive index $\hat{n}_2 = -1.0454 + 0.0041i$ such as for the material used in the experiment of Ref. [58]. This case would be very similar to the one originally considered by Veselago [2] (see also [6]). The small imaginary part of $\hat{n}_2$ regularizes divergencies at the exit interface of the slab that otherwise would exist for the refractive index strictly being $\hat{n}_2 = -1$. Now, we consider that the slits are separated either 10cm (3.33λ) or 3cm (λ). In this case, (see Figs. 2.16-2.19), the two slits are sharply resolved, even achieving some degree of superresolution, although the peak positions in the image appear slightly altered with respect to those of the object slits, this is again indicative of some loss of isoplanatism due to diffraction.

Additionally, Fig. 2.19(b) shows the image from finite width slabs of 40, 25 and 15cm. Thus, we see that there is not an appreciable resolution loss by reducing the width of the slab within these values, even though in the cases of 25 and 15cm the edges of the slab are not in contact with the waveguide absorbing walls.

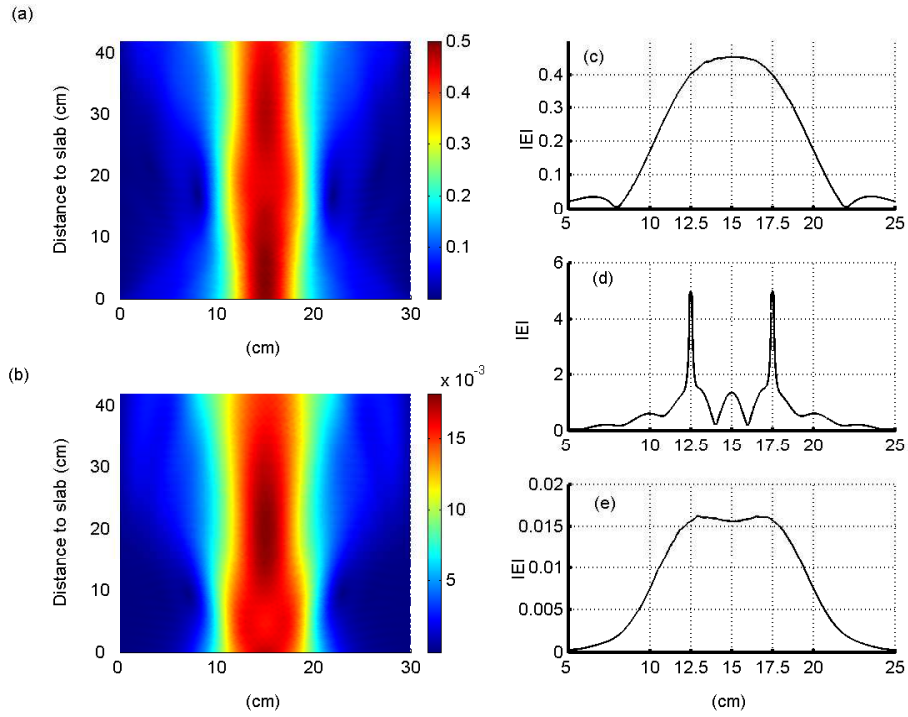

Figure 2.14: Same as Fig. 2.12 but for slits separated 5cm.

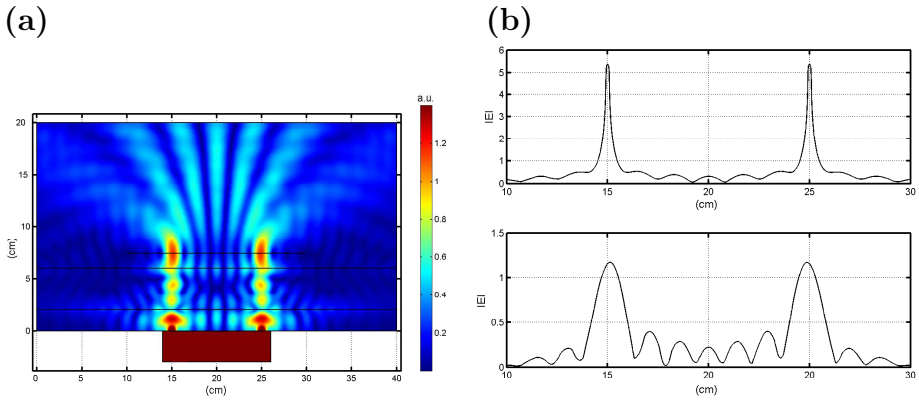

Figure 2.16: (a) Map of the electric field modulus for two slits separated 10cm in front of a LHM slab ($\hat{n}_2 = -1.0454 + 0.0041i$). (b) Distribution of electric field modulus along the slits (top) and along the image plane after the slab at 1.4cm from the last interface (bottom).

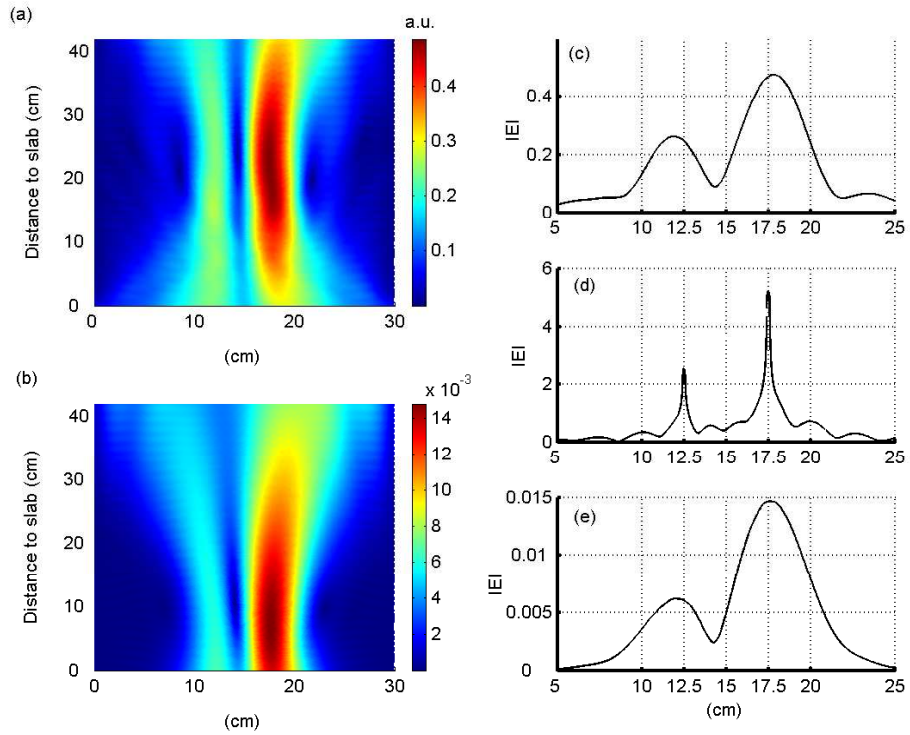

Figure 2.15: Same as Fig. 2.13 but for slits separated 5cm.

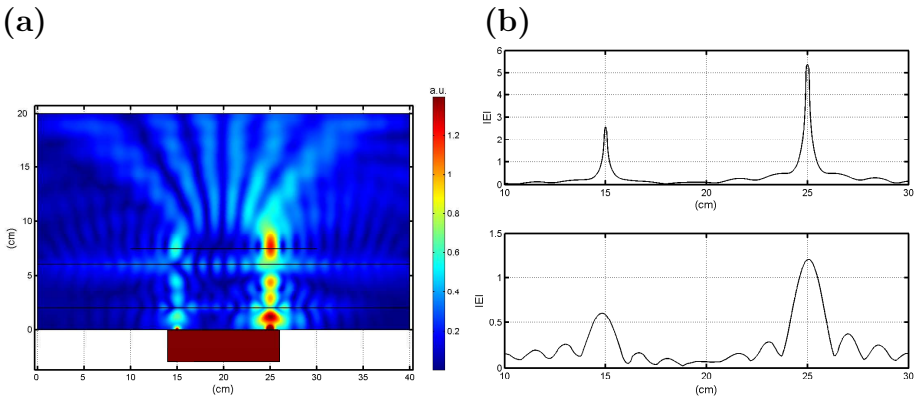

Figure 2.17: Same as Fig. 2.16 but for different intensity in the slits.

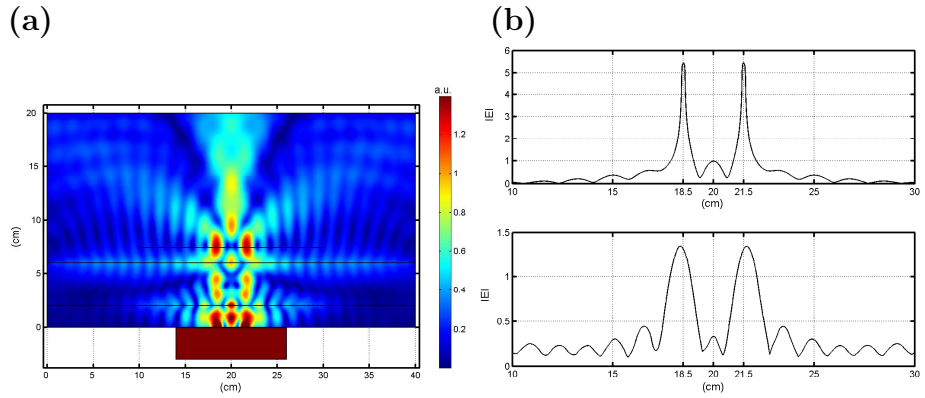

Figure 2.18: Same as Fig. 2.16 but for slits separated 3cm.

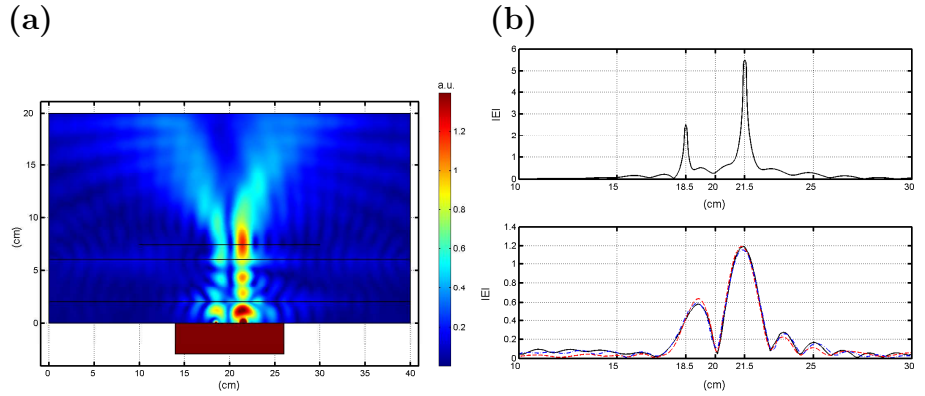

Figure 2.19: Same as Fig. 2.17 but for slits separated 3cm. In (b) black solid curve is for a slab 40cm width, blue dashed-point curve correspond to a slab 25cm width and red dashed curve is for a slab 15cm width.

2.6 Transfer function of LHM slabs

It is worth analyzing the transfer function of a LHM slab whose constitutive parameters are very close to those of an ideal lens: $\hat{\epsilon} = \hat{\mu} = -1 + i0.001$, which involves that the complex refractive index will be $\hat{n} = -1 + i0.001$. A time harmonic dependence $\exp(i\omega t)$ for the wave is assumed. Figs. 2.20(a)-(c) show the spatial distribution of the electric field modulus when a point source, made by a narrow slit (Fig. 2.20(d)), is placed at distances $z_0 = \lambda$, $\lambda/3$ and $\lambda/6$ from the entrance surface of the slab. It is well known that any imaging system, and in particular a lens, should be space invariant, at least in a certain field region. This involves the *isoplanatic*

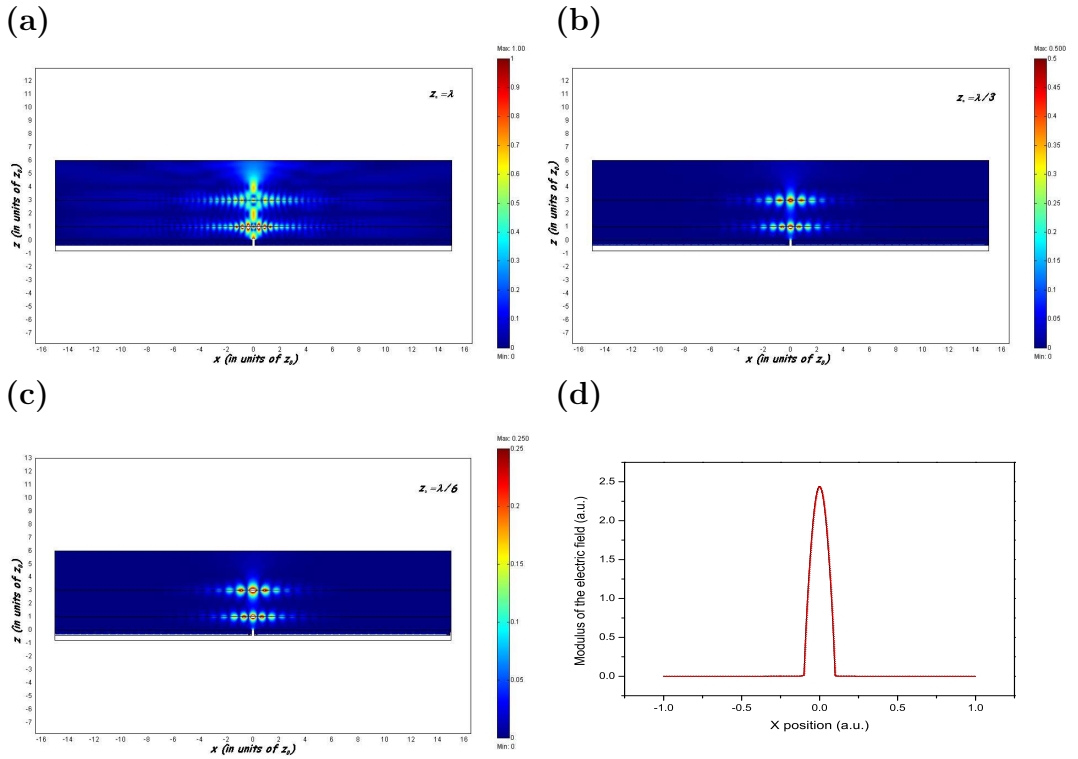

Figure 2.20: (a)-(c) Map of the modulus $|E_y|$ of the electric field for a slit emitting in front of left handed slab with $\hat{n} = -1 + i0.001$ for different distances z_0 in terms of the wavelength λ. (d) Modulus of the electric field measured on the exit plane of the slit, namely, at distance z_0 from the slab entrance interface. This magnitude is evaluated both with and without the presence of the LHM slab, both profiles are indistinguishable from each other.

condition, according to which the image field distribution $i(x)$ is given in terms of the object wavefront distribution $o(x)$ by the convolution [10], [67]:

$$i(x) = \int o(x')P(x - x')dx'. \tag{2.16}$$

In Eq. (2.16) $P(x)$ is the point spread function of the system, or response to a point source, (i.e., $P(x)$ constitutes the wavefunction at the focus), and it allows, by Fourier transformation, to define a transfer function of the lens or optical system. This also involves that in the region of isoplanacity the response $o(x_i)P(x - x_i)$ in the detection plane to each ith sampling point $o(x_i)\delta(x - x_i)$ of the object wavefield distribution in the input plane, only depends on the difference of coordinates $x - x_i$ and not on the position x_i.

In order to test the degree of isoplanatism of this LHM slab, we carry on the

following operation: the inverse Fourier transform of this point source image $P(x)$ is performed, then this result which is the transfer function $T(u)$, is multiplied by the Fourier spectrum $O(u)$ of any extended object $o(x)$ placed at the input plane z_0. Subsequently, an inverse Fourier transform of this product should yield a field distribution $i(x)$ in the image plane according to Eq. (2.16), and this result ought to be very similar to that obtained by direct FE calculation of the propagation of this extended object wavefront through the crystal slab, in the image plane.

The corresponding transfer functions, calculated by the procedure described before, are shown in Fig. 2.21. It is observed how the width of these curves increases as z_0/λ decreases. Also, while at $z_0 = \lambda$ there is focusing inside the slab (cf. Fig. 2.20(a)), which manifests the dominant contribution of the propagating components of the wavefield, at subwavelength distances z_0 this focusing is almost imperceptible, showing the predominance of the evanescent components of the wavefield angular spectrum. In addition in Figs. 2.20(a)-(c) one sees how both the object and the image fields are spatially coupled with intensity enhancements in the entrance and exit surfaces of the slab, respectively. Both enhancements being due to the excitation of surface plasmon polaritons (SPPs) by the evanescent components of the wave, and thus being increasingly prominent as z_0/λ decreases; this is shown in Fig. 2.22. These SPPs are present for both TE and TM polarization cf. [15], and are extended in their transversal wavevector component at the frequency under study, thus being excited by a large spectrum of evanescent waves. Of course the larger excitation of these surface waves in the back interface as z_0/λ diminishes, is what broadens the bandwidth of the transfer function. Figs. 2.20(a)-(c) and 2.21 confirm it.

Figs. 2.20(a)-(c) and 2.22 also show that the distance of the focus plane to the exit surface of the slab is not well defined as z_0/λ decreases beyond 1/2. Since the image field is constituted by the distribution expelled out from the standing wave pattern of the SPP at the exit interface. This progressive lack of a focus plane as one approaches the quasi-electrostatic limit is in agreement with a similar observation of lack of intensity maximum in $z > 0$ in [68] when dealing with the image of a point source through a slab of photonic crystal of small thickness compared to the wavelength λ. The same can be said with respect to the field of the incident wave in front of the entrance surface of the slab.

One may even wonder how the effect of the standing wave in the entrance surface actually distorts the field distribution of the field in the input plane when the stationary field state is reached. However, a cross section of the field distribution below the entrance surface, as shown for the wavefield modulus in Fig. 2.20(d) for a slit source, and in Fig. 2.23(d) for an extended object, shows that for these parameters used, the resulting field pattern in this region accommodates so that the incident wavefront distribution in the input plane is not appreciably distorted by the presence of the slab interface.

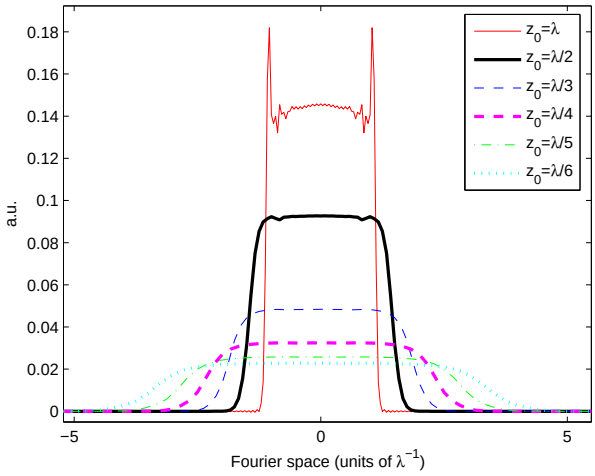

Figure 2.21: Modulus of the real part of the transfer function (Fourier transform of the image of a point source) produced by a LHM with real part of the refractive index $n_1 = -1$ and imaginary part $n_2 = 0.05$ at different distances z_0 of the source from the slab. We observe that their widths exceed those limited by the Rayleigh limit of resolution $1/\lambda$.

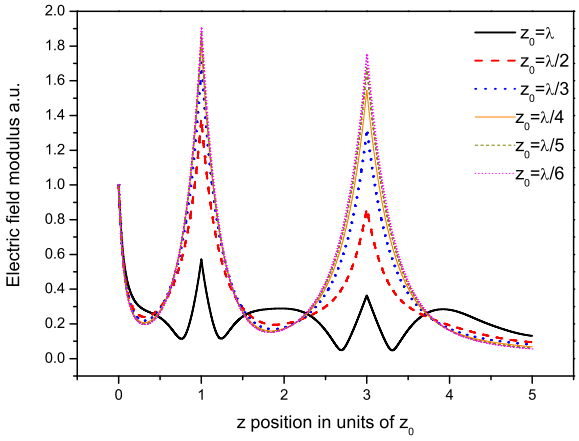

Figure 2.22: Electric field modulus $|E|$ (normalized to the value in the exit of the slit) versus z coordinate for different distances z_0 from the slit to the slab. We observe an increasing of the modulus $|E|$ on the interfaces and a suppression of the resolution in the focus along oz as z_0 decreases.

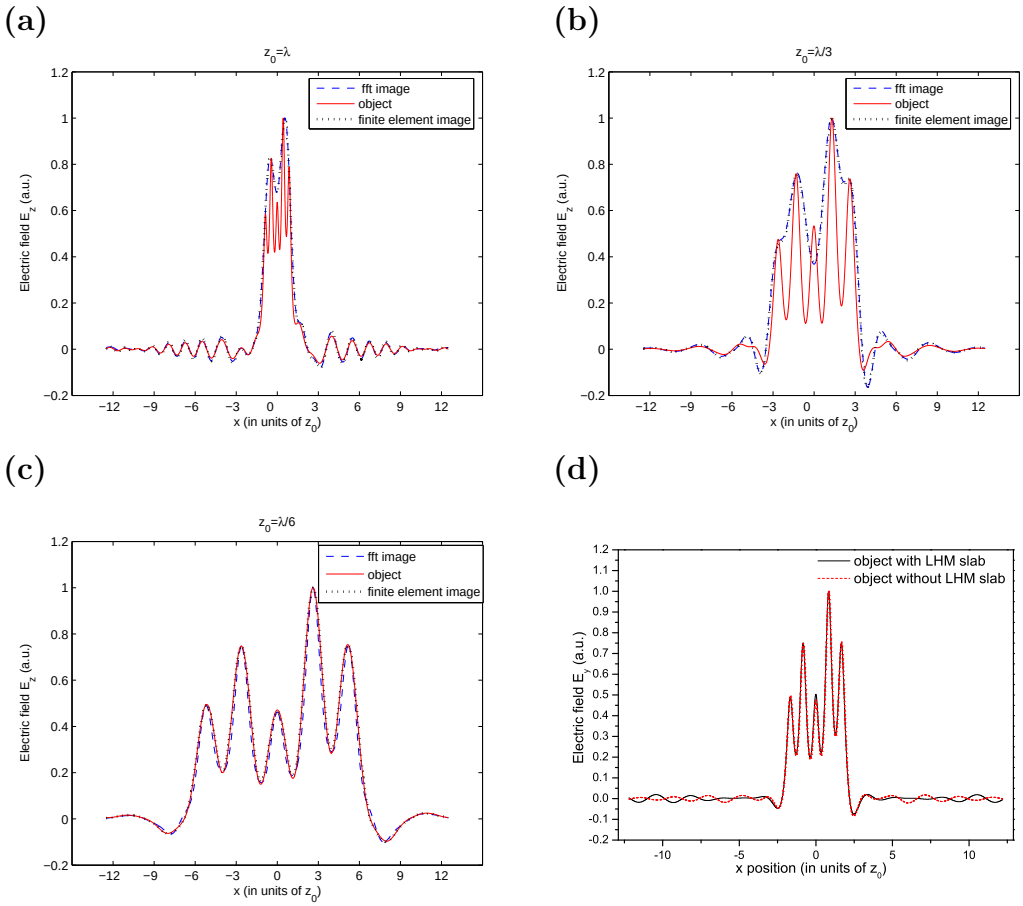

Figure 2.23: (a)-(c) Electric field amplitude E_y of an extended object containing subwavelength details (red solid line) and its image by a LHM slab for different distances z_0 and different thickness of the slab $d = 2z_0$. The image obtained via the transfer function is shown by the blue dashed line. The image obtained from the propagation simulation by the FE calculation is displayed by the black dotted line. (d) Electric field amplitude measured at distance z_0 from the slab entrance interface. This magnitude is evaluated both with and without the presence of the LHM slab (black solid line and red dashed line, respectively), both profiles are indistinguishable from each other except the slight differences in the tails.

On the other hand, Figs. 2.23(a)-(c) show the image distribution at distance z_0 from the exit surface of the slab for an incident extended object wavefront, on the input plane at distance z_0 from the entrance surface. The superresolution attained as z_0 decreases, in association with that of the corresponding transfer functions (cf Fig. 2.21) is evident. Also, in these Figs. 2.23(a)-(c) we have performed the same operation as in the PC slab, namely, a comparison between the image obtained by

FE simulation of the propagation process throughout the slab and that obtained by Fourier transformation via the transfer function. The agreement shown, even in those cases demanding superresolution, demonstrates the isoplanatism of this system in the range of distances and wavelengths employed.

2.7 Extended object and propagation scheme

All work done so far has been concentrated in the focusing characteristics of a slab for one or two point sources, however, a real lens should be able to provide images of extended objects with isoplanatic characteristics [69] this will be addressed in this section.

The extended object is a TE polarized time-harmonic electric field composed by the Fourier superposition of harmonics:

$$E_z(x) = \sum_{p=1}^{15} \left[\sin\left(\frac{p\pi x}{\ell}\right) + \cos\left(\frac{p\pi x}{\ell}\right) \right], \tag{2.17}$$

where x is the horizontal coordinate and ℓ represents the width of the slab. Fig. 2.24 shows the electric field modulus, (the values of the electric field in contiguous peaks are in phase opposition, which is the best situation to resolve them [67]). Table 2.1 shows the distance between peaks at different wavelengths used. The scheme of propagation is shown in Fig. 2.25:

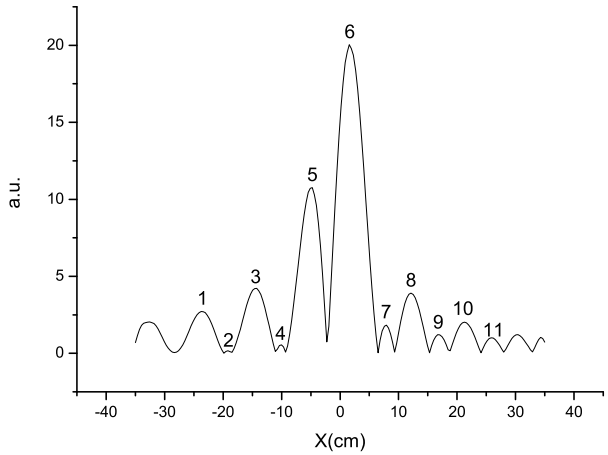

Figure 2.24: Electric field modulus of the extended object point out the distances of the peaks(cm).

Table 2.1: distance between peaks (in bold cases demanding superresolution).

peaks	1-2	2-3	3-4	4-5	5-6	6-7	7-8	8-9	9-10	10-11
distance$\Delta x(cm)$	4.4	4.8	4.3	5.1	6.7	6.1	4.3	4.7	4.4	4.8
$\Delta x(\lambda = 3cm)$	1.47λ	1.60λ	1.43λ	1.7λ	2.23λ	2.03λ	1.43λ	1.57λ	1.47λ	1.60λ
$\Delta x(\lambda = 6cm)$	0.73λ	0.80λ	0.72λ	0.85λ	1.12λ	1.02λ	0.72λ	0.78λ	0.73λ	0.80λ
$\Delta x(\lambda = 9cm)$	$\mathbf{0.49\lambda}$	0.53λ	$\mathbf{0.48\lambda}$	0.57λ	0.74λ	0.68λ	$\mathbf{0.48\lambda}$	0.52λ	$\mathbf{0.49\lambda}$	0.53λ
$\Delta x(\lambda = 12cm)$	$\mathbf{0.37\lambda}$	$\mathbf{0.40\lambda}$	$\mathbf{0.36\lambda}$	$\mathbf{0.42\lambda}$	0.56λ	0.51λ	$\mathbf{0.36\lambda}$	$\mathbf{0.39\lambda}$	$\mathbf{0.37\lambda}$	$\mathbf{0.40\lambda}$
$\Delta x(\lambda = 15cm)$	$\mathbf{0.29\lambda}$	$\mathbf{0.32\lambda}$	$\mathbf{0.29\lambda}$	$\mathbf{0.34\lambda}$	$\mathbf{0.45\lambda}$	$\mathbf{0.41\lambda}$	$\mathbf{0.29\lambda}$	$\mathbf{0.31\lambda}$	$\mathbf{0.29\lambda}$	$\mathbf{0.32\lambda}$
$\Delta x(\lambda = 18cm)$	$\mathbf{0.24\lambda}$	$\mathbf{0.26\lambda}$	$\mathbf{0.24\lambda}$	$\mathbf{0.28\lambda}$	$\mathbf{0.37\lambda}$	$\mathbf{0.34\lambda}$	$\mathbf{0.24\lambda}$	$\mathbf{0.26\lambda}$	$\mathbf{0.24\lambda}$	$\mathbf{0.26\lambda}$

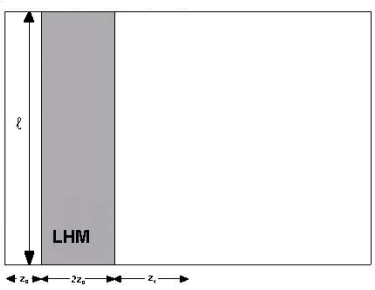

Figure 2.25: Propagation scheme. The extended object is in the left boundary at distance z_0 from the slab.(All boundaries are perfectly matched absorbing).

The extended object is at distance $z_0 = 10cm$ from the slab with thickness $d = 2z_0$ and a width $\ell = 70cm$. Its refractive index is $n = n_1 + in_2$ ($n_1 < 0$). We take the complex $\varepsilon = \mu = n$ to get a perfect matched surface impedance at normal incidence). z_1 represents the distance from the image plane to the exit face of the slab. This distance is fixed by both the real and imaginary parts of n on considering the law of refraction for the phase vector $\vec{k}_t$ in the generally lossy slab [69] (see section 2.4, Eq(2.12)and (2.14)).

2.8 Results

2.8.1 Influence of the variation of n_1

First, we slightly vary the real part of the refractive index of the left-handed slab from his archetypal value $n_1 = -1$ assuming null its imaginary part n_2.

The images obtained are represented in Fig. 2.26. We can see the loss of superresolution when the real part of n is moved from $n = -1$. We observe better resolution for the cases in which the refractive index is $n_1 < -1$ than in those situations with $n_1 > -1$, including a possible case of superresolution for $\lambda = 9cm$ for both $n_1 = -1.1$ and $n_1 = -1.2$.

This better resolution in those cases with $n_1 < -1$ is due to the larger effective aperture and to the smaller distance of the position of the focus image z_1 from the exit interface of the LHM slab.

2.8.2 Influence of the variation of n_2

Next, we fix the value of n_1 to $n_1 = -1$, and we vary the imaginary part n_2. Thus, we introduce losses in the LHM slab. Under these circumstances, in Reference [17] it was predicted a resolution

$$\Delta x = \frac{\lambda}{2s_c}, \tag{2.18}$$

where s_c is

$$s_c = \left\{ \left[\frac{\lambda}{4\pi z_0} \ln\left(\frac{2}{n_2}\right) \right]^2 + 1 \right\}^{1/2}. \tag{2.19}$$

Fig. 2.27 shows for different wavelengths the better resolution obtained from Equations (2.18) and (2.19) as z_0/λ becomes larger.

Consequently, we carry out the following numerical simulations of the imaging process whose results are shown in Fig. 2.28.

We observe that for $\lambda = 3cm$ the image manifests a loss of resolution of the peaks 2, 4 for $n_2 = 0.050$ and of the peak 7 when $n_2 = 0.250$. For $\lambda = 6cm$ the image looses the resolution of the peaks 2, 4 for $n_2 = 0.050$, the peak 7 when $n_2 = 0.125$ and of the peaks 9, 11 for $n_2 = 0.200$. And in the case $\lambda = 9cm$ the peaks 2, 4, 7 and 9 involving superresolution are lost with $n_2 = 0.100$, this being in agreement with the theory of Equations (2.18) and (2.19), since in this case $s_c = 1.0228$ and $\Delta y = 0.49\lambda$. For the cases with $\lambda > z_0$ most of the peaks involving superresolution are lost even though with very small losses in the LHM slab.

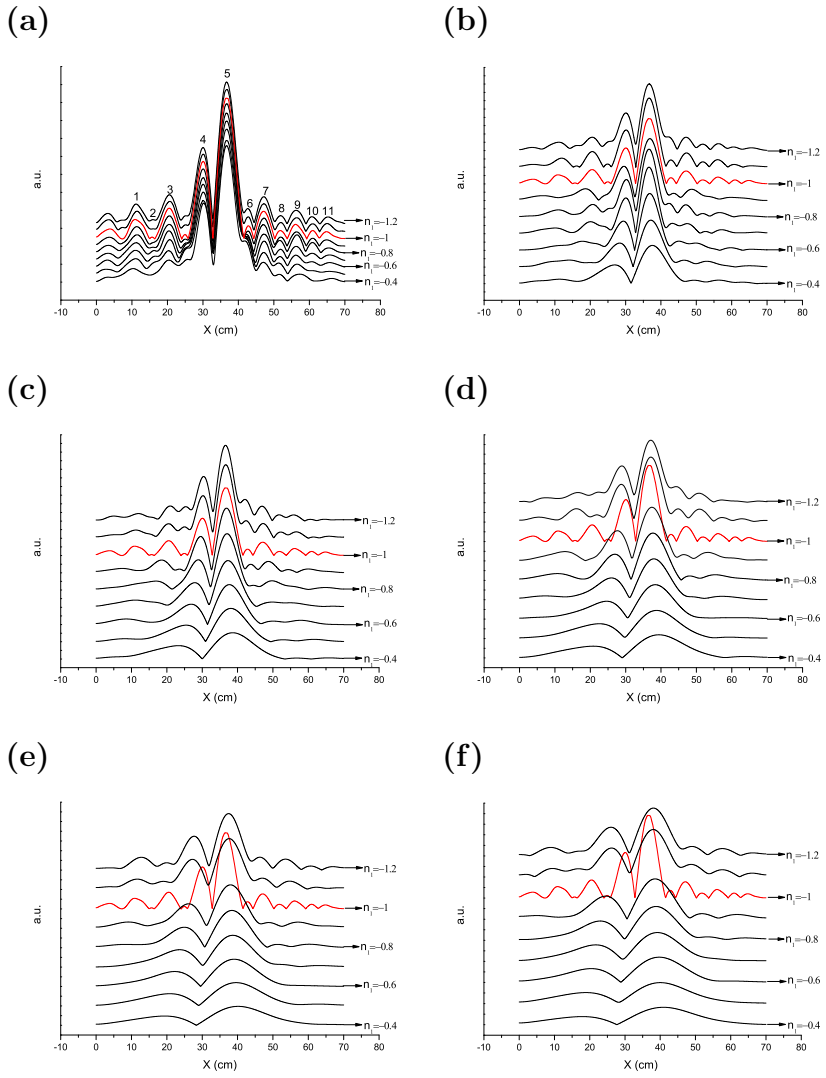

Figure 2.26: Modulus of electric field of image of the extended object of Fig. 2.24 by varying the real part n_1 of the refractive index in the cases: (a)$\lambda = 3cm$, (b)$\lambda = 6cm$, (c)$\lambda = 9cm$, (d)$\lambda = 12cm$, (e)$\lambda = 15cm$ and (f)$\lambda = 18cm$

2.9 Conclusions

Since due to the large wavelength in the microwave region, prisms samples of LHMs used in experiments are unavoidably of particle size for the incident wave, edge scattering and diffraction phenomena are of importance. We have analyzed these effects and shown how sandwiching the sample within a waveguide configuration of

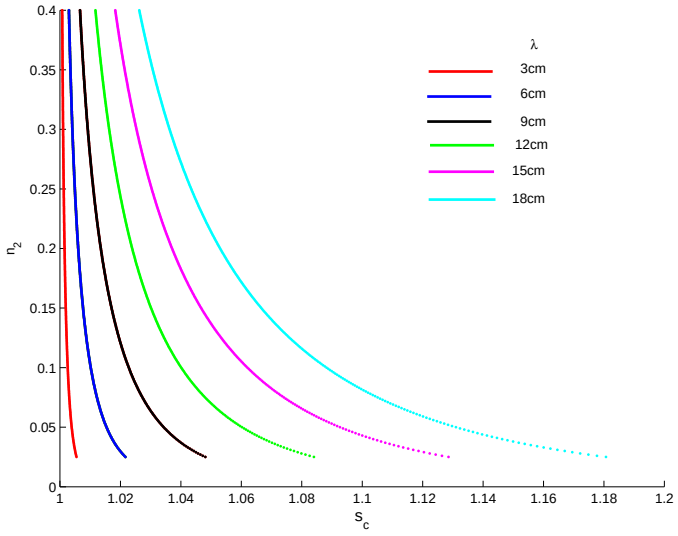

Figure 2.27: Theoretical calculation of s_c versus imaginary part of the refractive index n_2 from 0.025 to 0.4 for different wavelengths.

absorbing walls, as done in the experiments of Ref. [60], dramatically suppresses these effects, thus allowing to distinguishing a neat refraction direction within some estimation error.

We have established a refraction law for these prisms at the exit interface, which shows that, due to absorption, the refracted wave into the air is in general inhomogeneous with the phase and amplitude planes normal to each other. However, for the constitutive parameters used in the experiments so far, the alteration of the usual Snells law caused by absorption is almost negligible. Nonetheless, we believe that the special characteristics of our new refraction law due to absorption are of interest for future experiments with different constitutive parameters. Absorption, on the other hand, is shown to be quite large in these prisms, within ranges comparable to the wavelength. It is desirable that these losses can be overcome in future designs of LHMs.

This absorption has important effects on both the position and focus size produced by flat slabs. We have clarified why the focus appears closer to the slab than what one could expect from the value of the real part of the refractive index.

We have shown a model for the formation of the image of an extended object if a LHM slab is acting as a real lens, since then it should work in a regime of isoplanatism. We have analyzed the transfer function and the influence of the variation of the real part of n from -1 showing how a worsening in the resolution of the extended object appears with deviations from $n = -1$. Also we have shown in the cases with $n_1 < -1$ a better resolution than in those cases with $n_1 > -1$.

On the other hand, since the existence of losses in metallic metamaterials (LHM)

is unavoidable, we must take into account the imaginary part of n in the imaging formation process. We have studied these effects and show how this absorption has severe effects that affect the superresolution of an extended object by means of a LHM slab. In this way, we have showed the agreement of the numerical simulations with a previous theory proposed.

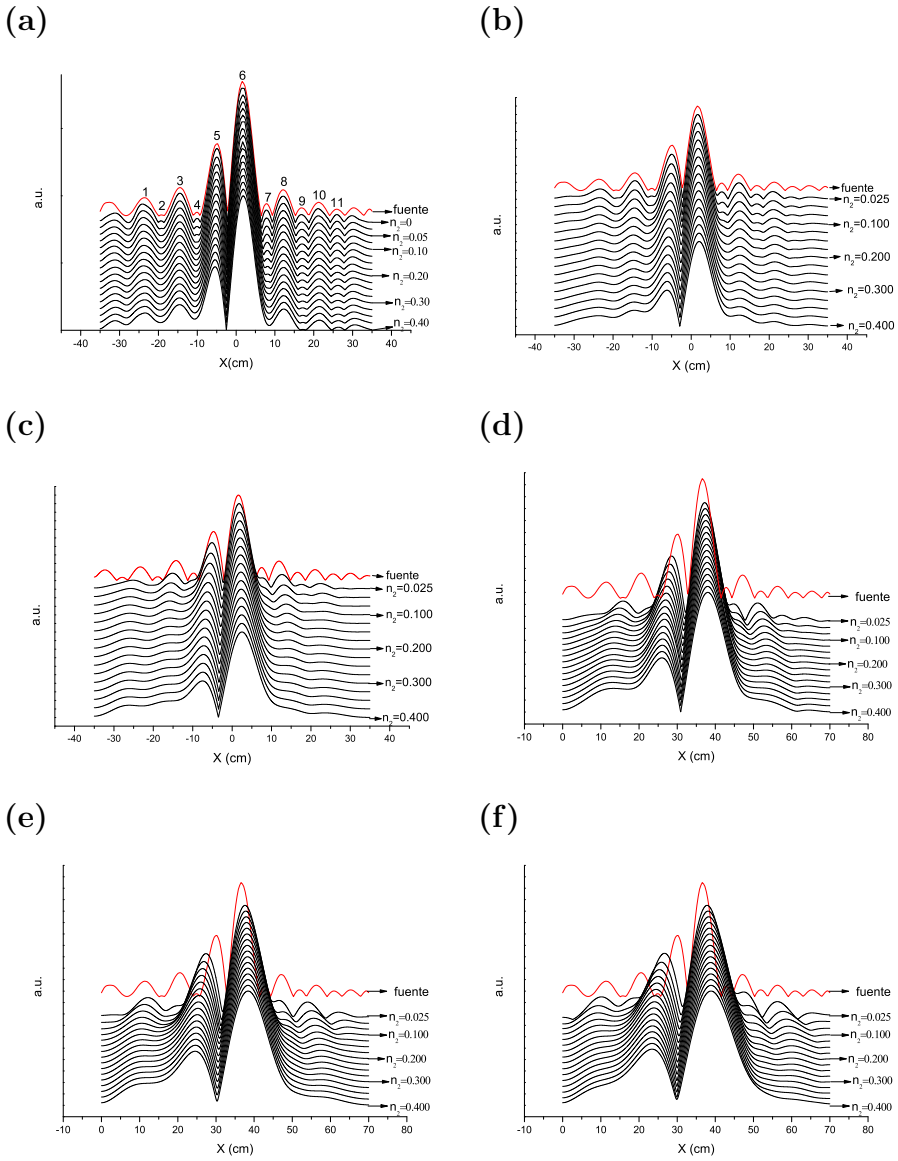

Figure 2.28: Electric modulus of the image of the extended object of Fig. 2.24 by varying the imaginary part n_2 of the refractive index in the cases of (a)$\lambda = 3cm$, (b)$\lambda = 6cm$, (c)$\lambda = 9cm$, (d)$\lambda = 12cm$, (e)$\lambda = 15cm$ and (f)$\lambda = 18cm$

Chapter 3

Photonic crystals with negative refraction

3.1 Motivation

We have shown in previous chapter that the losses are an important obstacle in the imaging properties of metamaterials or LHMs. To avoid this difficulty scientists have tried to use dielectric photonic crystals (PhC) to obtain image formation by negative refraction. However, at first sight, there are several differences in these systems. In LHMs the wavelength λ is much higher than the lattice parameter a, i.e. $\lambda >> a$, while in the PhCs the wavelength is of the order of the lattice parameter $\lambda \approx a$, this fact involved that in LHMs the process of negative refraction can be interpreted within an effective medium theory. On the other hand, in PhCs propagation conveys a diffractive process. In this chapter we analyze the process and factors involved in the formation of the image with these photonic structures.

3.2 Introduction: Photonic crystals

A photonic crystal (PhC) is a material composed of periodically arranged dielectric or metallo-dielectric structures (Fig. 3.1). Essentially, in photonic crystals the dielectric constant ϵ or the refractive index n are periodic, i.e. $n = n(r) = \epsilon^2(r)$. The contrast $n(r_1)/n(r_2)$ between the high and low refractive index is in general higher than 2.

This periodicity affects the propagation of electromagnetic waves (EM) in the same way as the periodic potential in a semiconductor crystal affects the electron motion by creating allowed and forbidden electronic energy bands.

In solid state physics we have a crystalline lattice of atoms which make the potential periodicity for electrons. The state of the electron in the crystal is described

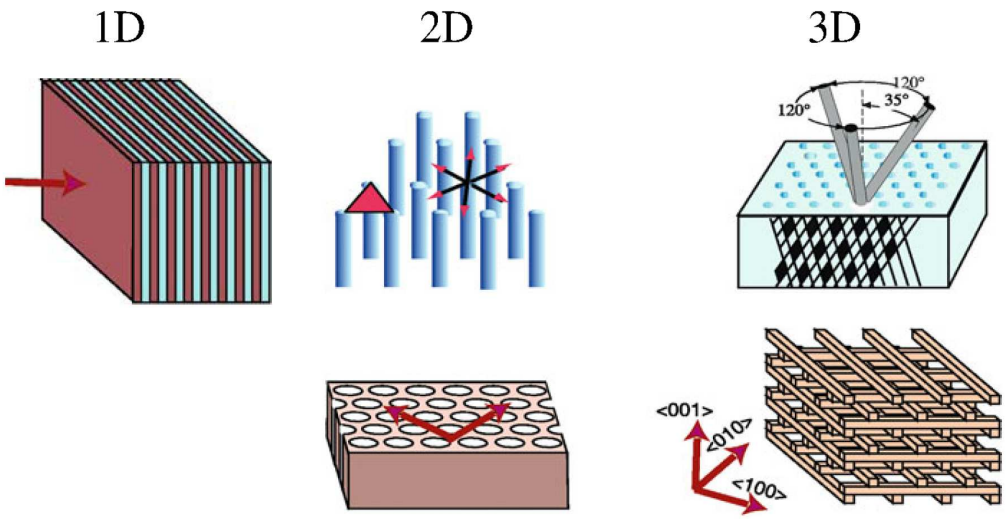

Figure 3.1: Emblematic photonic crystals. From left to right: One-dimensional structure: Bragg mirror. Two-dimensional structures: hexagonal lattices formed by rods or holes. Three-dimensional structures: 'yablonovite' and 'woodpile' structures.

by the Schröndinger equation:

$$i\hbar\frac{\partial}{\partial t}\psi = \left[-\frac{\hbar^2}{2m}\nabla^2 + V(\vec{r})\right]\psi. \tag{3.1}$$

The first term on the right side is the kinetic energy, the second term is the potential provided by the periodic array of atoms, such that

$$V(\vec{r}+\vec{l}) = V(r) \tag{3.2}$$

Where $\vec{l}$ is any lattice vector. the time-dependent equation (3.1) can be transformed into the stationary equation

$$\left[-\frac{\hbar^2}{2m}\nabla^2 + V(\vec{r})\right]\psi(\vec{r}) = \mathcal{E}\psi(\vec{r}) \tag{3.3}$$

While photons satisfy Maxwell's equations that for the electric field lead to the wave equation:

$$\nabla\times\nabla\times E(\vec{r},t) = \frac{1}{\epsilon_0 c^2}\frac{\partial}{\partial t^2}\left[P(\vec{r},t) + \epsilon_0 E(\vec{r},t)\right] \tag{3.4}$$

This equation (3.4) could be modified to reach the structure of a time-independent equation or Helmholtz equation. In 2−dimensional systems with a linear polarization either TE or TM, we can disregard the divergence of the electric field:

$$\nabla^2 E_0(\vec{r}) = -\frac{\epsilon(\vec{r})\omega^2}{c^2} E_0(r) \tag{3.5}$$

We can write the solution of these equations (3.1) and(3.4) for electrons or photons with periodic potential or permittivity respectively, in the form

$$\psi_k(\vec{r}) = u_k(\vec{r}) e^{i\vec{k}\cdot\vec{l}} \tag{3.6}$$

$$E(\vec{r}) = u_k(\vec{r}) e^{i\vec{k}\cdot\vec{l}} \tag{3.7}$$

from which we can establish the Bloch theorem

$$\psi_k(\vec{r}+\vec{l}) = \psi_k(\vec{r}) e^{i\vec{k}\cdot\vec{l}} \tag{3.8}$$

$$E(\vec{r}+\vec{l}) = E(\vec{r}) e^{i\vec{k}\cdot\vec{l}} \tag{3.9}$$

The physical meaning of the Bloch theorem is that the wavefunctions or electric fields at positions $\vec{r}+\vec{l}$ and $\vec{r}$ are almost the same, except for a phase factor $e^{i\vec{k}\cdot\vec{l}}$.

From this analogy we can conclude that effects similar to those of condensed matter will occur in the refraction of the light in PhC, as for example photonic bandgap, localization, etc.

3.2.1 Bands in photonic crystals

We now analyze Bloch waves in an one-dimensional layered periodical media. For simplicity we are going to consider a situation where there are two kinds of slabs with thickness d_1 and d_2 alternatively arranged with dielectric constant ϵ_1 and ϵ_2 respectively as shown Fig. 3.2(a). We assume that the stacking direction is z, and the $x-y$ plane is infinite and homogeneous. Electromagnetic wave propagation in this system can be treated as a one-dimensional problem, because it is trivial for waves along the x and y directions.

The unit cell is composed of slab 1 and slab 2, so that the lattice spacing is $d = d_1 + d_2$. Then the periodicity of the dielectric constant can be written as:

$$\epsilon(z+d) = \epsilon(z) \tag{3.10}$$

which will lead the solution of to have the Bloch form:

$$E_0(z+d) = E_0(z) e^{ikd} \tag{3.11}$$

where we let $E = eE_0$, being e the unit vector. Further, we write the solutions in slabs 1 and 2 of the *lth* unit cell and slab 1 of the *(l + 1)th* unit cell as follows:

$$E_{0l}^{(1)}(z) = A_l e^{iq_1 z} + B_l e^{-iq_1 z}, \tag{3.12}$$

$$E_{0l}^{(2)}(z) = C_l e^{iq_2 z} + D_l e^{-iq_2 z}, \tag{3.13}$$

$$E_{0l+1}^{(1)}(z) = A_{l+1} e^{iq_1 z} + B_{l+1} e^{-iq_1 z} \tag{3.14}$$

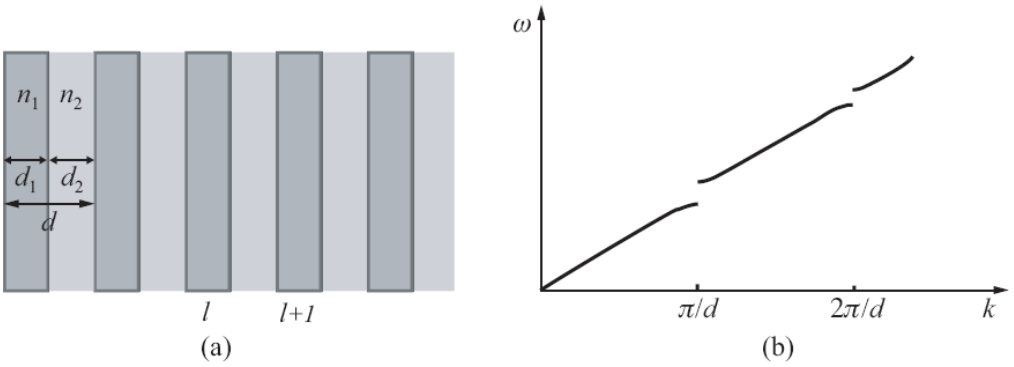

Figure 3.2: (a) Layered periodic medium composed with two kinds of slabs with thicknesses d1 and d2; (b) The dispersion relation for a one-dimensional periodic dielectric structure.

where we define $q_1 = \sqrt{\epsilon_1}\omega/c = n_1\omega/c$, $q_2 = \sqrt{\epsilon_2}\omega/c = n_2\omega/c$, with n_1 and n_2 the indices of refraction. A_l, B_l, C_l and D_l are the oscillation amplitudes of the electric field. For convenience, we take the interface at the left side of each slab as its local coordinate origin $z = 0$, then using the continuity conditions of E_0 and dE_0/dz at boundaries, we can find that

$$\begin{pmatrix} A_{l+1} \\ B_{l+1} \end{pmatrix} = \mathbf{T} \begin{pmatrix} A_l \\ B_l \end{pmatrix} \tag{3.15}$$

where $\mathbf{T}$ is a unimodular 2×2 transfer matrix with elements

$$T_{11} = e^{iq_1d_1}\left[cos(q_2d_2) + \frac{i}{2}\left(\frac{n1}{n2} + \frac{n2}{n1}\right) sin(q_2d_2)\right] \tag{3.16}$$

$$T_{12} = e^{iq_1d_1}\frac{i}{2}\left(\frac{n1}{n2} - \frac{n2}{n1}\right) sin(q_2d_2) \tag{3.17}$$

$$T_{21} = T_{12}^* \tag{3.18}$$

$$T_{22} = T_{11}^* \tag{3.19}$$

Thus the Bloch's theorem is transformed into

$$\begin{pmatrix} A_{l+1} \\ B_{l+1} \end{pmatrix} = e^{ikd} \begin{pmatrix} A_l \\ B_l \end{pmatrix} \tag{3.20}$$

Substituting this into (3.15), we have

$$(\mathbf{T^{-1}} - e^{-ikd}\mathcal{I}) \begin{pmatrix} A_l \\ B_l \end{pmatrix} = 0. \tag{3.21}$$

where $\mathcal{I}$ is the unit matrix. If we consider the reverse process to get A_{l-1},B_{l-1} from A_l,B_l, we can obtain

$$(\mathbf{T} - e^{ikd}\mathcal{I}) = \begin{pmatrix} A_l \\ B_l \end{pmatrix} \tag{3.22}$$

Combining these two expressions, we obtain

$$\cos kd = \frac{1}{2}(\mathbf{T} + \mathbf{T}^{-1}) = \frac{1}{2}Tr\mathbf{T}. \tag{3.23}$$

Finally, we have the transcendental equation

$$\cos k(d_1 + d_2) = \cos\frac{n_1\omega d_1}{c}\cos\frac{n_2\omega d_2}{c} - \frac{1}{2}\left(\frac{n_1}{n_2} + \frac{n_2}{n_1}\right)\sin\frac{n_1\omega d_1}{c}\sin\frac{n_2\omega d_2}{c}, \tag{3.24}$$

from which the dispersion relation for electromagnetic wave propagation in the one-dimensional periodic dielectric structure is determined. The numerical result is shown in Fig. 3.2 (b). It is clear that there are pass-bands and stop-bands for certain frequencies ω: The stop bands appear at the boundaries of the Brillouin zones.

3.2.2 The first Brillouin zone

When studying the optical modes of conventional photonic structures such as optical fibers or other waveguides, we have seen that one of the central aims is to determine the dispersion relation $\vec{k} = \vec{k}(\omega)$ connecting the wavevector $\vec{k}$ of a given mode with the frequency ω. If we invert the dispersion relation to obtain $\omega = \omega(\vec{k})$, then we typically find a different solution for every value of the wavevector $\vec{k}$. So for example in an optical fiber, as we increase k without limit, the mode profile becomes ever more tightly bound to the core, and the effective index of the mode asymptotically approaches the core refractive index. For sufficiently large $\vec{k}$, the system will support multiple modes and there are several solutions ω_i for each value of k.

In periodic systems such as photonic crystals, the dispersion curves are markedly different from each other. Our objective is still to find the frequencies $\omega_i(\vec{k})$ of all the modes for a given wavevector k. But it is no longer true that distinct solutions are found for every value of $\vec{k}$. In Fig. 3.2(b) we show a portion of the band structure (dispersion relation) for the TM modes of a one-dimensional square lattice of period a. As the wavevector $\vec{k}$ varies, the mode frequencies repeat with period $2\pi/d$. In fact, due to Bloch's theorem, any two wavevectors $\vec{k}$ that differ by a reciprocal lattice vector $\vec{G}$ are equivalent.More precisely, for any wavevector $\vec{k}$ and any reciprocal lattice vector $\vec{G}$, we can find a mode j for each mode i such that:

$$\omega_i(\vec{k}) = \omega_j(\vec{k} + \vec{G}) \tag{3.25}$$

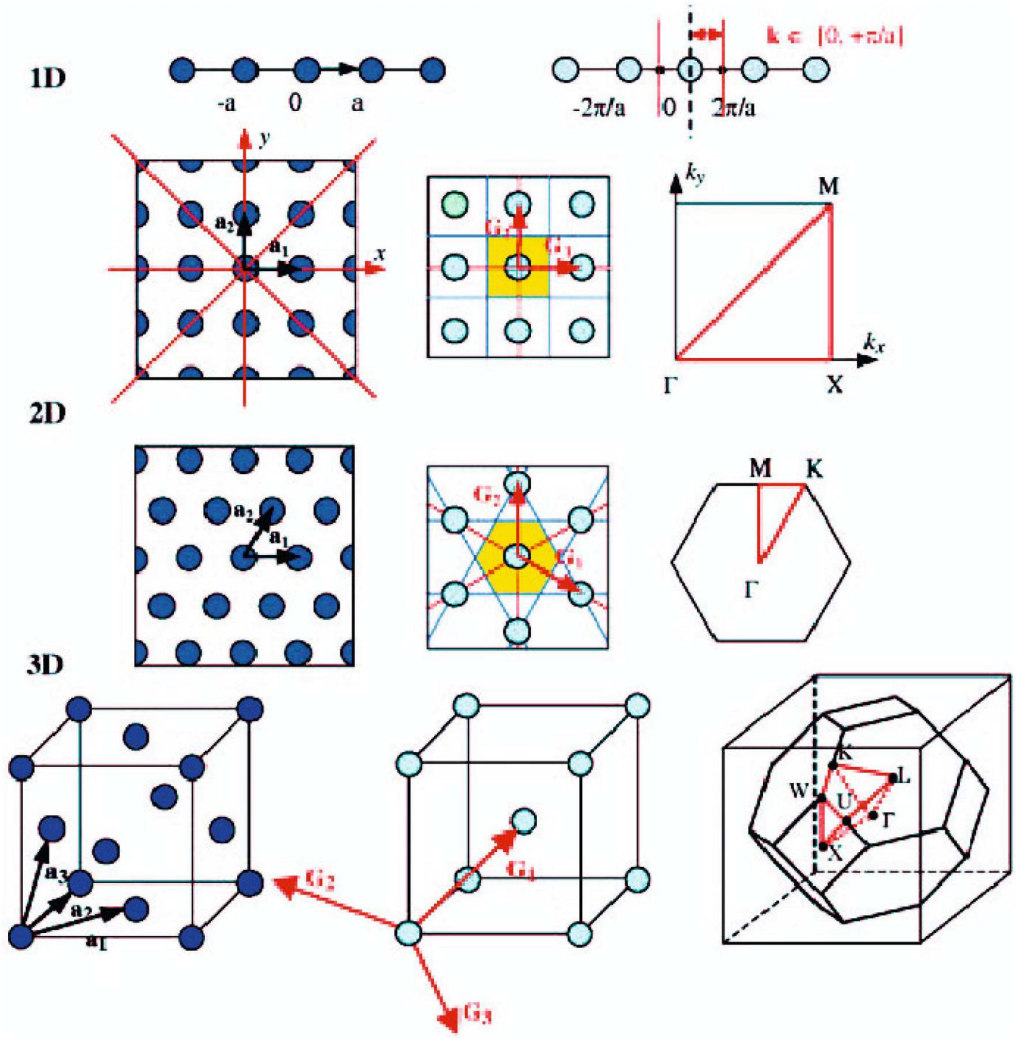

Figure 3.3: One-, two- and three-dimensional photonic crystals (left) with their corresponding Brillouin zones (middle and right). For the one-dimensional crystal, the first Brillouin zone and the irreducible Brillouin zone are formed by the intervals $[-\pi/a, +\pi/a]$ and $[0, \pi/a]$ respectively. For two-dimensional crystals, the middle figures represent the first Brillouin zones (light grey area) while the right figures show the irreducible Brillouin zones (thick lines). For the free crystal, the middle figure represents the centered cubic reciprocal lattice and the right-hand figure represents the two Brillouin zones: the first Brillouin zone is a truncated octahedron, while the irreducible Brillouin zone is the polyhedron with apexes Γ, X, U, L, W and K.

This result simplifies our task enormously, since to find all the modes of the crystal, we only have to solve the problem in the neighborhood of the origin of reciprocal or wavevector space. To make this neighborhood precise, we define the First Brillouin Zone (1BZ) of reciprocal space as that consists of all points closer to the origin than to any other reciprocal lattice vector. Fig. 3.3 shows the 1BZ for a few commonly encountered crystal types. The points labelled with letters in these diagrams correspond to points of high symmetry within the 1BZ.

3.2.3 Band diagrams

For the most common applications of locating and optimizing band gaps, and calculating the dispersion of defect modes, it is only necessary to examine a small subset of points in the 1BZ. Group theory can be used to show that the extremal points of all the bands must occur at points of high symmetry. Thus if a gap is found at the symmetry points, we can be sure that the gap persists at all points within the 1BZ. Each crystal structure is characterized by a set of symmetry points denoted by more or less standard letters. To construct a band diagram, we identify the symmetry points of the 1BZ and connect them by straight lines. The BZ illustrations in Fig. 3.3 show these points and lines. The band structure is calculated along these lines and displayed as a single graph.

3.3 Isofrequency curves

3.3.1 Definition

The refraction processes in photonic crystals are difficult to analyze due to the diffractive and scattering effects which occur inside. The question may arise whether the notion of effective refractive index should be retained and used for the description of these structures. In the long wavelength region, i.e. at low frequencies, the approximation of the crystal as a homogeneous material does not create any particular difficulty. Mathematicians have indeed developed homogenization techniques based on analyzing limiting values. Since, however, most of interesting phenomena, including unusual beam propagation, occur outside the low-frequency limit, we are not satisfied with this homogenization method to understand light propagation in photonic crystals.

Hence, for wavelengths comparable to the period of the structure, the situation becomes more complex. Nevertheless, numerical simulations of the propagation of the field as well as experiments have revealed that under certain conditions a periodic or a quasi-periodic structure may behave like a bulk homogeneous material except for the interfaces of the structure at which scattering effects may always occur. Therefore, we must consider both the phase velocity and, more relevant, the group velocity vector

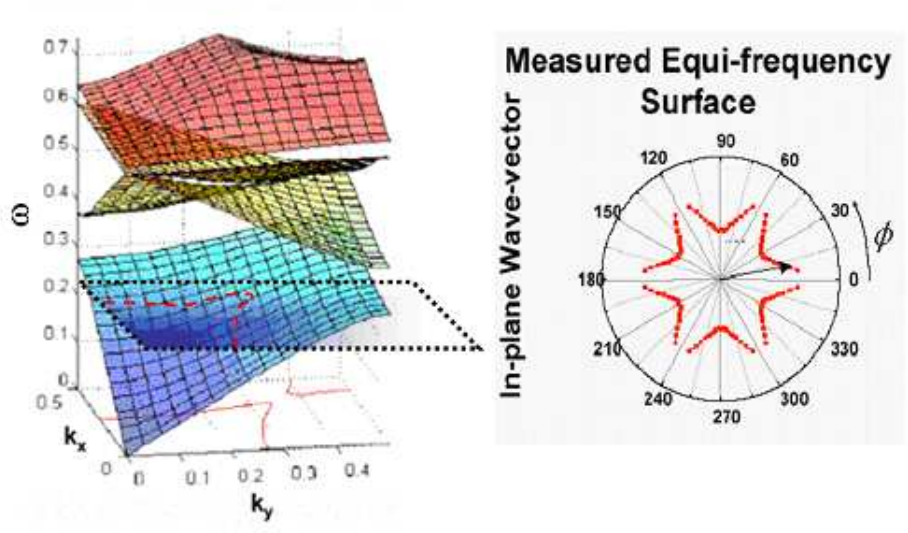

Figure 3.4: Isofrequency bands for a two dimensional photonic crystal. The intersection of the bands with a horizontal plane ω_0 give us the isofrequency curve for that frequency.

to study beam propagation in photonic crystals. We thus need to investigate the equifrequency surface of the photonic band structure.

In the two-dimensional case represented in Fig. 3.4, the isofrequency profiles are obtained by horizontally cutting the dispersion surfaces separately calculated by means of a plane wave model (see Appendix). Such isofrequency curve defines the permitted phase wavevectors inside the photonic crystal at one frequency ω and the group velocity is given by

$$\vec{v_g} = \vec{\nabla}_k \omega(\vec{k}) \tag{3.26}$$

The group velocity is therefore defined by the normal to the isofrequency surface $\omega(\vec{k}) = \omega_0$ at point (k_x, k_y). Note the inverse correlation between curvature and group velocity.

The group velocity $\vec{v_g}$ goes inwards or outwards the isofrequency curve depending on whether the slope of the band is negative or positive. At first sight the effect of negative refraction in PhCs arises due to the negative slope of the upper or second band. This negative slope is the result of the reduction of the first Brillouin zone. In particular in the model of an empty lattice the total phase factor is $e^{i(k-2\pi/dsignk)r}$, i.e., the sign of the wavevector coincides with the slope of the band. The isofrequency surfaces of photonic crystals are actually a direct analogue to Fermi surfaces for solid state crystals.

3.3.2 Calculation of the isofrequency curve

Our purpose is to calculate the isofrequency curve from the known wavevectors of the reduced band diagram given by the plane wave expansion. By using group theory, it can be proved that the isofrequency curves in the reciprocal space have the full point group symmetry of the lattice (extremal points of all the bands must occur at high-symmetry wave vector points). In this way, we can calculate the isofrequency curve, for example for a trigonal or hexagonal photonic crystal, with the reduced band diagram in first approximation. We can assume that the isofrequency has the polynomial form in polar coordinates:

$$\vec{k}(\phi) = a + b\phi + c\phi^2 + d\phi^3 \tag{3.27}$$

where ϕ is the azimuthal coordinate in the reciprocal space. So, if we replace in Eq. (3.27) the values of the modulus $|\vec{k}_{\Gamma M}|$ and $|\vec{k}_{\Gamma K}|$ and their derivatives at the directions of high symmetry $\phi = \phi_0 = 0$ and $\phi = \phi_1 = \frac{\pi}{6}$ respectively:

$$\vec{k}(\phi_0) = \vec{k}_{\Gamma M} \tag{3.28}$$

$$\vec{k}\,(\phi_1) = \vec{k}_{\Gamma K} \tag{3.29}$$

$$\left.\frac{\partial f}{\partial \phi}\right|_{\phi=\phi_i} = 0 \tag{3.30}$$

on combining Eq. (3.28), Eq. (3.29) and Eq. (3.30) it results:

$$\vec{k}(\phi) = \vec{k}_{\Gamma M} + \frac{3(\vec{k}_{\Gamma K} - \vec{k}_{\Gamma M})}{\phi_1^2}\phi^2 + \frac{2(\vec{k}_{\Gamma M} - \vec{k}_{\Gamma K})}{\phi_1^3}\phi^3. \tag{3.31}$$

The other parts for completing the isofrequency curve are calculated by means of group-symmetry operations.

We deduce from Eq(3.31) that for $\vec{k}_{\Gamma M} = \vec{k}_{\Gamma K}$ the isofrequency is a circumference, i.e. the medium can be considered isotropic. And the difference between the wavevector along the two directions ΓK and ΓM gives us the separation of the isofrequency from the isotropic medium.

3.3.3 Refracted waves in photonic crystals

Isotropic dielectric materials obey the Snell law $n_1 sin\theta_1 = n_2 sin\theta_2$ for refracted waves.

The phenomenon of refraction undergoes dramatic modifications as soon as one of the media on either side of the interface is anisotropic. While two and three-dimensional photonic crystals are by construction anisotropic, a number of solid

state crystals that are both transparent and anisotropic, exist in nature. The optical anisotropy of these crystals manifests itself in the form of birefringence, which merely expresses the dependence of the refractive index on the direction of propagation and on the polarization of light. The fundamental principles of optics of anisotropic crystals were established by A. Fresnel in 1820, long before the development of the electromagnetic theory. The reader will find a more detailed introduction to the optical properties of anisotropic crystals in the reference works (Born 1965; Landau 1969). Generally, the angular dependence of the phase refractive index in such solid state crystals can be described by an index ellipsoid, which allows an analytical formulation for the refraction of light in birefringent crystals. Compared to solid state crystals, photonic crystals present dispersion curves of a much more complex shape, as can be seen in Fig. 3.4(b). The spatial profiles of the index $n(k_x, k_y, k_z)$ at a given frequency in the reciprocal space, or in other terms, the isofrequency curves or surfaces [70] are therefore very far from being ellipsoidal. Therefore, in photonic crystals we can consider the Snell's law taking the form

$$\frac{\sin\theta_1}{\sin\theta_2} = n_{PhC}(\theta_1) \tag{3.32}$$

where the refraction index of the photonic crystal n_{PhC} is a function of the incidence angle θ_1.

The refracted waves can be found on the dispersion contours (or equifrequency dispersion contours) by conserving the surface-parallel component of the wavevector from the incident wave(Fig. 3.5). Geometrically, the refracted waves are obtained from the points on the free-space contour, representing the incident wave, by drawing a line perpendicular to the interface and finding its intersections with the material dispersion contour. Moreover, the presence of strong scattering crystal structures can modify the dispersion relation of light so much that the shapes of the dispersion contours are far from being circular. The gradient directions on these contours and thus the refraction directions can be very different from those expected in a uniform material. Furthermore, the strength of each refraction wave can be quite different from either refraction in uniform media or simple diffractions. In the extreme case, the occurrence of a photonic band gaps can entirely eliminate waves on certain directions. These considerations illustrate that photonic crystal structures can give rise to nontrivial effects in refraction, and we will refer them as complex Bragg scattering. The refraction process then may be analyzed by matching the wavevectors inside the bulk crystal to that of the incident wave and also reducing the solution wavevectors to the first Brillouin zone to find the refracted Bloch modes.

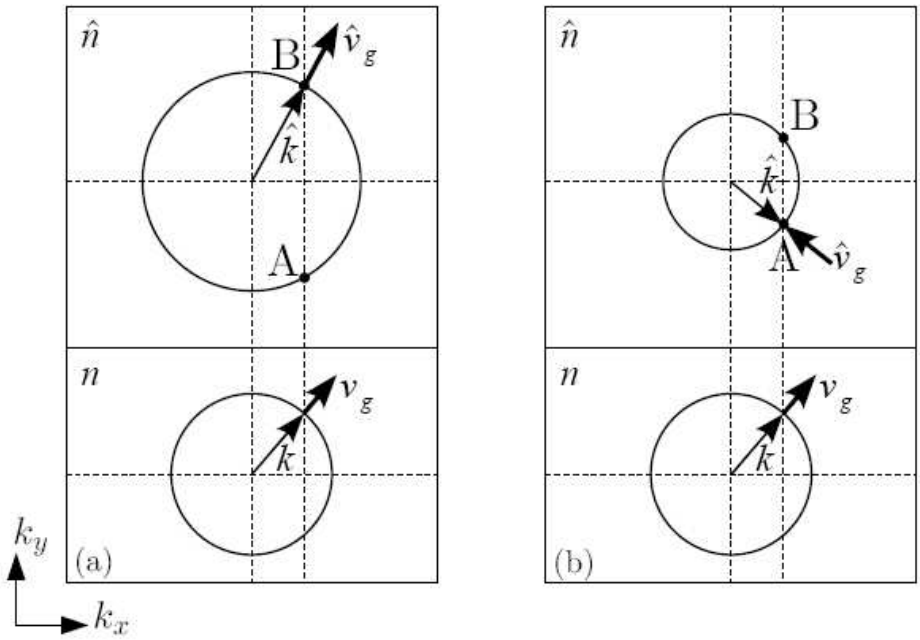

Figure 3.5: Wave vector diagram for a light incident problem from air ($n = 1$) to a homogeneous isotropic dielectric material with refractive index $\hat{n} > 1$ (a) and from air ($n = 1$) to a photonic crystal with effective $\hat{n} < 0$ (b). $\vec{k}$ and $\hat{\vec{k}}$ denote the incident and refracted wave vector, respectively; v_g and $\hat{v}_g$ denote the corresponding group velocity vectors.

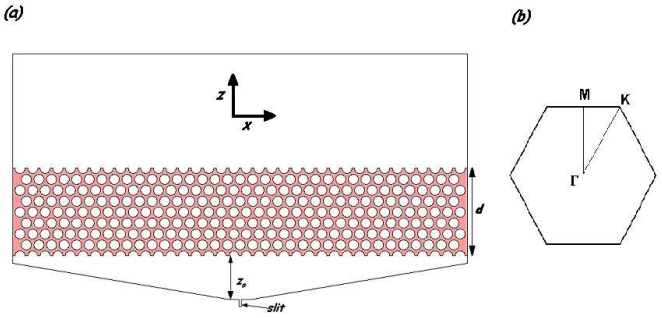

Figure 3.6: (a) Geometry of the numerical simulation for the PhC slab of air cylinders in a dielectric matrix with $\epsilon = 12.96$. The wave source is at distance z_0 from the slab limiting interface. (b) Brillouin zone for the hexagonal PhC and symmetry points.

3.4 Propagation of extended wavefronts in photonic crystal slabs

The theory of negative refraction in photonic crystals is outlined in the next example. We first address a 2-D hexagonal lattice of air cylinders in a dielectric matrix with permittivity $\epsilon = 12.96$, lattice constant a and radius $r = 0.4a$. The geometry is shown in Figs. 3.6(a) and 3.6(b) both for a slab of this crystal and its Brillouin zone. This structure was proposed in [71] and its band diagram is shown in Fig. 3.7(a). From it, one obtains isofrequency lines that, at the frequency at work, are circle-like centered in the Γ point (Fig. 3.7(b) (top inset)). In Fig. 3.7(b) we show the different permitted wavevectors k in this regime of frequencies, which are in the second band, for the directions ΓK and ΓM. We observe that the the magnitude of the permitted wavevectors is different for the ΓK and ΓM directions in this range of frequencies (bottom inset of Fig. 3.7 (b)), and therefore the effective refractive index is not the same for both directions, which causes the deformation of the isofrequency from a circle one; this deformation being the cause of an aberration in the imaging process by a slab of this crystal, as shown next. We shall denote as the *input plane* that at which we specify the limiting value of the wavefield illuminating a slab of thickness d of this array. This plane is taken at distance z_0 from the entrance surface of the crystal slab. Let us now consider a point source, in the input plane, at distance $z_0 = 3.442a$, which emits linearly polarized harmonic waves around a normalized frequency $\omega = 0.305 \times 2\pi c/a$, λ being the wavelength, with the electric vector E_y parallel to the cylinder axis.

This source is realized with a narrow slit whose exit is at $z_0 = 3.442a$. The thickness of the PhC slab is $d = 2z_0$. The calculation gives the distribution of the

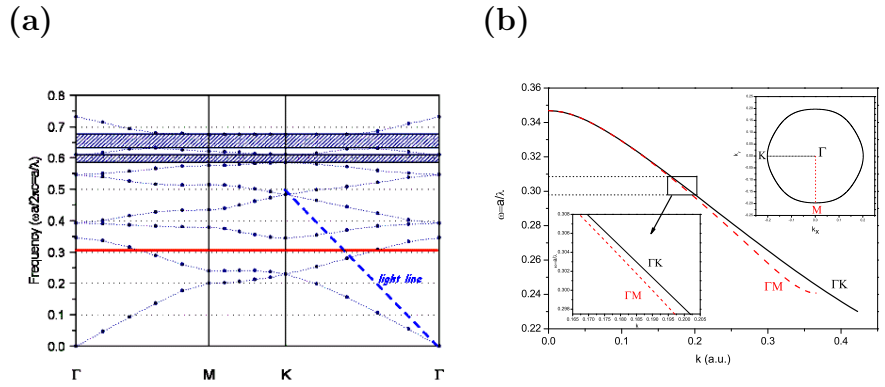

Figure 3.7: (a)Band diagram, obtained using a plane wave expansion calculation, for the hexagonal lattice of air cylinders in a dielectric matrix with $\epsilon = 12.96$. The red line corresponding to the range of frequencies used, cuts the second band in such a way that there is a circle-like isofrequency about the Γ point. The corresponding frequency surface gradient is negative and so is the group velocity. The light line (broken) is also shown. (b) Second band for ΓK (solid line) and ΓM (dashed line) directions, showing the differences, at used frequencies, of wavevector distances from the Γ point to the K and M points, (bottom inset), as well as the corresponding deformation of the corresponding isofrequency from a circle, (top inset) for $\lambda = 3.36a$.

field propagated throughout the crystal and out of it. In particular, its response in the image plane at the Veselago distance z_0 from the exit surface is evaluated. This is shown for $\lambda = 3.28a$ in Fig. 3.8.

3.4.1 Isoplanatic condition and transfer function

It is well known that any imaging system, and in particular a lens, should be space invariant, at least in a certain field region. This involves the *isoplanatic* condition Eq. (2.16) . We calculate the transfer function, by means the procedure explained before (chapter 2, section 2.6), in order to test the degree of isoplanatism of this PhC slab.

Fig. 3.9 shows the transfer function obtained by this procedure for the wavelengths: $\lambda = 3.24a$, $3.28a$, $3.32a$ and $3.36a$. On the other hand, Fig. 3.10 depicts the transfer function at different distances z_0 of the source from the slab. We observe that the widths of these transfer functions do not exceed the Rayleigh limit of resolution $1/\lambda$.

Subsequently, an inverse Fourier transform of this product should yield a field distribution $i(x)$ in the image plane according to Eq. (2.16), and this result ought to be very similar to that obtained by direct FE calculation of the propagation of this extended object wavefront through the crystal slab, in the image plane. The

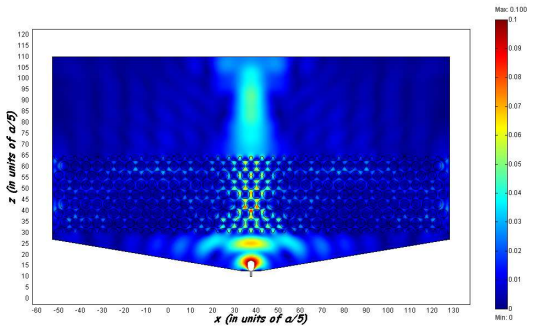

Figure 3.8: Map of the modulus of the electric field E_y for a narrow slit which acts like point source (down) with a $\lambda = 3.28a$ in front of a 2-D hexagonal photonic crystal. We observe a focus both inside and out the crystal. The outer focus is elongated as a consequence of aberrations. (White spots in the color distribution indicate that the value is out of the color scale on the right).

comparison of the images of an extended object that has no subwavelength details, obtained by the above mentioned procedures is displayed in Fig. 3.11 for $\lambda = 3.28a$ measured at a distance z_0 from the slab. They indicate that in the range of wavelengths and distances of operation studied here, there is good degree of isoplanatism in the crystal, however due to a diffraction effects and since the isofrequency lines are not perfect circles, the image possesses aberrations.

3.4.2 Aberrations

These aberrations have been characterized by means of a ray tracing (see Figs. 3.12(a)-(d)). In order to understand the different mechanisms that alter the imaging process, we think that it is useful to separate the aberration due to only the deformation of the isofrequencies from circles (Fig. 3.12(a)), (where the exterior medium plays no role), from the actual one that takes place in the real system subjected to the FE simulation, namely, that in which one also takes into account the difference between the refractive index of the surrounding air and the effective refractive index of the PhC slab. This additional cause of aberration is produced by the size difference between the isofrequency lines in the exterior and in the crystal. The lateral (Δx) and longitudinal (Δy) aberration distances, defining the vertices of the resulting ray tracing caustic, (cf. Figs. 3.12(a) and 3.12(b)), are shown in Fig. 3.12(d). The distances Δx and Δy of the aberration due only to deformations of the isofrequency from a circle, increase with the wavelength, (this is clear by looking at the bottom inset of Fig. 3.7(b), where details of the separation between the ΓK and ΓM curves are appreciated). On the other hand, the distances Δx and Δy of the aberration in the real case, namely that in which we have also had into account that the refractive index of the surrounding air, being different to that of the PhC, gives rise to

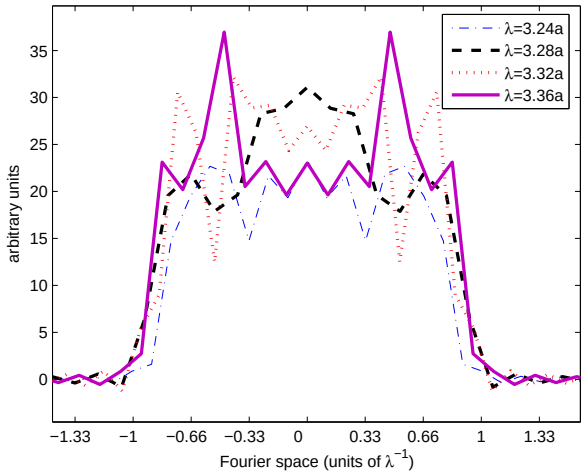

Figure 3.9: Modulus of the real part of the transfer function (i.e. Fourier transform of the image of a point source) produced by a hexagonal PhC of air holes in a dielectric matrix with permittivity $\epsilon = 12.96$, lattice constant a and radius $r = 0.4a$, at different wavelengths. We observe that their widths do not exceed the Rayleigh limit of resolution $1/\lambda$.

transmission into the PhC that varies with the angle of incidence, decrease with the wavelength.

It should be noted that there is yet a third cause of aberration provoked by the transmission dependence on the angle of incidence due to the surface impedance $Z = \sqrt{\epsilon/\mu}$, which has been demonstrated to be different from $Z = 1$ in these PhC slabs [72]; this is known to alter the the position of the focus, within an effective medium theory [69].

3.5 Conditions for superresolution

Based on the previous discussion for LHMs,in this section we analyze the conditions for superresolution in a photonic crystal. First, it is convenient to begin with an easy model, that is frequently on use, illustrating the amplification of evanescent waves and superlensing, namely, both in a LHM and a silver lens (SL). This will provide an example and guidance for the behavior of the PhC slab.

It is illustrative to consider first the constitutive parameters of the LHM slab to be $\epsilon' = \mu' = n' = -1$. These values are not strictly physical, since some absorption should be present [16], however they help to interpret the behavior of the evanescent waves which grow with the slab depth.

Let $\mathbf{k} = (k_x, k_z)$ and $\mathbf{k}' = (k'_x, k'_z)$ be the wavevectors of one evanescent plane wave

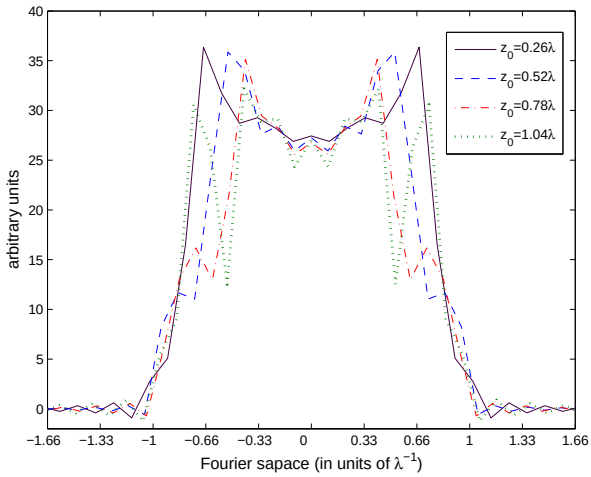

Figure 3.10: Modulus of the real part of the transfer function (Fourier transform of the image of a point source) produced by a hexagonal PhC of air holes in a dielectric matrix with permittivity $\epsilon = 12.96$ for $\lambda = 3.32a$, at different distances z_0 and different thickness $d = 2z_0$ of the source from the slab. Their widths do not exceed those of the Rayleigh limit of resolution $1/\lambda$, although the source is in near field.

component, incident and transmitted into the slab, respectively. Namely, $ae^{ik_x x - k_z z}$ is refracted in the first interface of the LHM slab into $ae^{ik'_x - k'_z z}$, where

$$k_z = \sqrt{k_x^2 - k_0^2}, \tag{3.33}$$

$$k'_z = \sqrt{k_x'^2 - k_0^2 n'^2}, \tag{3.34}$$

Let s and s' be the directional sines of $\mathbf{k}$ and $\mathbf{k}'$ for k_x and k'_x, respectively , namely, $k_x = k_0 s$, $k'_x = k_0 n' s$, then the Snell law derived from the continuity equation: $k'_x = k_x$ implies that $s' = -s$ and thus $k'_z = -k_z$ which is usually interpreted as the amplification of the incident evanescent wave component by the LHM slab.

On the other hand, in a silver slab we again assume approximately that : $\epsilon' = -1$, $\mu = 1$ and thus $n' = i$, then the Snell law yields $is' = s$, i.e.: $s'^2 = -s^2$; thus the z-component of the wavevector transmitted into the slab is in this case

$$k'_z = \sqrt{k_x'^2 - k_0^2 n'^2} = k_0 n \sqrt{s'^2 - 1} = \\ k_0 i \sqrt{-s^2 - 1} = -k_0 \sqrt{s^2 + 1}, \tag{3.35}$$

which is an amplified wave, even though with the sign difference: $+$ instead of: $-$ in the square root, namely: $\sqrt{s^2+1}$ instead of $\sqrt{s^2-1}$. In the electrostatic limit,

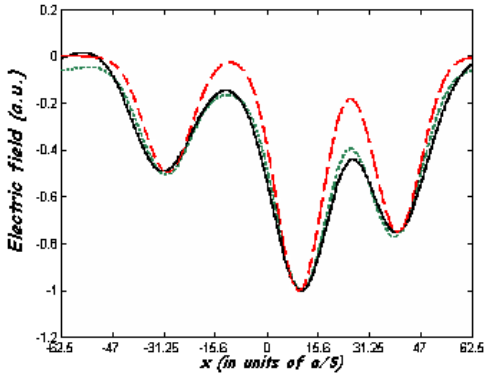

Figure 3.11: Electric field amplitude distribution of an extended object wavefront for $\lambda = 3.28a$ measured at a distance z_0 from the slab (red dashed line); which does not demand superresolution details. Its image obtained from the transfer function via by Fourier transform, as explained in the text, is shown in the green dotted line. The image obtained by propagation FE simulation (black solid line) is very similar to the latter.

however, $s >> 1$ which yields exactly $k'_z = -k_z$. Thus the silver slab acts in a similar way as the LHM slab in this limit which involves scales of the slab thickness, and distances outside it, much smaller than λ.

On the other hand, in a photonic crystal the restrictions to amplify incident evanescent waves are stringent [73]. For example, in Fig. 3.13 we show the evolution of an incident evanescent wave on a slab of the photonic crystal addressed in section This evanescent wave has been created by total internal reflection of a plane wave incident on a dielectric prism, placed below the slab. No amplification is observed. The question however is: under what circumstances can some evanescent components couple to surface waves of the exit interface of the PhC slab?. In other words, can we design a photonic crystal with a band diagram in the evanescent region, that contains evanescent modes being flat enough and involve a large enough number of wavevectors? In this way, there is coupling with a significant number of evanescent components of the incident wavefield, and thus amplify them at a given working frequency.

To search an answer, let us first look at this amplification in either a LHM and a silver slab. To this end, one has to search for the excitation of surface waves, plasmon-polariton-like ones, on the exit surface of the slab, and these waves must couple to as many as possible evanescent components of the wavefront propagated along the slab. This was seen in chapter 2, Fig. 2.20 for a LHM and was further illustrated in Fig. 2.22. where an intensity distribution along the z-direction showed the corresponding increase of the intensity at the slab interfaces as the the source becomes closer to the slab and thus more evanescent components of the incident wave are retrieved. SPP

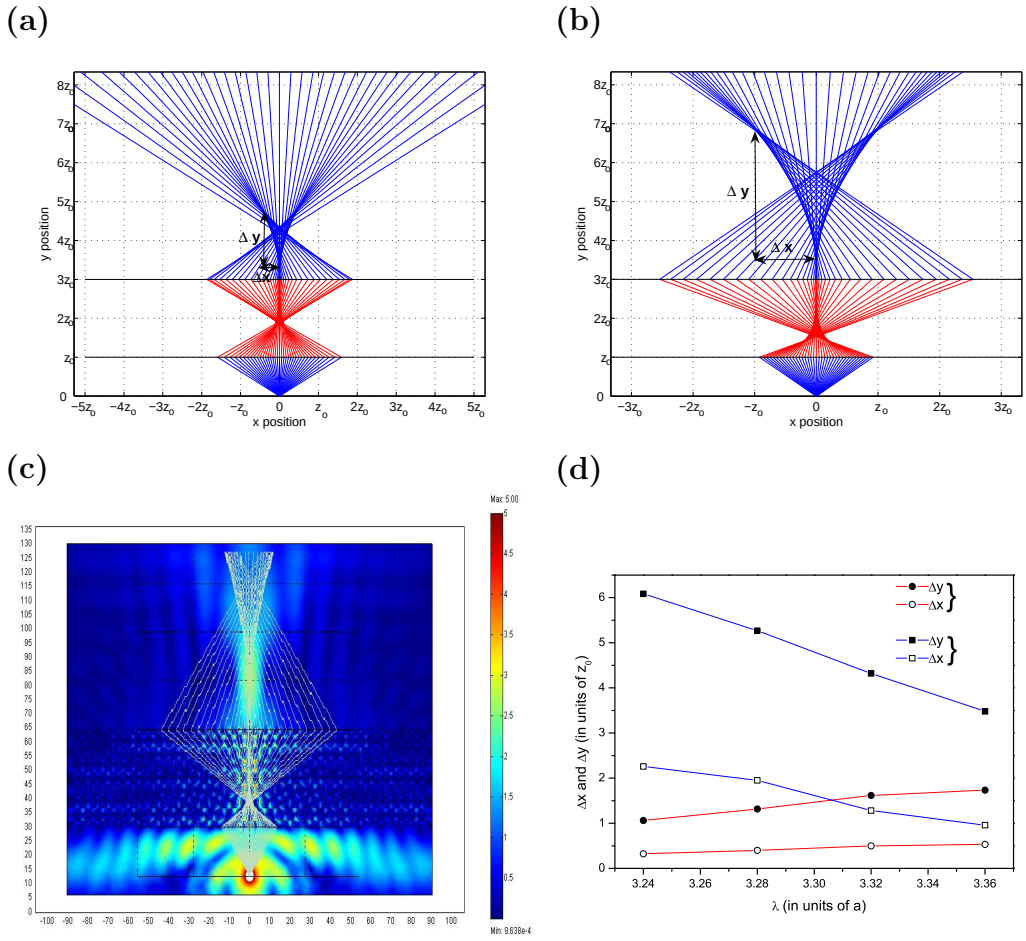

Figure 3.12: Aberrations analyzed by means of a ray tracing for: (a) A PhC illuminated by a point source with $\lambda = 3.32a$, where we have considered only the aberration due to the deformation of the isofrequency from a circle one, (namely, the surrounding medium has a refractive index that equals the averaged effective one of the crystal slab). (b) The same illuminated PhC where we have also taken into account that the surrounding medium is air. This is the real situation of the FE simulation. We consider both the aberration caused by deformation in the isofrequency from a circle and that caused by difference between effective refractive index of the PhC and the surrounding medium (air) ($\lambda = 3.36a$). (c) Same as (b) with the numeric simulation and $\lambda = 3.32a$; we observe agreement between ray tracing and FE simulation. This agreement is clear both in the position and depth of the focus obtained by both methods. (d) Distances Δx (white symbols) and Δy (black symbols) corresponding to the lateral and longitudinal aberration, respectively, for the case in which the configuration is that of Fig. (a)(circles and red line) and for the case in which is that of Fig. (b) (squares and blue line). These distances are referred to the caustic vertex in the paraxial focus.

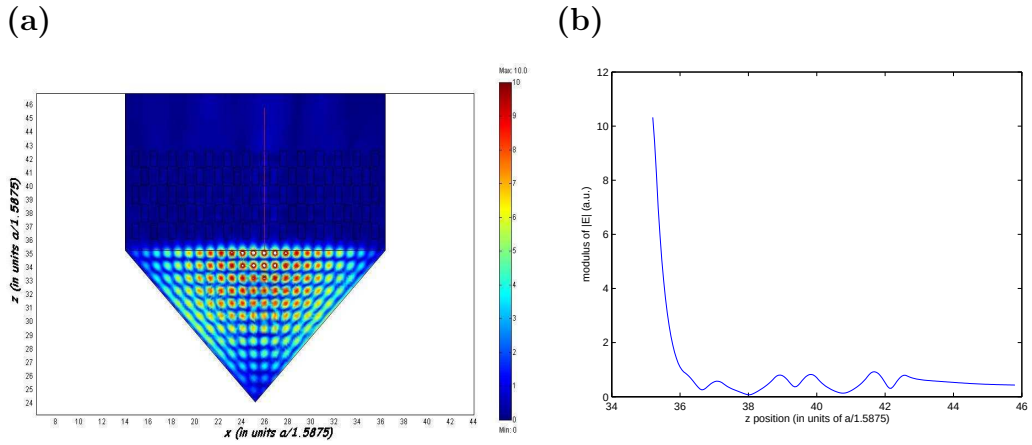

Figure 3.13: (a) Total internal reflection at 45 degrees in a dielectric prism with n=3.5 below the photonic crystal slab. An evanescent wave is transmitted and incides on the crystal (b) Variation of the evanescent wave intensity along the depth (z-coordinate) of the crystal.

in LHM exist for both TE and TM waves [15]. On the other hand, in a silver slab the Drude model gives the permittivity:

$$\epsilon(\omega) = 1 - \frac{\omega_p^2}{\omega\left(\omega + i/\tau\right)} \underset{\omega\tau<<1}{\approx} 1 - \frac{\omega_p^2}{\omega^2}, \tag{3.36}$$

ω_p being the plasma frequency in the bulk. If we look into the dispersion relation:

$$k_x(\omega) = \frac{\omega}{c}\sqrt{\frac{\epsilon(\omega)}{\epsilon(\omega)+1}}. \tag{3.37}$$

When the real part of the permittivity is $\epsilon \approx -1$ then from Eq. (3.37) one sees that the surface plasmon satisfies that $k_x(\omega) \to \infty$, this is the essence of the electrostatic limit: $k_x(\omega) >> k_0$ at subwavelength scales, and thus from Eq. (3.36) we have that its excitation frequency ω_{sp} is:

$$\omega_{sp} = \frac{\omega_p}{\sqrt{2}} \tag{3.38}$$

Fig. 2.20 shows the importance of the evanescent components in the electrostatic limit, namely when the source is at a distance from the slab much smaller than the wavelength, then the contribution of the propagating components is not so important and, as a result, no focus inside the slab, as dictated by Veselago's geometry, is formed.

In order that each evanescent component of the incident wavefront couples with a surface wave of the exit interface of the slab, namely, it should follow the hyperbolic

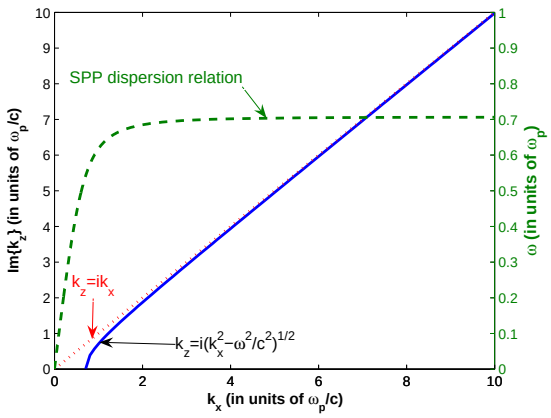

Figure 3.14: Condition for superresolution of a superlens with real part of the permittivity $\epsilon \approx -1$ at a working frequency $\omega_p/\sqrt{2}$, ω_p being the plasma frequency. Due to the fact that excited surface plasmons (green dashed line) have high value of the wavevector k_x, the hyperbolic condition Eq. (3.39) in the evanescent zone (blue solid line) is satisfied for the wavevector k_x of all evanescent components of the incident wavefront, since for high k_x this condition becomes the asymptotic straight line $k_z = ik_x$ (red dotted line) which corresponds to the flat zone of the dispersion relation (green dashed line).

isofrequency line of the (k_x, k_z)-complex plane in the evanescent zone, given by:

$$k_z = i\sqrt{k_x - \epsilon(\omega)\frac{\omega^2}{c^2}} \tag{3.39}$$

If we refer to Fig. 3.14, one sees that Eq. (3.39) would impose that each evanescent component of the slab follows that isofrequency line at the same plasmon frequency ω_{sp}. However, The SPP plasmon dispersion relation shown in Fig. 3.14 shows that this is only possible in the flat region of this curve which corresponds to large values of k_x at which Eq. (3.39) takes on the asymptotic form given by the straight line:

$$k_z = ik_x \tag{3.40}$$

This is the reason why the silver slab works yielding superfocusing at such small distances in the electrostatic limit: all evanescent components at the same frequency excite the corresponding value k_x in the flat zone of the dispersion relation, all of them satisfying it at the plasmon frequency ω_{sp}.This could not happen, however, in the curved portion of the dispersion relation, since there only one k_x corresponds to each ω_{sp}, and thus only one evanescent component of the incident wavefront would excite it.

Now, turning back to a PhC slab, we can create surfaces modes by introducing a cut in the last row elements, namely those forming the exit surface of the slab. In this

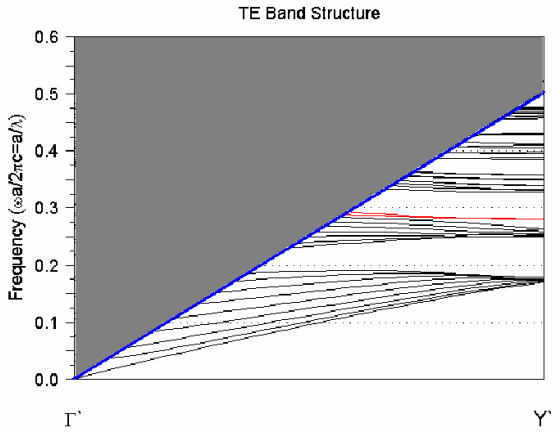

Figure 3.15: Surface mode dispersion curve (red line) in the second band for TE polarization (Electric field parallel to the prisms). The surface mode is "flat", which implies that all those k_x wavevectors at the the right of the light line included in the definition domain of this red segment are permitted in the surface at practically the same frequency of excitation.

work we present a hexagonal array of rectangular prisms $0.4a \times 0.8a$ with permittivity $\epsilon = 9.61$ in air, like those used in reference [74]. We have excited a surface mode by cutting $0.1a$ the first and last rows of prisms, and we have calculated it by the supercell method [75, 76, 77] in Fig. 3.15. However, this mode does not conveys superresolution because the wavevectors k_x are very close to the light cone ω/c and thus they are not sufficiently high to reach the hyperbolic isofrequency curve posed in our Eq. (3.39) in the evanescent zone, or conversely the corresponding dispersion relation line, (green curve in Fig. 3.14). Furthermore, we have a limited spectrum of permitted k_x, with a maximum k_M that does not allow this subwavelength detail.

Finally, in order to show and illustrate that the excitation of surface modes itself, is not enough to imaging with superresolution, unless they fulfill the requirements discussed in the above analysis for left handed materials and silver slabs, we show in Fig. 3.16 the image obtained from an extended object in a slab of this crystal, either with or without introducing the aforementioned cut in the first and last rows. In other words, either with or without the existence of surface modes. One observes that the creation of this surface mode is not enough, and hence it does not yield any improvement in the quality of the subwavelength detail of such an image of this extended object that demands superresolution. This lack of superresolution is due to the fact that the length $\frac{\pi}{a} - \frac{\omega}{c}$ of the range of values of the transversal wavevector of the surface waves is only $0.788\frac{\omega}{c}$, (cf. Fig. 3.15); and hence, if one looks to the dispersion curve $\omega(k_x)$ of Fig. 3.14, one sees that this range lies inside the zone in which the hyperbola of Eq. (3.39) does not take the asymptotic form Eq. (3.40); namely, that range lies in the curved region of the plasmon dispersion relation which

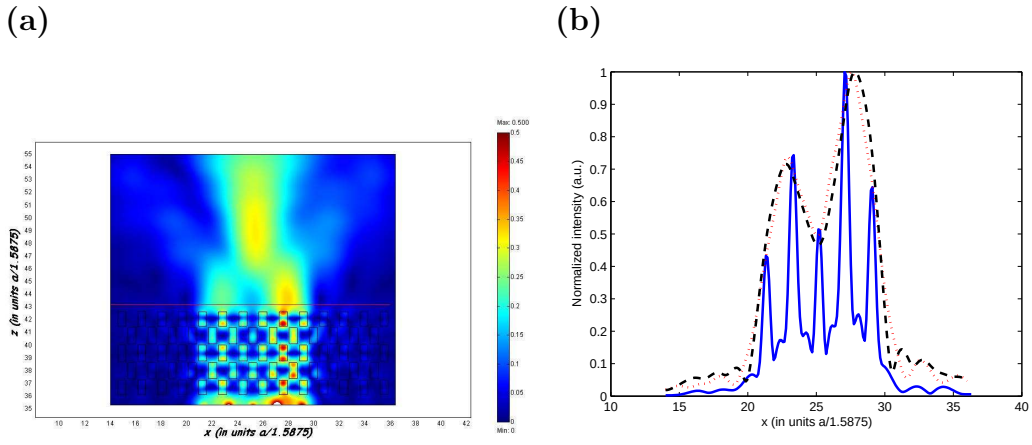

Figure 3.16: (a) Map of the modulus of an extended object wavefront in the bottom impinging on a photonic crystal (b) Corresponding intensity of extended object wavefront (blue solid line) and its image by a crystal whose exit interface is cut such that a surface mode is either not excited (red dotted line) or excited (black dashed line) at the frequency $\omega = 0.345 \times 2\pi c/a$ (i.e.$\lambda = 2.898a$).

is between the light line (value ω/c) and the flat zone region $\omega = constant$ of the dispersion curve. Therefore, the excited surface waves do not follow the required isofrequency line in the evanescent zone.

3.6 Conclusions

We have studied the propagation of extended object wavefronts in some photonic crystal slabs capable of yielding negative refraction. We have found by means of an analysis that introduces the transfer function, that this system is isoplanatic, at least in a wide range of distances of the source and frequencies as those addressed here. However, due to imperfections in the isofrequencies of their band diagram, and to angle dependent transmissions at their interfaces, they present aberrations that we have characterized. We have compared this photonic crystal behavior with that of a left handed material and we have shown the differences in the transfer functions of both as regards the resolution of images. Finally, we have discussed the necessary conditions to achieving superresolved images by PhC slabs by taking guidance of the equivalent problem for both left handed materials and silver slabs . We have concluded that the created surface waves in the exit interface of a PhC should have a wavevector that either follows the correct hyperbolic isofrequency line in the complex plane of its Cartesian components, or the experimental conditions should be such that the electrostatic limit, where a flat dispersion relation is held for enough values of the transverse wavevector, applies.

Chapter 4

Self-collimating in photonic crystals

4.1 Motivation

We have shown in chapter 3 that the condition for superresolution in dielectric photonic crystals cannot be reached. However several works have claimed superresolution in these systems, some errors which have been committed by initial works in negative refraction in PhC have been slightly remarked in the previous chapter and now they will be more extensive developed. Finally, we investigate the phenomenon of self-collimation in photonic crystals that constitute one of these mistakes proposing devices and showing experiments in the GHz range. We put forward theory and numerical simulations. Also an experiment that matches with these results is shown.

4.2 Introduction: Focussing by a square lattice?

Some of the first works on negative refraction in PhC [78, 79] had several errors. We have seen that the idea of negative refraction in PhC is possible, but we must be very careful with the observation of this phenomenon both experimentally and numerically. There are two main problems which must be taken into account. First, the similar value of the wavelength with the lattice parameter and in consequence the similar value with the size of the PhC involves that the edge effects and the diffraction effect of the photonic crystal have special relevance in the process. Secondly, the real measurable quantity to be numerically calculated, is not a snapshot of the electric field but the time averaged magnitude of the Poynting vector, which for a time harmonic plane polarized TE or TM wave accounts to the norm, or the intensity, of space dependent part of the electric or magnetic field. We can see these facts by making an analysis of some square lattice structures.

Actually, the superfocussing reported in Refs. [78, 79] is not an image, but due

to two factors mainly: The concentration of the electric field in the cylinders of an PhC and the self-waveguiding effect. We explain these two factors in the following subsections and show that they leave nothing to do with negative refraction and hence to imaging as initially interpreted. However it leads to interesting phenomena. To this aim, we study the same structure as that of these works [78, 79].

4.3 Response of the slab of a 2-D square photonic array to a point source

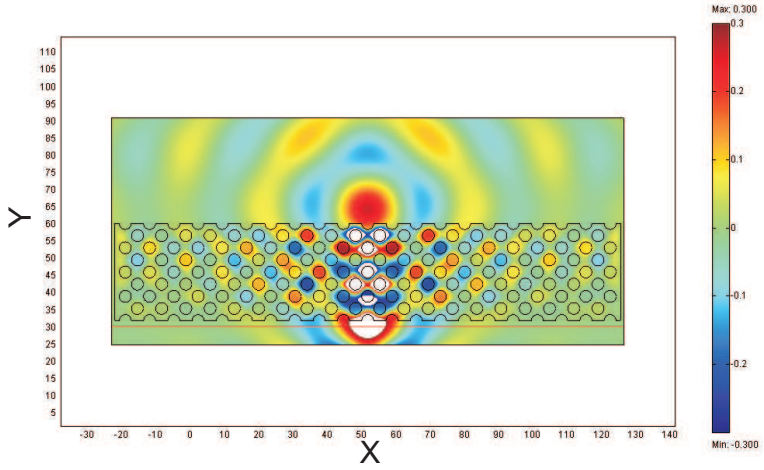

Figure 4.1: Maps of the magnetic field H_z for a point source in the input plane (red line) in front of a 2-D square lattice of air holes in a dielectric. One length unit is $a/5$.(Withe spots in the space of simulation are out of the color scale).

We first address a 2-D square lattice of air cylinders in a dielectric with permittivity $\epsilon = 12$, lattice constant a and radius $r = 0.35a$. This case was considered in [79]. We shall denote as the *input plane* that at which we specify the limiting value of the wavefield illuminating the array. This plane is taken at distance d of the entrance surface of the crystal. We shall first consider a point source, in the input plane, at distance $d = 0.35a$, which emits linearly polarized waves at normalized frequency $\omega = 0.195 \times 2\pi c/a$, c being the light speed in vacuum, with the magnetic vector $H_z(r,t) = H_z(r)cos\omega t$ parallel to the cylinder axis. We first record snapshots of $H_z(r,t_0)$ at different instants of time t_0. One of them coincides with the result of [79] but the position of this apparent focus is not stable (see Fig. 4.1 with snapshot at different time). This is better seen by computing $|H_z(r)|$ which corresponds to the stationary state (cf. Fig. 4.2), and constitutes the detected quantity for harmonic waves . As one can observe, the position of the peak intensity above the exit interface which should resemble a focus appears inside one half-cylinder of this interface, being

expelled upwards. Similarly happens for a point source emitting at $\omega = 0.192 \times 2\pi c/a$, with E_z along the cylinder axis, in front of a crystal consisting of dielectric cylinders with $\epsilon = 14$ and $r = 0.3a$ in air. Although one obtains for the field a snapshot at a certain instant t identical to that of [79] that again resembles a focus, it varies its position and size with time and, as before, its time averaged intensity given by the modulus $|E_z(r)|$ has an intensity maximum that comes from a cylinder of the exit interface. In either case, when the source is slightly shifted, so that it is placed in front of the space between two half-cylinders, as shown by Fig. 4.3, there is no one peak of intensity, but two peaks, each emanating from the two exit interface half-cylinders in front.

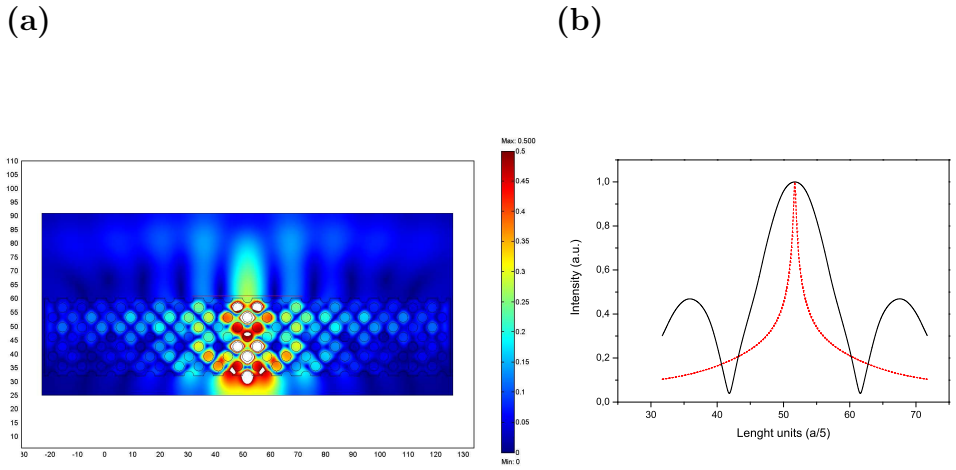

Figure 4.2: (a) Same as Fig. 4.1 but for the modulus $|H_z|$ of the magnetic field.(b) Normalized intensity for the point source (dashed red line) and the "image" in the exit interface (solid black line).

These results agree with those of [80] and suggest that the wave diffracted in the crystal has a preferential direction of propagation along the ΓM direction rather than being refracted. To test this, we address a slab of the same array symmetry, but with dielectric cylinders of $\epsilon = 9.61$, $r = 1.575mm$, $a = 4.79mm$ in air (This was employed in [78]). TM polarization is chosen. The band diagram, frequency of illumination of this structure is shown in Fig. 4.4(a).

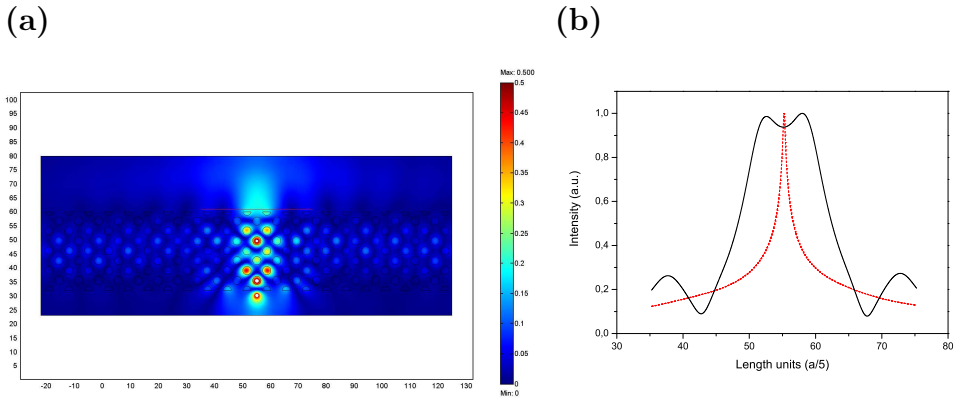

Figure 4.3: (a) Same as Fig. 4.2 but for a 2-D square lattice of dielectric cylinders for a point source. (b) Here the "image" (solid black line) has two peaks, the point source being in front of the space between two cylinders of the first row.

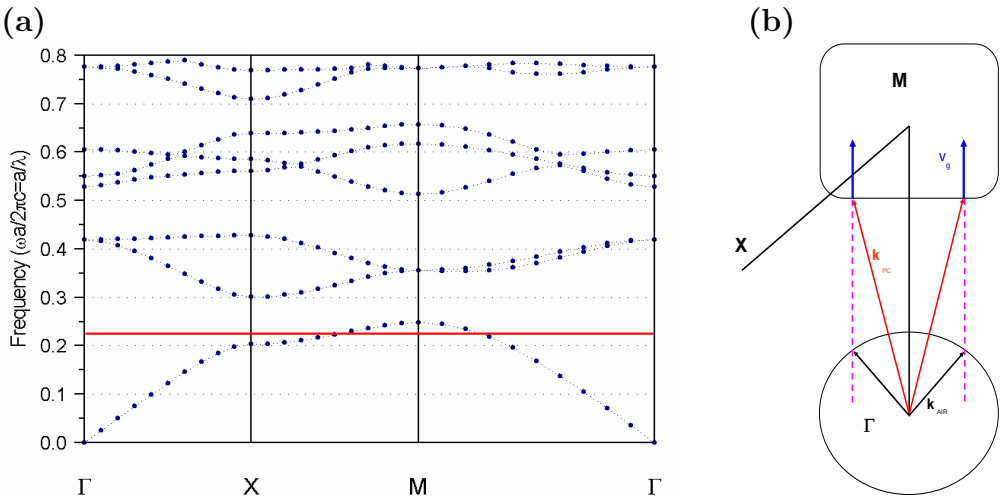

Figure 4.4: (a) Band diagram for the photonic crystal structure for TM polarization (E_z parallel to the cylinders) The illumination frequency is marked by the red line. (b) Isofrequency curves of air (bellow) and PhC(above) at this frequency. $\vec{v_g}$ is the group velocity.

The first experiment on negative refraction in PhC used cylinders of alumina in the microwave range and this work argued that negative refraction was observed. We show a simulation of this experiment in Fig. 4.5 (a) with a result nearly to that of the experiment of [78]. We could interpret it as a confirmation of negative refraction, but if we put absorbing walls in the edges of the PhC (Fig. 4.5 (b)) we avoid the diffractive and edge effects of the PhC, and observe that the transmission is normal

to the interface.

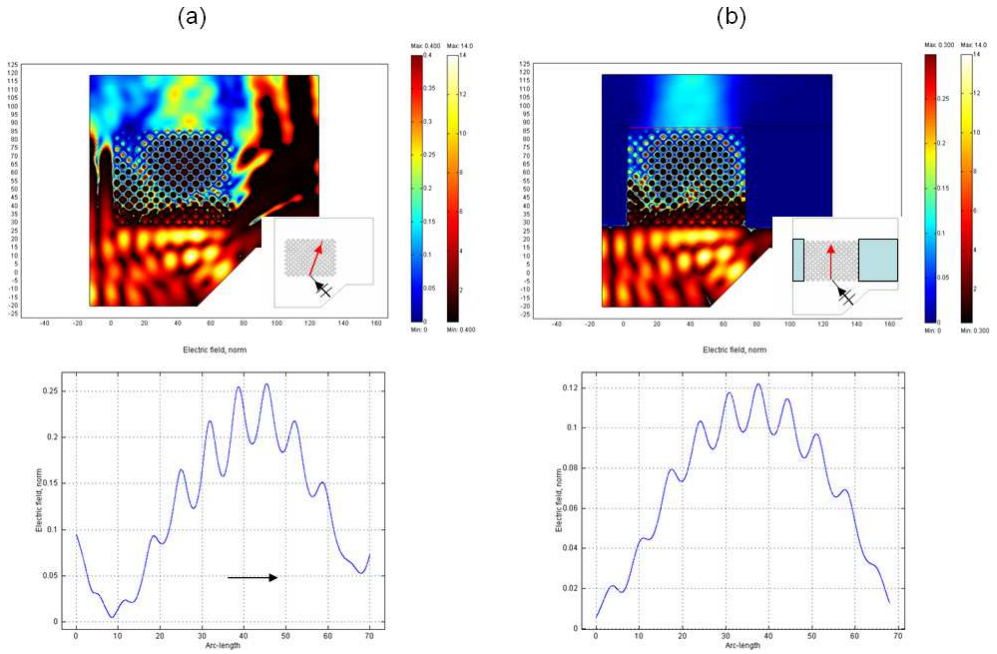

Figure 4.5: (a) Modulus of the electric field $|E_z(r)|$ of a beam impinges at 45° the bottom interface of a square lattice 2−D PhC, and, in the bottom profile in the exit interface of $|E_z(r)|$. (b) The same structure but we have situated absorbing walls in the sides of the PhC.

Furthermore, we have tested the wave propagation when a cylinder is removed in the center of the slab and replaced by a point source emitting at $\lambda = 21.88mm$. As shown in Fig. 4.6, propagation takes place along the ΓM direction, in agreement with [80], and the intensity is concentrated in the cylinders. This concentration appears because the frequency chosen is in the lower side of the bandgap (cf. Fig. 4.4(a)), namely in the so-called dielectric-band [81], and it is associated to a high permittivity. In fact, although not shown here, we have observed such a concentration by illuminating just one row and even one single cylinder; and it is this high concentration responsible for the localization of intensity in the surroundings of the cylinders in the exist surface of the slab. Its expelling to the air appears like a focus and so it may be interpreted from experimental measurements, as shown in previous figures and in Fig. 4.6. This dominance of propagation along ΓM can be understood from Fig. 4.4(b), where the group velocity v_g is normal to the isoline which has a very large flat portion.

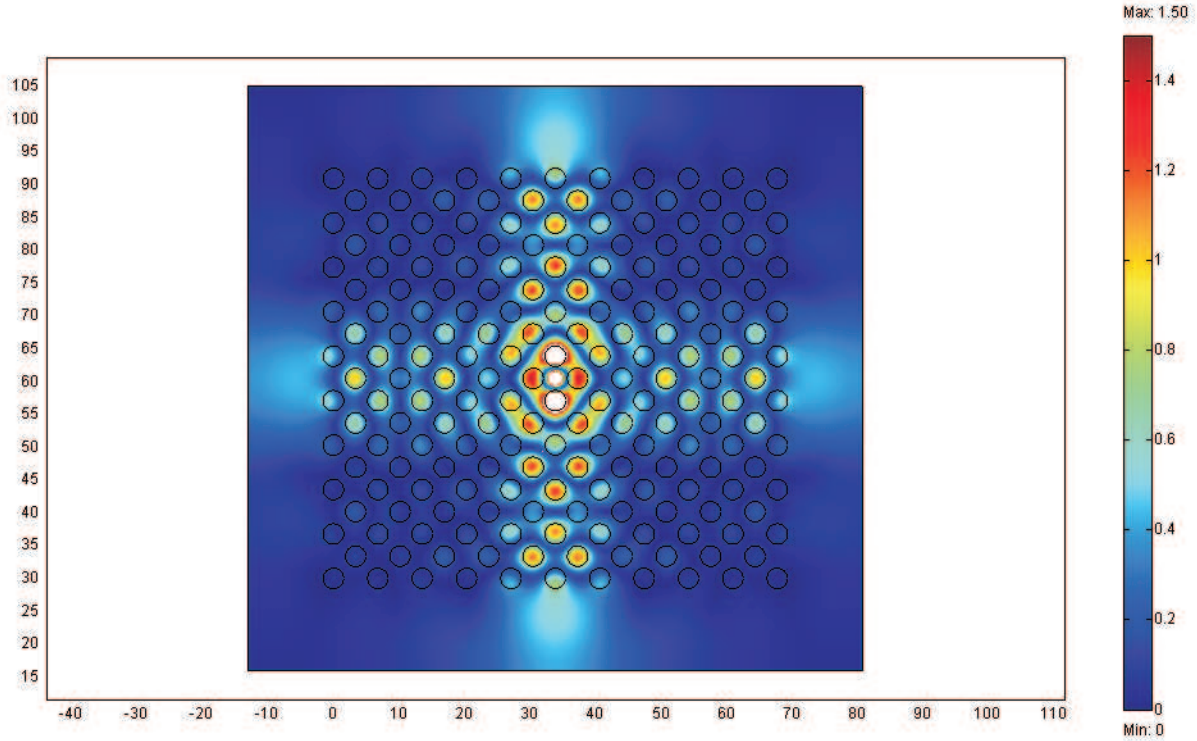

Figure 4.6: Maps of the modulus $|E_z(r)|$ of the electric field $\vec{E}$ for a point source emitting in a central defect of the photonic crystal and showing the directional propagation along ΓM.

This effect is further shown in Figs. 4.7, where two points sources are placed in front of the crystal. Fig. 4.7(a) corresponds to the same situation as in the experiment of [78], and thus detecting the signal at plane close to the exit surface of the slab yields two subwavelength width peaks that apparently look like the images of the sources (see Fig. 4.7(b)). However, when one varies the separation s between the point sources, there are no corresponding image peaks in the detection plane, but the intensity distribution at this plane depends on the distribution of light concentration in the cylinders of the exit interface; this is clearly seen in Fig. 4.7(b) for different separations s between the point sources. This dependence on the width of the illuminating wavefront is also consistent with observations in [78] according to which the "focusing" disappears as the source separates from the slab. To obtain additional confirmation of these effects, we have varied the number of rows in the slab, from 16 to 18. The field intensity distribution from two point sources is shown in Figs. 4.8(a) and 4.8(b), showing that it alternates between one and two peaks. They clearly prove that this

distribution depends on whether there are one or two cylinders of the exit surface with high field concentration inside. Given the symmetry of this array, this depends on whether the number of slabs is even (one peak) or odd (two peaks).

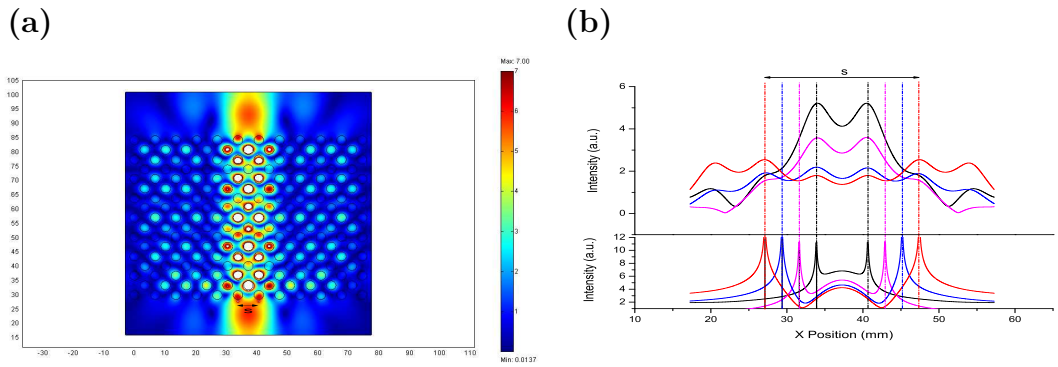

Figure 4.7: (a) Maps of the modulus $|E_z(r)|$ of the electric field $\vec{E}$ for two point sources separated a distance s from each other. (b) Intensity of the point sources (bottom) and the intensity of the "image" (top), at distance $0.7mm$ from the tangent plane to the top cylinders, for different values of s. The peaks abscissas coincide with those of illuminated cylinders.

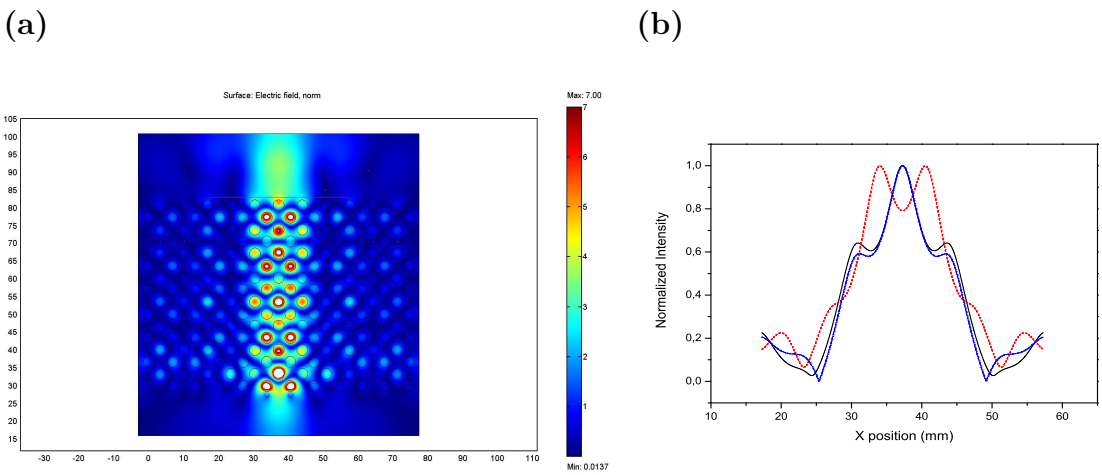

Figure 4.8: (a) Same as Fig. 4.7(a) but with the upper row removed. (b) Normalized intensity of the image in the case of Fig. 4.7(a), i.e. 16 rows (dashed red line) and of Fig. 4.8(a), namely, 17 rows (solid black line), and with 18 rows (dash-dot blue line) at the plane shown in (a) at distance $0.7mm$ from the tangent plane to the cylinders. In the three cases the peak abscissas fit with the position of the illuminated cylinders in the exit interface, and it is independent of the position of the two point sources.

4.4 Response of the square lattice photonic crystal slab to extended objects and wavefield distributions

To further study the response of these slabs to incident wavefronts, we now address their illumination by both extended object field distributions and to Gaussian beams. It is well known that an imaging system, and in particular a lens, should be space invariant, at least in a certain field region. This is given by the isoplanatic condition, according to which the image field distribution $i(x)$ is given in terms of the object wavefront distribution $o(x)$ by the convolution [10], [67] (see also Eq. (2.16))

Again in Eq. (2.16) $P(x)$ is the point spread function of the system, or response to a point source, (i.e., $P(x)$ constitutes the focus distribution), and as shown in chapter 2 and 3(sections 2.6 and 3.4.1, respectively), it allows, by Fourier transformation, to define a transfer function of the lens or optical system. This also involves that in the region of isoplanacity, the response $o(x_i)P(x - x_i)$ in the detection plane to each sampling point $o(x_i)\delta(x - x_i)$ of the object distribution in the input plane, only depends on the difference of coordinates $x - x_i$ and not on the position x_i. This defines the problem with our photonic crystal lens: there is no such a point spread function; the response to a point source depends on its location in the input plane, as proven by the previous examples.

The consequences are next discussed. Fig. 4.9(a) shows the response of the crystal slab to an extended object wavefront. The output is not an image but, again due to both directionality of propagation along ΓM and concentration at the exit surface cylinders, this output is similar to that of two point sources, (cf. Fig. 4.7(b)), and does not appreciably varies by changing the distance d of the input plane. On the other hand, Fig. 4.9(b) shows the response to a Gaussian beam that at the input plane has a FWHM of $2\sqrt{27}mm$. The result is similar to that of a point source emitting in front of a cylinder of the entrance surface and indicates a guiding of the wavefront along the ΓM direction of the crystal. Of course, increasing the beam width results in a broader section of the wavefront traversing the crystal and hence more cylinders of the exit surface being illuminated, thus yielding additional peaks in the detection plane, like in the case when two point sources are separated from each other at constant s, (cf. Fig. 4.7). To obtain additional confirmation of these effects, we have varied the number of rows in the slab. Removing the last row of cylinders, i.e. that of the exit interface, each time, produces a field intensity distribution as displayed in Fig. 4.9(b), showing that it alternates between one and two peaks, thus clearly proving that this distribution depends on whether there are one or two cylinders of the exit row possessing high field concentration inside. Given the symmetry of this array, this depends on whether the number of slabs is even (one peak) or odd (two peaks), and can also be observed in the intensity of the field emerging in front of the vertical and horizontal exit surfaces of Fig. 4.6 which have the parity exchanged with respect to

each other. In neither situation any actual image is formed.

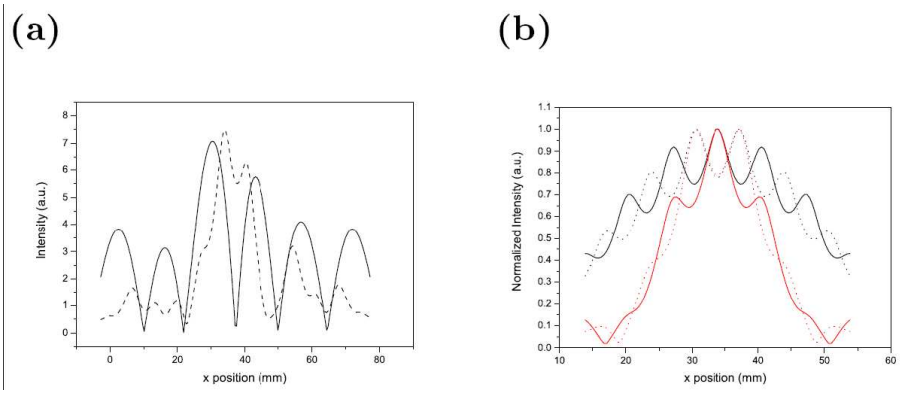

Figure 4.9: (a)Extended object wavefield intensity (solid black line) at the input plane situated at distance $d = 0.7mm$ from the slab and intensity in a plane away $0.7mm$ from the tangent plane to the cylinders of the exit row interface of the PC (dashed)(b)Normalized intensity in a plane $0.7mm$ away from the exit row of the response of the PC to a Gaussian beam of $FWHM = 2\sqrt{27}mm$ (solid red line) and with the upper row removed (dashed red line) and a Gaussian beam with $FWHM = 30mm$ (solid black line) and the same respectively (dashed black line) but with the upper row removed. The peak abscissas coincide with those of illuminated cylinders.

4.5 Waveguiding and bending in a self-collimated photonic crystal

All previous results suggest that, aside from reflections at the entrance interface, the ΓM direction of propagation makes the structure to act as a guide for the incident wave. This is confirmed by Fig. 4.10(a) corresponding to a Gaussian beam incident on a prism whose entrance interface is parallel to the XM direction and the beam propagates in the ΓM direction.

Furthermore, if we insert a Gaussian beam into a prism with the entrance interface perpendicular to the ΓM direction and with a tilt angle $\phi = 45^o$ (i.e. whose exit interface is perpendicular to the XM direction) the beam can be also bent as Figs. 4.10(b) and 4.10(c) show. This bending is due to the conservation of the component of $\vec{k}$ parallel to the reflection interface.As shown in Fig. 4.10(d), most of the propagating vectors $\vec{k}_{PC}$ inside of photonic crystal do not provide a permitted propagating wavevector $\vec{k}_{air}$ in the air which satisfies this parallel component conservation. Furthermore, on reflection we obtain an evanescent wave in the air that, due to the finite size of the Gaussian beam, travels across the interface (i.e. along the interface

cylinders) a distance $\Delta d \simeq 2a$ like in the shift of usual total internal reflection (we analyze this effect in the next section) .

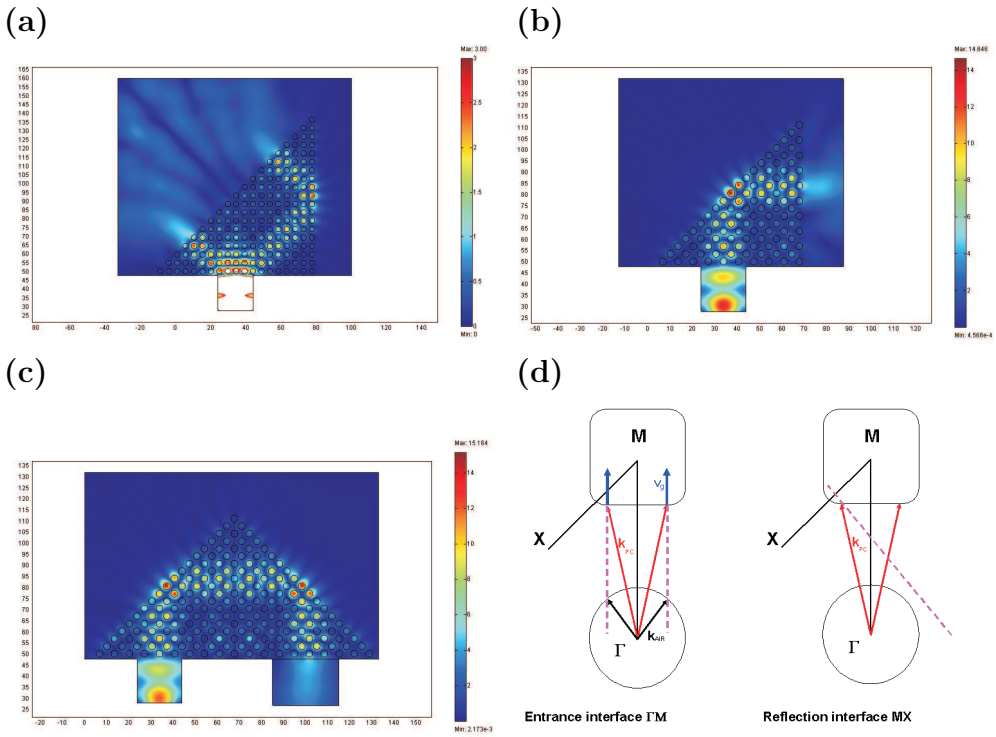

Figure 4.10: Maps of the modulus $|E_z(r)|$ of the electric field $\vec{E}$ for (a) a Gaussian beam entering in a prism in the interface parallel to XM, (b) and (c) a Gaussian beam entering in a prism in the interface parallel to ΓM and reflection in the tilted interfaces. (d) Isofrequency lines in air and in the PC, and illustration at the entrance (left) and at the reflection interface (right). Conservation of the parallel component of $\vec{k}$ at the entrance interface gives a broad range of k-vectors in the PC giving rise to group velocity vectors normal to the flat portion of the isofrequency line and thus propagating in the ΓM direction. On the other hand, conservation of the parallel component of $\vec{k}$ at the reflection interface gives rise to almost all k-vectors in air being evanescent (i.e. outside the $k = \omega/c$ circle).

Due to the symmetry of the crystal, only $\phi = 45^o$ provides this total internal reflection. With a tilt angle larger than 45 degrees, there appears a refraction process governed by the Bragg law $k^{\parallel}_{air} = K^{\parallel}_G + k^{\parallel}_{PC}$, where $K^{\parallel}_G$ is the parallel component of the reciprocal lattice vector, coming from higher order Brillouin zones. This is seen in Fig. 4.11(a) for a prism with $\phi = 64.43^o$; the angle of refraction θ_1 coincides with that given by the isofrequencies lines in the second Brillouin zone, as shown by Fig. 4.11(b).

Also, from the conservation of the parallel components in the Bragg law in the process of reflection, we show in Fig. 4.11(c) that for every tilt angle ϕ, the angle of reflection is always in the ΓM direction, i.e. at 90 degrees with the beam incident on the prism. Similarly, the angle of refraction θ_2 in the right exit interface, as seen in the field distribution of Fig. 4.11(a), fits with that displayed in Fig. 4.11(d).

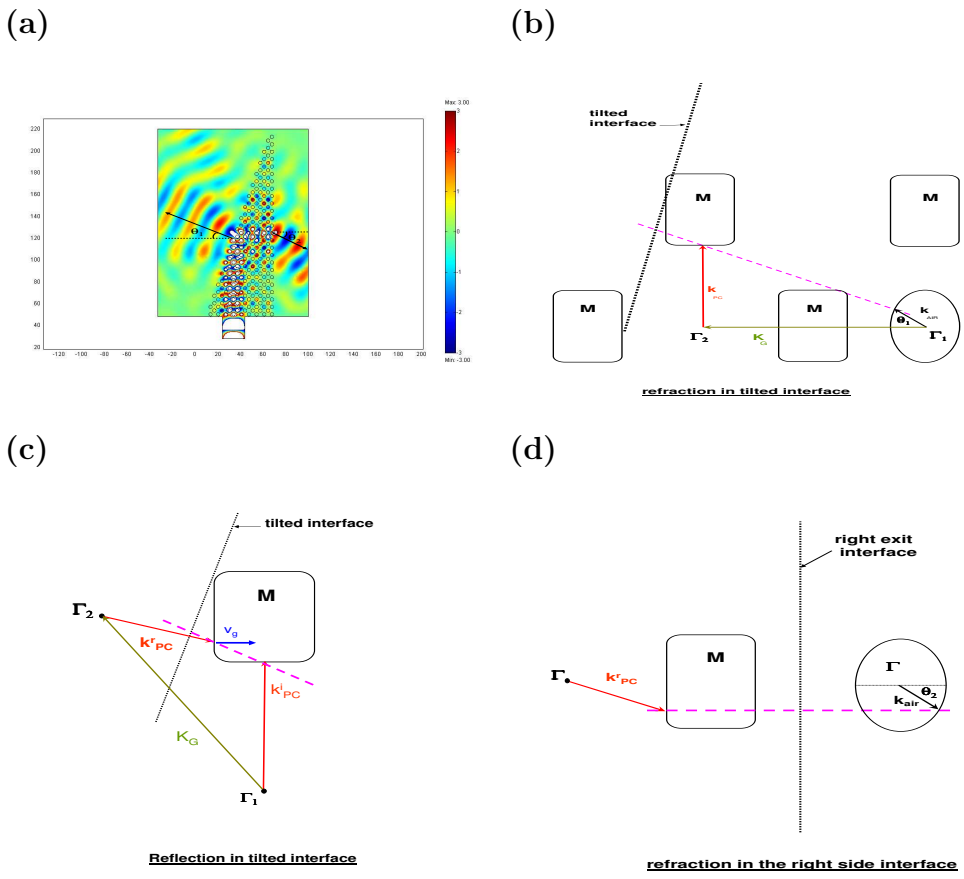

Figure 4.11: (a) Map of the electric field E_z for a prism with a tilt angle $\phi = 63.43°$. (b) Conservation of the parallel components in the Bragg law for the tilted interface for refraction, where Γ_2 is the origin of the second Brillouin zone. Notice that the pink broken line is normal to the tilted interface direction. The point at which this line crosses the air isofrequency circle marks the orientation of the refraction k-vector. (c) Conservation of the parallel components of the Bragg law for the tilted interface in the reflection process. (d) conservation of the component of k parallel to the right side interface in the refraction process.

4.6 Beam lateral shift in a self-collimated photonic crystal

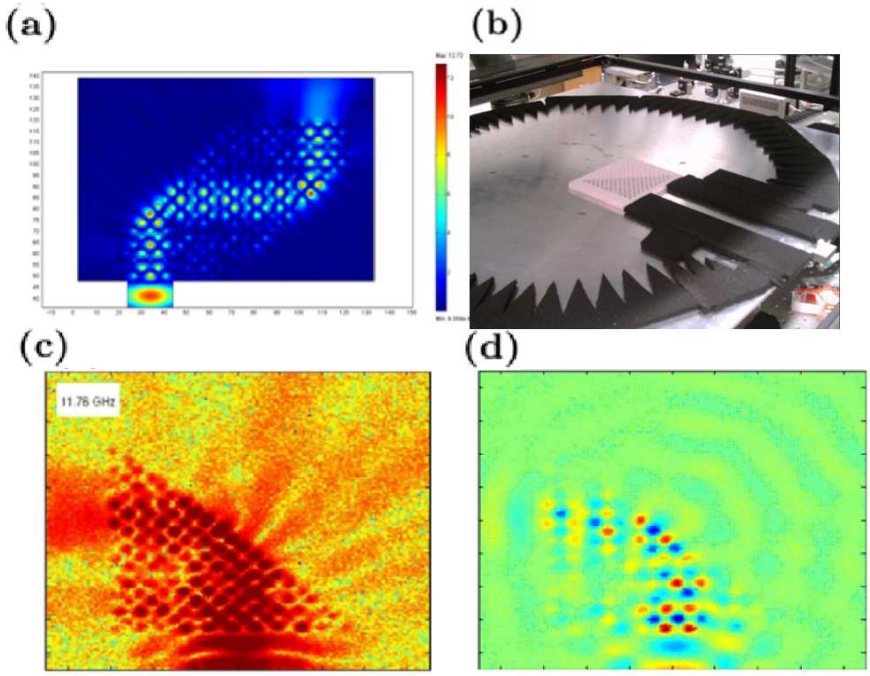

Figure 4.12: (a) Map of the modulus of the electric field $|E|$ in the configuration of the numerical simulation: An incident Gaussian beam impinges the photonic crystal (PC) of dielectric cylinders from the bottom and suffers two total internal reflections at the PC boundaries. (b) Experimental setup with photonic crystal array (c) Experimental data showing the map of intensity with one total internal reflection at an interface parallel to the XM direction in a prism of the same PC of dielectric cylinders on which the beam enters from below. (d) (movie) snapshot of the experimental recorded electric field E_z, showing the field phase in this total internal reflection.

It is well know that totally reflected beams at a dielectric-air surface suffer a lateral shift. This is the extensively studied Goos-Hänchen effect [82]. The wave components that compose an incident Gaussian beam suffer a nonuniform phase shift upon reflection and contribute to a net offset of the beam. Energy flow between the incident and shifted reflected beam is mediated by evanescent waves in the transmission side (air) of the interface. A similar effect has been discussed in photonic crystals (PhC) when a Gaussian beam impinges from the air with a frequency in the bandgap [83, 84]. In this section we demonstrate another photonic crystal beam shifting phenomenon that arises when a guided beam, propagating in the self-waveguided crystal, is reflected at

the crystal/air interface. This has a certain analogy with the aforementioned Goos-Hänchen shift, but as we have seen before, this total internal reflection occurs at only one angle of incidence.

We performed an experiment to investigate the beam position when total internal reflection takes place at the PhC boundary. We first numerically simulating a path design based on the experimental setup by Goos and Hänchen [82, 85], which exhibits two total internal reflections, after which the beam propagates outside the photonic crystal, (cf. Fig. 4.12(a)). In the experiment [86] we only make one total internal reflection due to the limiting space imposed by the experimental setup (Fig. 4.12(b),(c),(d)). We consider a Gaussian incident beam, with constant amplitude electric vector E_0, linearly polarized parallel to the axis of the cylinders, and width $\sigma = 14mm$, impinging at the bottom surface of the crystal and transmitted within it along the ΓM direction. After penetrating, it is self-guided up to the interface where it impinges at an angle of 45 degrees perpendicular to the XM direction. At this interface, a first total internal reflection is produced, along with the appearance of an evanescent wave transmitted into the air. This reflection is repeated a second time at the next interface as illustrated in Fig. 4.12(a). These reflections bend the beam. This is due to the conservation of the component of the $\vec{k}$ wavevector parallel to the reflection interface. As shown in Fig. 4.10(d) and the previous section, most of the propagating vectors $\vec{k}_{PhC}$ inside the photonic crystal do not provide a permitted propagating wavevector $\vec{k}_{air}$ in the air that satisfies this parallel component conservation. Due to the symmetry of the crystal, only incidence under $\varphi = 45°$ provides this bending by total internal reflection. When the tilt angle is larger than 45 degrees, there appears a refraction process governed by the Bragg law $k_{air}^{\parallel} = K_G^{\parallel} + k_{PhC}^{\parallel}$, where $K_G^{\parallel}$ is the parallel component of the reciprocal lattice vector, coming from higher order Brillouin zones. It is at this unique angle $\varphi = 45°$ of the crystal frontier row that at which the beam lateral shift occurs and is studied.

We next show the experimental setup that we performed at Duke University [86] to test some of these results.

4.6.1 Experimental setup

We have built a two dimensional square photonic crystal lattice made of cylinders of flint glass (0080 Corning glass) with permittivity $\epsilon = 7 + 0.08i$ in the studied range of frequencies, in a matrix of Styrofoam. The refractive index n of Styrofoam is very approximately $n = 1$ at these frequencies. The crystal has a lattice constant $a = 7.57mm$ and the cylinder radius r is $r = 0.35a = 2.65mm$. The crystal is illuminated at a frequency $\nu = 11.76\ GHz$. To this aim, the sample was introduced in a parallel-plate waveguide which is comprised of two flat conducting (Al) plates spaced 11 mm apart. Microwaves were introduced through an X-band (8 to 12 GHz) coax-to-waveguide adapter that was attached to the lower plate. A 1.5 cm wide guide was constructed out of 10 dB/cm absorber along the path from the antenna to the

sample to form the incident beam. The sample rested on the lower plate and was nearly of the same height (10 mm) as the plate separation. A field-sensing antenna was formed from a coaxial fixture inserted into a hole drilled through the upper plate. The center conductor and dielectric of the coaxial connector extended to a position flush with the lower surface of the upper plate and did not protrude into the chamber volume. The lower plate was mounted on two orthogonal linear translation stages, so that the lower plate (including the photonic crystal prism, waveguide feed, and absorber) could be translated with respect to the upper plate and to the detector. By stepping the lower plate in small increments and recording the field amplitude and phase at every step, a full 2D spatial field map of the microwave scattering pattern could be acquired both inside the sample and in the surrounding free-space region.(See Fig. 4.12(b))

4.6.2 Results

To evaluate the reflected beam shift S, we measured the position of the beam peak after exiting the crystal, far enough to avoid possible modulations due to the influence of the intensity concentration in the cylinders of the last row [87]. Another interesting characteristic of this beam shift on total internal reflection in a self-guiding photonic crystal, is that it keeps almost constant as the exterior index n_2 varies (Fig. 4.13). This behavior may be due to the existence of the unique angle 45 degrees of total reflection, together with the existence of a coupling with propagating modes inside the photonic crystal, independently of the exterior medium. This implies that another effect is involved in the process of total internal reflection.

Finally, we have investigated the influence of the termination, or truncation, of the cylinders that form the surface of total internal reflection. This truncation has been studied in several works for different geometries with the aim of avoiding losses associated with radiation of surface modes [88, 89, 90], or beaming transmitted light by means of surface modes [91, 92] . We have introduced the cut parameter to define the termination of the crystal (in this case $\tau = r$ corresponds to a hemicylinder and $\tau = 2r = 5.3mm$ to the complete cylinder; see inset of Fig. 4.14).

Fig. 4.14 shows that the beam shift S reaches a maximum about $\tau = 1.57r = 4.16mm$ whereas S is minimum for $\tau < r = 2.65mm$. This minimum is due to the existence of the surface modes which exponentially decay on both sides of the interface. These modes coexist inside the photonic crystal with propagating modes at the same frequency, and their wavevector k_x is smaller than that of the propagating modes, (cf. Fig. 4.15). To demonstrate it, we have employed the supercell method in which slabs of dielectric cylinders alternate with slabs of air [88]. Therefore, for certain cuts, the surface mode and propagating modes both constructively and destructively interfere, leading to a higher or smaller beam shift, respectively.

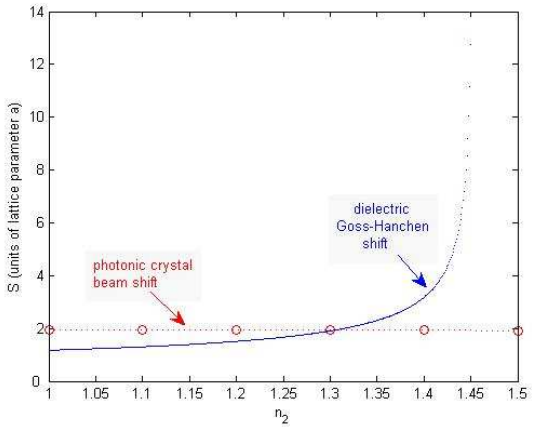

Figure 4.13: Numerical results of the beam shift S as a function of the exterior refractive index n_2 for a photonic crystal with complete cylinders(red dashed line) on comparison with the beam shift produced by a dielectric (blue solid line) with an effective refractive index similar to the effective index of the photonic crystal.

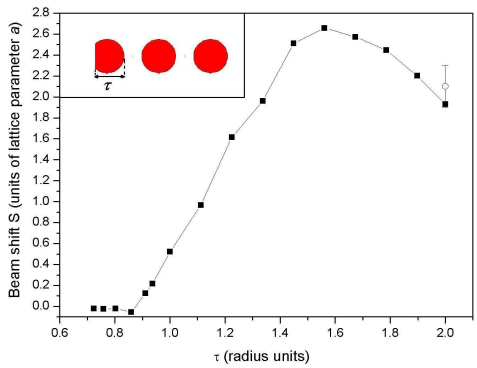

Figure 4.14: Variation of the beam shift S versus the cut parameter τ numerical (solid squares) and experimentally (open circles), (see inset: truncation in the last cylinder row and representation of the cut parameter τ).

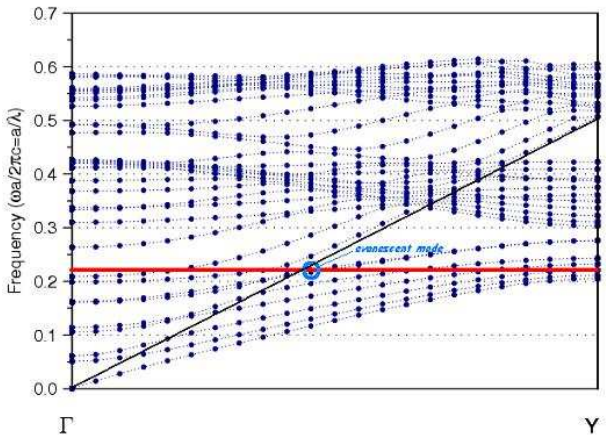

Figure 4.15: Band diagram for the photonic crystal supercell, with an evanescent surface mode for a cut $\tau = 4.16mm$. The work frequency (solid thick red line) is shown

4.7 Scanning device and subwavelength concentrator

The self-guiding effect, and the intensity peaks concentration in the cylinders, indicate that sharpening the edges of the crystal sample, one should produce high field intensity concentrations in the vertex. As a matter of fact, this allows us to design devices of use e.g. in scanning procedures over sample surfaces. Fig. 4.16(a) shows a two apex 2-D crystal of the latter cylinder array. Fig. 4.16(a) shows the self-guiding, as well as both the collection in the bottom vertex and concentration on the top apex. Specifically, the lower apex, in front of a slit that acts as a collimator, are both raster-scanning the wavefront emerging from an object surface, while the upper apex is the collector of the response of this crystal array to the input intensity emerging from the slit. As shown in Fig. 4.16(b), the scanning reproduces at the collector apex the response to the successive values of the intensities from the source (the slit) as the object wavefront is scanned. The efficiency of this structure is 20%, which is mainly limited by the transmittance of the slit, since the net intensity transmission through the crystal up to the output in the tip is about 80%.

A tailored shape of this array can guide the incident wavefront up to a pencil-shaped tip that concentrates the wave from an incident beam. Figure 4.17 (a) illustrates this process: a Gaussian beam of FWHM being $12.65mm$ is guided reaching a tip-shaped appendix of the structure. As seen in Fig. 4.17(b), the subwavelength concentration effect is larger the wider the beam is and also can be improved when

the last cylinder in the apex is further sharpened with a peak shape.

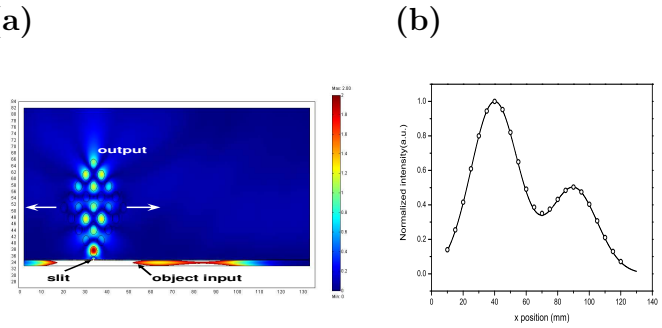

Figure 4.16: (a)Map of the modulus $|E_z(r)|$ of $\vec{E}$ of a two-apex crystal.(b) Intensity of the wavefront emerging from an extended object, (solid line), compared with the output signal, (open circles), close to the upper apex when the lower apex, and an aperture close to it, raster scan the object wavefront. Both signals are normalized to unity. The peak of the output is the same as that of the object.

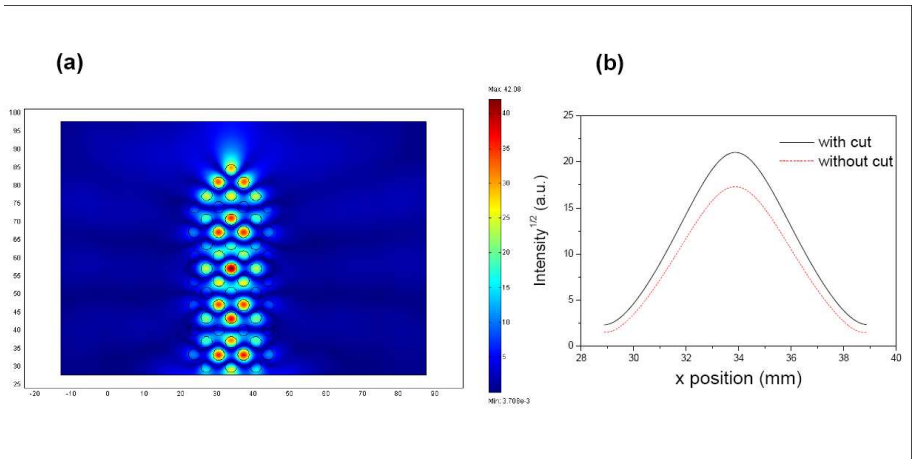

Figure 4.17: (a) Map of the modulus $|E|$ of the electric field for a Gaussian beam coming from the bottom into a the photonic crystal tip structure with the two external cylinders on both sides of the tilted interfaced cut and (b) profile of the square root of the intensity at $1.1mm$ of the last cylinder for a tip without cut, i.e. complete cylinders (dashed line) and with a cut $\tau = 4.16mm$ in the external cylinders of the interface (solid line).

Finally, it should be remarked that possible applications of a beam shift have been reported before [93, 94]. In this way taking into account the characteristics described

before about the lateral shift, we have improved this subwavelength concentrator cutting the two outer cylinders with the cut parameter around $\tau = 4.16mm$, in order to focus the most external rays onto the apex cylinder, therefore getting more concentrated intensity (Fig. 4.17(b)).

4.8 The superprism effect

Another effect observed in PhC due to the shape of the isofrequency lines is the so called superprism effect. This phenomenon shows the dispersion of light being 500 times stronger than the dispersion in conventional prisms. It was demonstrated at optical wavelengths in photonic crystals (PhCs) fabricated on Si. Drastic light-beam steering in the PhCs was achieved by slightly changing the incident wavelength or angle.(Fig. 4.18)

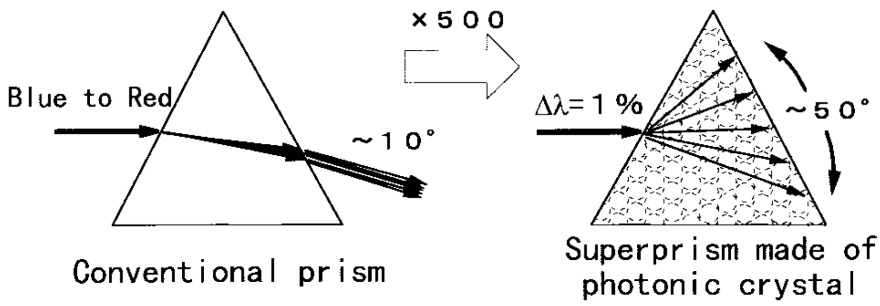

Figure 4.18: Schematic illustration of superprism phenomena. The wavelength dispersion in a superprism made of PhCs is approximately 500 times stronger than in a prism made of conventional crystals. After Ref. [95].

Lin et al. reported an interesting phenomenon in the radio frequency range that they called highly dispersive prism [96]. They designed an array of alumina rods to deflect radio waves by tuning the energy near the photonic band gap. The deflection, unfortunately, was of magnitude comparable to that obtained from a conventional prism or grating. By contrast, Kosaka et al. [95] have demonstrated the superprism effect. The physics underlying these two phenomena are totally different. Lin et al. assumed isotropic dispersion, and attributed the deflection to the modification of the refractive index through the nonlinearity in the dispersion relation determined by the photonic band structure. By contrast, Kosaka et al. intentionally introduced anisotropy in the dispersion and observed the propagation direction of light determined by the group velocity. In other words, the fundamental difference can be associated to that between the phase velocity and the group velocity. As a result,

the light dispersion that they obtained was much larger than that obtained with conventional prisms or gratings.

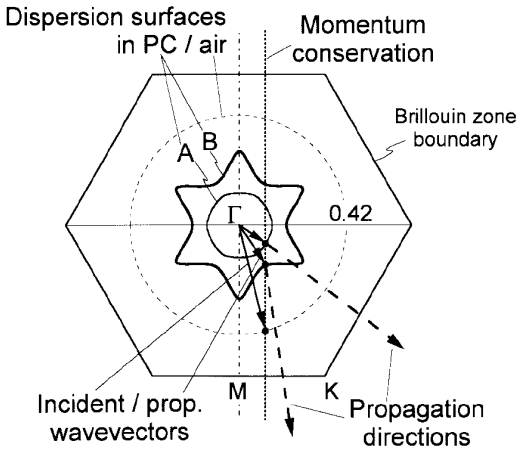

Figure 4.19: Equi-frequency contours called dispersion surfaces at the frequency cut−of for TE modes. The process used to derive the propagation direction is shown: the normal vector at the intersection of the dispersion surface and the construction line (through the end of the incident wavevector and normal to the crystal edge) gives the propagation direction. After Ref. [95].

The remarkable difference introduced by these results is, however, that the dispersion surfaces in PhC's show a variety of shapes in contrast to the circular or ellipsoidal shapes in conventional crystals. As an example, dispersion surfaces at the frequency cut of for TE modes are shown in Fig. 4.19. The apparent distortion from the circular shape and the multiplicity of the dispersion surface are the origins of the phenomena.

The process for obtaining the propagation direction from these dispersion surfaces is graphically illustrated in Fig. 4.19. First, the propagation wavevectors are obtained through the momentum conservation rule, which is the continuity condition between the incident wavevector and the propagation wavevector for the tangential components parallel to the incident crystal edge . Then the propagation directions are obtained being normal to the dispersion surface at the end point of the propagation wavevector. This process is used because the propagation direction is determined by the energy velocity, which is exactly the same as the group velocity in a periodically distributed material without losses [27], [28]. We used that the group velocity points to the gradient direction of dispersion surfaces at a wavevector

4.9 Conclusions

Although the mechanism of negative refraction is not responsible for the subwavelength intensity concentration at the exit of the crystal slab of some photonic crystal structures previously investigated, constituted by 2-D arrays of high index cylinders in air, or viceversa, since at those working wavelengths it is rather the directional propagation in the ΓM direction, and the intensity concentration inside the cylinders of the crystal, in the lower frequency band, the cause of this effect, (in this respect, a part of our conclusions agree with previous observations in [80], [97], [71]), we have proven, however, an alternative use of these structures, in which multiple diffraction is responsible for waveguiding, bending, and subwavelength intensity concentration in tailored samples of these arrays. In particular, this subwavelength concentration phenomenon may be of particular interest when extended wavefronts, like beams, are incident on the structure. Alternatively, this precess suggests its use in scanning tip devices.

Chapter 5

Split ring resonator based metamaterial coupled to two level system gain medium

5.1 Motivation

We have seen in the previous chapters that the losses constitutes one of the main problems in the metamaterials, also we have seen that the PhCs have several limitations which a lossless metamaterial should not have. If losses in the metamaterials could be eliminate or compensate many of the applications in microwaves metamaterials (where the losses are lower) such as perfect lens or cloaking might get it. A possible way to counteract the losses in a metamaterial is coupling to a gain medium. In this chapter, we develope a simple model in order to understand and find the physics and restrictions of the Lasing Spaser system. We found several characteristics that are useful for a future experimental realization.

5.2 Introduction

The concept of Lasing SPASER (surface plasmon amplification by stimulated emission) was introduced by Bergman and Stockman [98], where a strong coherent field is achieved in a region much smaller that the wavelength. In a theoretical work, Zheludev developed the lasing Spaser combining a gain medium with an array the metamaterials. In these microscopic calculations [99] based on numerical solutions of the three-dimensional vector Maxwell equations for specific metal nanostructures, the gain medium has been described by a constant (i.e., frequency-independent and emission-independent) negative imaginary part of the gain medium dielectric function. Clearly, it is interesting to investigate modifications of this result due to a more realistic frequency-dependent gain, gain pinning, and dynamic effects.

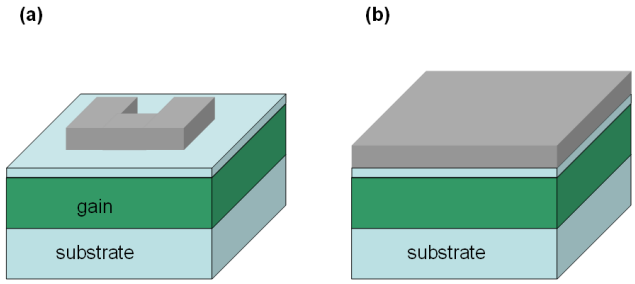

Figure 5.1: (a) Schematic illustration (not to scale) of a possible geometry for bringing the optical gain from a thin semiconductor film (bulk, quantum wells, or quantum dots) close to an array of, e.g., plasmonic split-ring resonators (one unit cell is shown). This geometry aims at taking advantage of local-field-enhancement effects. The electric-field vector lies in the layer plane. (b) Schematic illustration of the toy model for a plasmonic (bosonic) metamaterial resonance coupled to a (fermionic) two-level-system gain resonance via local-field interactions. This interaction is described by the phenomenological (Lorentz) parameter $\mathcal{L}$.

In this chapter, we rather propose a simple general toy model based on a fermionic two-level-system resonance (representing the gain medium, e.g., semiconductor quantum dots) and a single bosonic resonance (representing the plasmonic resonance of the metamaterial), connected to each other via a local-field coupling analogous to the local-field Lorentz factor. Interestingly, our toy model can be solved analytically for (quasi-) steady-state conditions. Numerical solutions for the time-dependent case are also discussed.

5.3 Definition of the model

The physics of our toy model is graphically illustrated in Fig. 5.1. The key to the model are the local field (or evanescent-field) interactions, i.e., the local electric field of the two-level system (2LS) is given by the external electric field E

$$E(t) = E_0 cos(\omega t) = \frac{E_0}{2}(exp(-i\omega t) + c.c.) \tag{5.1}$$

of the light plus a phenomenological constant, $\mathcal{L}$, times the polarization of the bosonic mode, P_{pl}, i.e.,

$$E \Rightarrow E + \mathcal{L}P_{pl} \tag{5.2}$$

Correspondingly, the local electric field of the bosonic mode is given by the external electric field plus constant $\mathcal{L}$ times the polarization of the 2LS, P_{2LS}, i.e.,

$$E \Rightarrow E + \mathcal{L}P_{2LS} \tag{5.3}$$

As the spatial separation between 2LS and plasmonic resonance is increased (see Fig. 5.1 (a)), the coupling via the plasmonic evanescent field decreases and $\mathcal{L}$ approaches zero. Note that we have omitted the self-interactions, which can generally also occur via the local fields. In linear optics, however, self-interaction merely renormalizes the effective resonance center frequency. Mathematically, the equations of motion for a fermionic two-level system are the famous and well known optical Bloch equations [100]. They can be arranged into the form

$$\dot{p}_{2LS} + (i\Omega_{2LS} + \gamma_{2LS})p_{2LS} = i\hbar^{-1}d_{2LS}E(1-2f), \tag{5.4}$$

$$\dot{f} + \Gamma_{2LS}f = i\hbar^{-1}(p^*_{2LS}d_{2LS}E - p_{2LS}[d^*_{2LS}E^*] \tag{5.5}$$

Here p_{2LS} denotes the (dimensionless) complex transition amplitude, $f = f_{2LS}$ the occupation probability of the upper level, d_{2LS} the dipole matrix element, E the (external) electric field, Ω_{2LS} the transition frequency, γ_{2LS} the damping (or transverse relaxation) rate, and 2LS the population (or longitudinal) relaxation rate. The individual electric dipole moment is given by the product $d_{2LS}p_{2LS}$. Multiplying with the volume density of two-level systems, N_{2LS}, leads to the macroscopic 2LS polarization P_{2LS}, i.e., to $P_{2LS} = N_{2LS}d_{2LS}p_{2LS} + c.c.$. The equations of motion for a corresponding single bosonic mode are strictly identical to (5.4) and (5.5), except that the inversion factor $(1-2f)$ in equation (5.4) has to be replaced by unity, i.e.,

$$\dot{p}_{pl} + (i\Omega_{pl} + \gamma_{pl})p_{pl} = i\hbar^{-1}d_{pl}E. \tag{5.6}$$

Hence, the equation for the occupation f_{pl} of the bosonic mode becomes irrelevant. In analogy to the 2LS, the macroscopic plasmonic polarization is given by $P_{pl} = N_{pl}d_{pl}p_{pl} + c.c.$. As discussed above, we assume that the coupling between the two resonances is governed by *local-field effects*. Under these conditions, we simply have to replace the electric fields E in (5.3) and (5.4) by the term given in (5.1) and the electric field E in (5.5) by (5.2). We envision that the 2LS is pumped via a third energy level, resulting in an additional effective pump rate, pump, of the two-level system on the right handed side of (5.4). To avoid confusion: Generally, plasmonic nanostructures can have both an electric-dipole and a magnetic-dipole response [101]-[102]. Here, we have focused on the electric-dipole response (leading to the polarization P) as only that can couple directly to available gain media at optical frequencies. Thus,

our model is not applicable directly to magnetic-dipole plasmonic resonances or to negative-index metamaterials. Yet, it may provide qualitative trends. Our model is applicable directly to, e.g., the electric-dipole (Mie) resonances of the "V" structures envisioned in Ref. [98]. Next, we discuss analytical and numerical solutions of the model defined so far.

5.4 Linear response for fixed occupation

First, we consider the case of a given (i.e., fixed) occupation f of the 2LS and calculate the linear optical response. This assumption of fixed f is meaningful under transient but quasi-steady-state conditions, for example, following the excitation with a short pump pulse (via the pump rate described above). Under these conditions, it is straightforward to solve the above coupled equations. Using the usual rotating-wave approximation (RWA) [100], we derive the transition amplitudes $p = \tilde{p} \cdot exp(-i\omega t)$

$$\tilde{p}_{2LS} = \frac{(1-2f)\left(\hbar^{-1} d_{2LS} \frac{\tilde{E}_0}{2} + \frac{V_{2LS}\hbar^{-1} d_{pl} \frac{\tilde{E}_0}{2}}{(\Omega_{pl}-\omega)-i\gamma_{pl}}\right)}{(\Omega_{2LS}-\omega) - i\gamma_{2LS} - (1-2f)\frac{V_{pl}V_{2LS}}{(\Omega_{pl}-\omega)-i\gamma_{pl}}} \tag{5.7}$$

and

$$\tilde{p}_{pl} = \frac{\hbar^{-1} d_{pl} \frac{\tilde{E}_0}{2} + V_{pl}\tilde{p}_{2LS}}{(\Omega_{pl}-\omega) - i\gamma_{pl}}. \tag{5.8}$$

Here, we have introduced the two resulting coupling frequencies

$$V_{2LS} = \hbar^{-1} d_{2LS} \mathcal{L} N_{pl} d_{pl} \tag{5.9}$$

$$V_{pl} = \hbar^{-1} d_{pl} \mathcal{L} N_{2LS} d_{2LS} \tag{5.10}$$

describing the effective back-action of the plasmonic mode onto the 2LS and vice versa, respectively. Note that the numerator of the 2LS transition amplitude in (5.7) shows the anticipated resonant enhancement of its "oscillator strength", hence of its absorption/gain, via the plasmonic resonance. Strictly speaking, this resonance indexed by "2LS" is a mixed mode composed of the 2LS and the plasmonic resonance. Only for zero coupling, this resonance becomes that of the 2LS. The denominator of (5.7) also contains a resonance. This aspect can be interpreted as an eigenfrequency and a damping that are effectively frequency dependent, hence, this aspect gives rise to non-trivial lineshapes. As p_{2LS} also enters in the numerator of (5.8), the spectral dependence of p_{pl} is quite complex as well. The resulting is a macroscopic polarization for each layer obtaining individually the optical susceptibility χ_i or the effective electric permittivity $\epsilon_i = 1 - \chi_i$.

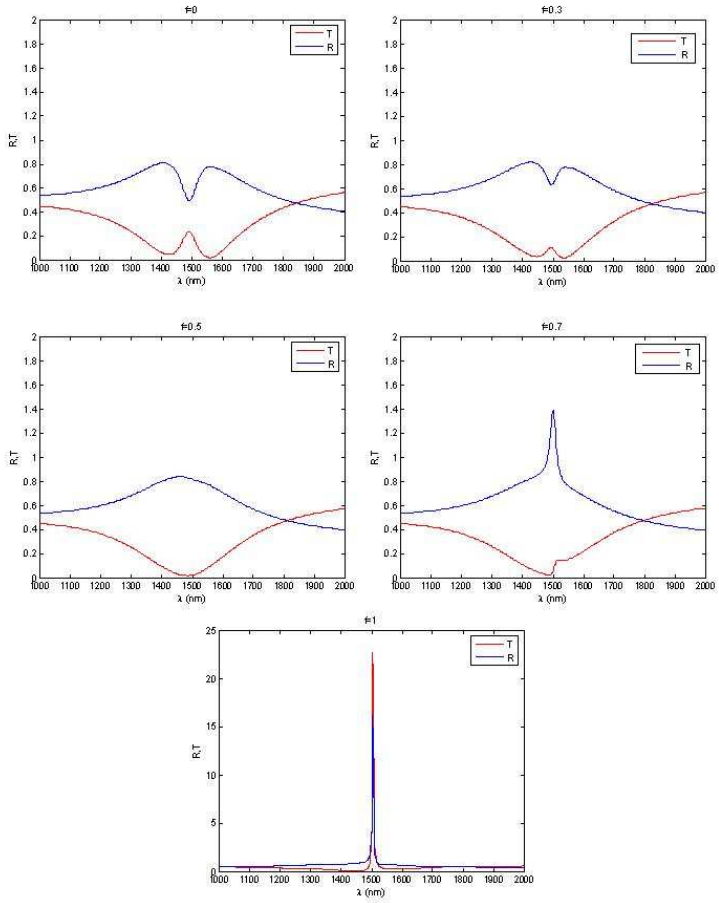

Figure 5.2: Intensity transmittance T, and reflectance R for a toy-model multilayer slab of thickness (l_{pl}+l_{InP}+l_{2LS}) as is shown in Fig. 5.1. The curves are the result with local field coupling $\mathcal{L}$. The two-level system occupation f increases from top to bottom as indicated. Parameters are: $\Omega_{2LS} = 2\pi \times 200THz$, $\Omega_{pl} = 2\pi \times 200THz$, $\gamma_{2LS} = 1510^{12}s^{-1}$, $\gamma_{pl} = 33.510^{12}s^{-1}$, $d_{2LS} = 6.510^{-29}Cm$, $d_{pl} = 10.310^{-26}\ Cm$, $N_{2LS} = 510^{24}m^{-3}$, $N_{pl} = 510^{20}m^{-3}$, $l_{2LS} = 50nm$, $l_{pl} = 30nm$, and $L = 1.732710^{10}m/F$ such that $V_{2LS} = 5.510^{11}s^{-1}$ and $V_{pl} = 5.510^{15}s^{-1}$ result.

$$P_{pl} = N_{pl} d_{pl} p_{pl} + c.c. = \epsilon_0 \chi_{2LS} \frac{\tilde{E}_0}{2} exp(-i\omega t) + c.c. \quad (5.11)$$

$$P_{2LS} = N_{2LS} d_{2LS} p_{2LS} + c.c. = \epsilon_{background} \chi_{2LS} \frac{\tilde{E}_0}{2} exp(-i\omega t) + c.c. \quad (5.12)$$

allows for obtaining all relevant optical properties of the system via a transfer matrix calculation of a multilayer system. Examples for calculated transmittance and reflectance spectra of a slab of thickness l of the resulting "material" embedded in vacuum (or air) are given in Fig. 5.2. Generally, the lineshape is Fano-like - an aspect that we have previously pointed out for coupled harmonic oscillators [103]. The Fano character becomes especially obvious for $f = 0$ and if one of the two resonances exhibits a much larger damping than the other one. More importantly, Fig. 5.2 also shows the evolution of the transmittance spectra for increasing two-level-system upper-state occupation (f=0, 0.25, 0.50, 0.75, and 1). Notably, the line width of the sharp transmittance maximum in Fig. 5.2 goes to zero as the transmittance peak approaches and eventually exceeds unity. At this point, the gain effectively compensates the loss. Hence, we interpret this feature as being indicative for the onset of lasing (or "spasing" [98] or "lasing spasing" [99]). Note that the transmittance shoots out of the frame in Fig. 5.2 and becomes $T = 25$ for $f = 1$. The threshold decreases as the local-field interaction increases (increased $\mathcal{L}$, hence increased V_{2LS} and V_{pl}) - as expected on the basis of the above intuitive reasoning in terms of the effective gain that matters.

Let us mention in passing that we have also performed microscopic numerical calculations (not shown) on the basis of the complete three-dimensional vector Maxwell equations similar to those in Ref. [99], however, with a frequency-dependent two-level-system gain resonance and for split-ring resonators roughly similar to the ones discussed in Ref. [35]. We find intensity transmittance and reflectance spectra that are qualitatively similar to the ones discussed here. In particular, we also find the avoided crossings and Fano-like lineshapes. In fact, our above choice of the phenomenological local-field parameter $\mathcal{L}$ (also see Fig. 5.2) is based on a comparison (or "fit") of the toy model to these numerical calculations.

In Fig. 5.2, we have intentionally only shown few selected aspects of the rather rich behavior of the model. Obviously, each of the two uncoupled resonances has four parameters (center frequency Ω , damping γ , dipole moment d, and density N). In addition, the important phenomenological local-field coupling parameter $\mathcal{L}$ and the two-level-system occupation f can be freely adjusted - altogether 10 parameters. Transmittance T, and reflectance R spectra of a multilayer material with geometry given by Fig. 5.1. So, it is useful understand the analogies between the classical system and the quantum system, in order to implement the FDTD numerical simulations (see appendix A). We developed this analogy in the next section.

5.5 Quantum analogy to the classical system

We can represent the gain medium as a Lorentz dispersive medium material, and the SRR as a bosonic medium.

5.5.1 The gain media: from the Lorentz dipole to the quantum system

We assume the permittivity of a Lorentz dispersive medium, with the resonance frequency Ω_{2LS}, as:

$$\epsilon = \epsilon_{background} + \chi = \epsilon_{background} + \frac{\epsilon_{lor}\Omega_{2LS}^2}{\Omega_{2LS}^2 - \omega^2 - 2i\gamma_{2LS}\omega} \tag{5.13}$$

where the sign of the Lorentz permittivity ϵ_{lor} gives us gain or absorbance if it is negative or positive, respectively. Due to we are in the near resonance regime, that is, the situation where $|\omega - \Omega_{2LS}| << \omega + \Omega_{2LS}$ we can make the classical analog of the rotating-wave approximation. Specifically we approximate $\Omega_{2LS}^2 - \omega^2$ by

$$\Omega_1^2 - \omega^2 \approx 2\omega(\Omega_{2LS} - \omega) \tag{5.14}$$

This reduces Eq (5.13) to

$$\epsilon = \epsilon_{background} + \frac{\epsilon_{lor}\frac{\Omega_{2LS}^2}{2\omega}}{\Omega_{2LS} - \omega - i\gamma_{2LS}} \tag{5.15}$$

That it is easy to make a comparison with the susceptibility in the model of two level systems when $V_{pl} = V_{2LS} = 0$ and $d_{pl} = 0$:

$$\chi_{2LS} = \frac{N_{2LS}d_{2LS}p_{2LS}}{\hbar\epsilon_0 E_0} = \frac{N_{2LS}d_{2LS}^2(1-2f)}{\hbar\epsilon_0[(\Omega_{2LS} - \omega) - i\gamma_{2LS}]} \tag{5.16}$$

From Eqs. (5.15) (5.16) we obtain:

$$(1 - 2f_1) = \frac{\hbar\epsilon_0\epsilon_{lor}\Omega_{2LS}}{2N_{2LS}d_{2LS}^2} \tag{5.17}$$

where we have used a rough approximation $\omega \approx \Omega_{2LS}$. From Eq. (5.17) we can observe that the module of the right handed term is in the range $[0, 1]$, i.e. if we fix ϵ_{lor} we have restrictions in the value of the dipole density N_{2LS}. Also we can see, that the factor wit the variables f and N_{2LS} $(1 - 2f)N_{2LS}$ must be both together in the equations about the linear response in the model. It is easy check that this last assumption is true.

5.5.2 The SRR: from the Lorentz dipole to the quantum system

If the electric field is parallel to the layers and is perpendicular to the arms of the SRR we can understand it as a LC resonator, the self-induction voltage of the inductance U_L plus the voltage drop over the capacitance U_C and due to the resistance U_R equals the voltage induced by the external electric field U_{ind}

$$L\dot{I} + RI + \frac{1}{C}\int Idt = U_{ind} = Es \tag{5.18}$$

Where s is the distance between the arms of the SRR. On the other hand, we have

$$P = \epsilon_0 \chi E \tag{5.19}$$

$$P/N_2 = Qs = s\int Idt \tag{5.20}$$

where we obtain using the previous equations in Eq. (5.18) and the ansatz $E = E_0 e^{i\omega t}$

$$\frac{\ddot{P}}{N_2} + \frac{R}{LN_2}\dot{P} + \frac{1}{LCN_2}P = -\frac{s^2 E}{L} \tag{5.21}$$

$$\left(-\omega^2 - i\frac{R}{L}\omega + \frac{1}{LC}\right)\chi = -\frac{N_{pl}s^2 t}{\mu_0 \epsilon_0 l^2} \tag{5.22}$$

where we have substituted

$$L = \mu_0 \frac{l^2}{t} \tag{5.23}$$

and the electrical susceptibility will be

$$\chi = \frac{N_{pl}c^2 s^2 t}{l^2} \frac{1}{\omega^2 + i\frac{R}{L}\omega - \frac{1}{LC}} \tag{5.24}$$

and using the rotating wave approximation (5.14), it must be

$$\chi = \frac{N_{pl}c^2 s^2 t}{2\omega l^2} \frac{1}{\omega - \frac{1}{\sqrt{LC}} + i\frac{R}{2L}} \tag{5.25}$$

From the model if we have not gain medium, i.e. $d_{2LS} = 0$

$$\chi = \frac{N_{pl} d_{pl}^2}{\hbar \epsilon_0} \frac{1}{\omega - \Omega_{pl} + i\gamma} \tag{5.26}$$

If we take into account that the damping constant in the model is

$$\gamma = \frac{\gamma_R}{2} = \frac{R}{2L} \tag{5.27}$$

Using Eqs. (5.24), (5.26) we obtain:

$$d_{pl} = \sqrt{\frac{\hbar \epsilon_0 c^2 s^2 t}{2\omega l^2}} \tag{5.28}$$

In the model, it is important to know that we are not including the magnetic response of the SRR and the plasmonic response of the metal. We can obtain an expression of this magnetic response in function of the fields from Eq. (5.18) and from

$$M = \chi_m H \tag{5.29}$$

$$M = N_{pl} l^2 I \tag{5.30}$$

We obtain that

$$I_0 = i \frac{s E_0}{L} \frac{1}{\Omega_{pl} - \omega - i\frac{R}{2L}} \tag{5.31}$$

where finally

$$\chi_m = N_{pl} l^2 i \frac{s E_0}{H_0 L} \frac{1}{\Omega_{pl} - \omega - i\frac{R}{2L}} \tag{5.32}$$

and the permeability will be

$$\mu(\omega) = 1 + \chi_m \tag{5.33}$$

So, the model is only valid for the calculation of the electric response of the SRR, in this precept we have decided that we must to fix the model with the dielectric constant obtain from the retrieval of the coefficients r and t and their phase for a SRR in air over an InP substrate.

5.6 Steady-state gain and occupation pinning

While any value of the 2LS occupation $f \in [0, 1]$ can occur under transient conditions, this is not true under steady-state conditions: If the coupled system exhibits a gain that exceeds the loss, stimulated emission will eventually reduce the two-level system upper-state occupation probability f until some steady-state value is reached -a phenomenon, which is well known as gain pinning in the context of a LASER [100, 104]. Thus, values of f above that steady-state value must be treated with carefully and knowing their meaning. Also see Ref. [27] for a corresponding discussion regarding constraints for negative-index metamaterials due to causality. Mathematically, polarization envelopes which neither grow ("too much gain") nor decay ("not enough gain") obviously need to have constant envelope, i.e., the imaginary part of the corresponding eigenfrequency of the coupled system has to be strictly zero. Without external light field, i.e., for $E = 0$ in (5.2) and (5.3), and for constant pump rate pump, the two complex-valued eigenfrequencies of the above coupled equations (5.2)-(5.6) are given by

$$\omega = \frac{\Omega_{2LS}+\Omega_{pl}}{2} - i\frac{\gamma_{2LS}+\gamma_{pl}}{2} \pm \sqrt{\left(\frac{\Omega_{2LS}-\Omega_{pl}}{2} - i\frac{\gamma_{2LS}-\gamma_{pl}}{2}\right)^2 + V_{2LS}V_{pl}(1-2f)}. \tag{5.34}$$

Zero imaginary part of (5.34) immediately translates into the general condition for the 2LS occupation f

$$\frac{\gamma_{2LS}+\gamma_{pl}}{2} = \pm\sqrt{\left(\frac{\Omega_{2LS}-\Omega_{pl}}{2} - i\frac{\gamma_{2LS}-\gamma_{pl}}{2}\right)^2 + V_{2LS}V_{pl}(1-2f)} \tag{5.35}$$

If (5.35) is fulfilled, the denominator of (5.7) becomes strictly zero for the real frequency ω resulting from (5.34), hence the linear optical response (5.11)-(5.12) diverges.

Case (a): Equation (5.34) has, e.g., a simple transparent special solution for the important degenerate case, i.e., for $\Omega_{2LS} = \Omega_{pl}$. We obtain

$$f = \frac{1}{2}\left(1 + \frac{\gamma_{pl}\gamma_{2LS}}{V_{pl}V_{2LS}}\right) = \frac{1}{2}\left(1 + \frac{\gamma^2}{V^2}\right) \in [0,1] \tag{5.36}$$

For example, for the parameters of Fig. 5.2, (5.36) leads to $f = 0.5831$. Recall that, according to the Pauli exclusion principle, the occupation f in (5.36) needs to be in the interval $[0,1]$. Thus, an effective coupling frequency V (= geometric mean of the two couplings) smaller than the effective damping γ(= geometric mean of the two dampings) leads to values of f exceeding unity. In other words: We have found a critical threshold value for the strength of the effective local-field interaction V. For values below that critical value, no lasing (spasing) action can occur under steady-state conditions. From (5.34), the (real-valued) lasing frequency results as $\omega = \Omega_{2LS} = \Omega_{pl}$. The condition of strong coupling $V \geq \gamma$ clearly also implies that an avoided crossing of the two-level-system resonance and the plasmonic resonance can be seen in the linear optical spectra without inversion, i.e., for $f = 0$ (see previous section). Hence, within our model, the avoided crossing can be viewed as a prerequisite for obtaining SPASER action.

Case (b): Another simple special case of (5.34) results for identical damping rates, i.e., for $\gamma = \gamma_{2LS} = \gamma_{pl}$, but finite detuning $\Delta\Omega = \Omega_{2LS} - \Omega_{pl} \neq 0$. We derive

$$f = \frac{1}{2}\left(1 + \frac{\gamma^2 + (\Delta\Omega/2)^2}{V^2}\right) \in [0,1]. \tag{5.37}$$

Clearly, increasing the detuning $\Delta\Omega$ increases the necessary 2LS occupation f, until eventually no physical solution $f \in [0,1]$ occurs any more for $\gamma^2 + (\Delta\Omega/2)^2 > V^2$. The detuning simply reduces the optical gain that is accessible for the plasmonic

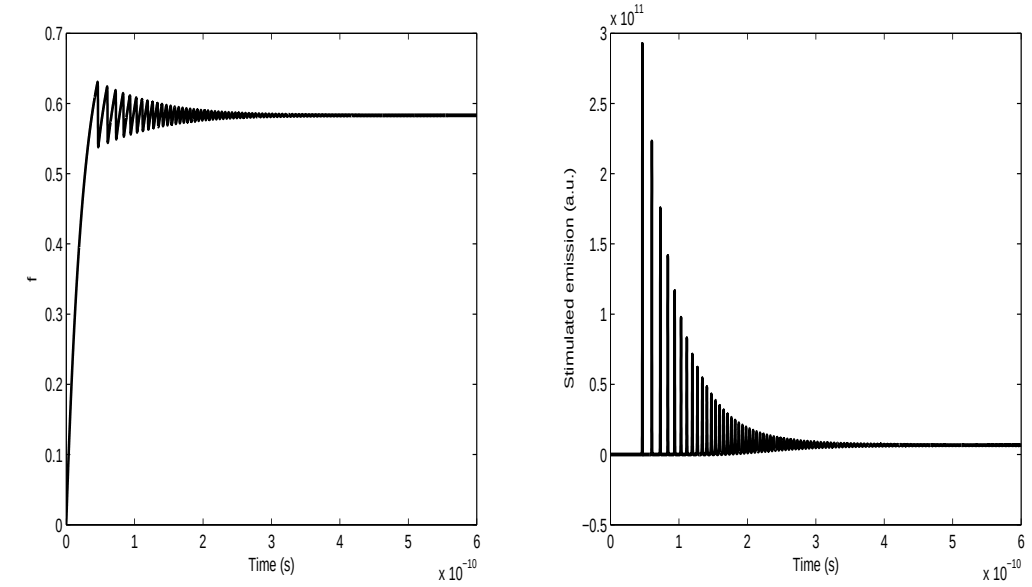

Figure 5.3: Switch-on of the lasing SPASER within our toy model leading to pronounced relaxation oscillations of the two-level system (a) occupation f and (b) the effective rate of stimulated emission Γ_{stim}. The pump rate $\Gamma_{pump} = \Gamma_0(1-f)$ with constant $\Gamma_0 = 3\Gamma_{2LS}$ after time $t = 0$ is parameter (as indicated). The model parameters are identical to those given in the caption of Fig. 5.2, $\Gamma_{2LS} = 10^{10}s^{-1}$. The lasing (spasing) frequency results as $\omega = \Omega_{2LS} = \Omega_{pl}$.

resonance from the two-level system (and so does the damping). From (5.34), the (real-valued) lasing frequency results as $\omega = (\Omega_{2LS} + \Omega_{pl})/2$. Note that, in the entire reasoning of this section, we have deliberately and tacitly neglected any optical feedback due to back-reflections from sample interfaces or even from mirrors (i.e., $E = 0$) because our aim has been to discuss the case of pure near-field optical feedback (the same holds for the following section). Experimentally, this ideal case could, in principle, be realized by appropriate anti-reflection coatings of the structure at the lasing wavelength. It should be clear, however, that there will be a continuous transition from an ideal SPASER to a usual LASER if the relative strength of the far-field optical feedback with respect to the near-field (local-field) optical feedback is increased continuously. Studying this transition is not subject of the present chapter.

5.7 Dynamics of the model

We introduce a pumping $\Gamma_{pump} = \Gamma_0(1-f)$ where Γ_0 is a constant. The Pauli blocking factor $(1-f)$ acknowledges that the upper state of each two-level system cannot be occupied with more than one electron, i.e., it guarantees $f \in [0,1]$. Γ_0 shall be zero until time $t = 0$. Then it is switched on to a constant value. Also, we seed the polarizations with a tiny but finite value. This is necessary because our toy model does not contain any spontaneous emission whatsoever. As a result, the transition amplitudes would otherwise be strictly zero, no matter how much gain the system develops. Alternatively, one could use a weak external seed pulse of light $E(t)$. None of these details is really important, the initial conditions just need to be non-zero. Then we have the dynamic differential equations using RWA and separating the real and imaginary part

$$\begin{aligned}
\frac{df}{dt} &= -\Gamma_{2LS} f + B(1-f) + 2\hbar^{-1} Im\{p_{pl}\} d_{2LS} E + \\
&+ 2V_{2LS} Im\{p_{2LS}\} Re\{p_{pl}\} - 2V_{2LS} Im\{p_{pl}\} Re\{p_{2LS}\} + \Gamma_0(1-f) \\
\frac{dRe\{p_{2LS}\}}{dt} &= -\gamma_{2LS} Re\{p_{2LS}\} - (\Omega_{2LS} - \omega) Im\{p_{2LS}\} - V_{2LS} Im\{p_{pl}\}(1-2f) \\
\frac{dIm\{p_{2LS}\}}{dt} &= -\gamma_{2LS} Im\{p_{2LS}\} - (\Omega_{2LS} - \omega) Re\{p_{2LS}\} + \\
&+ V_{2LS} Im\{p_{pl}\}(1-2f) + \hbar^{-1} d_{2LS} E(1-2f) \\
\frac{dRe\{p_{pl}\}}{dt} &= -\gamma_2 Re\{p_{pl}\} - V_{pl} Im\{p_{2LS}\} - (\Omega_{2LS} - \omega) Im\{p_{pl}\} \\
\frac{dIm\{p_{pl}\}}{dt} &= -\gamma_2 Im\{p_{pl}\} + V_{pl} Re\{p_{2LS}\} - (\Omega_{2LS} - \omega) Im\{p_{pl}\} + \hbar^{-1} d_{pl} E
\end{aligned}$$

We can write the first equation of the system as:

$$\frac{df}{dt} = -\Gamma_{2LS} - \Gamma_{stim} + \Gamma_{pump} \tag{5.38}$$

In the special case $E = 0$ and $\Omega_1 = \Omega_2 = \omega$, it easy to find the critical points $(d/dt = 0)$ where the differential are constants making the right handed terms of the previous equations equal to zero:

$$f_c = \frac{1}{2}\left(1 + \frac{\gamma_{2LS}\gamma_{pl}}{V_{2LS}V_{pl}}\right)$$

$$(abs(p_{2LS})_c)^2 = \frac{V_{2LS}\gamma_{pl}}{2V_{pl}}(\Gamma_0 - f_c(\Gamma_0 + \Gamma)$$

$$(abs(p_{pl})_c)^2 = \frac{V_{pl}}{2V_{2LS}\gamma_{pl}}(\Gamma_0 - f_c(\Gamma_0 + \Gamma)$$

In this way we obtain the stationary state in the dynamical model, we could appreciate several characteristics from these results. The first equation is the same result of Eq. (5.36).

The second and third equation give us an idea about the necessary pumping threshold for getting lasing due to:

$$abs(p_i)^2 > 0 \Rightarrow (\Gamma_0 - f_c(\Gamma_0 + \Gamma) > 0 \tag{5.39}$$

from where we have lasing for a pump Γ_0:

$$\Gamma_0 > \frac{f_c\Gamma}{1 - f_c} \tag{5.40}$$

In Fig. 5.3, we show selected time-dependent numerical solutions of the dynamical equations for parameters corresponding to those in the caption of Fig. 5.2. Trivially, the 2LS occupation f initially grows linearly in time due to the constant generation rate. At some point, the occupation is sufficiently large for obtaining gain. From this point in time on, the effective rate of stimulated emission Γ_{stim} increases exponentially. This growth ends when stimulated emission has depleted the gain so much that the system comes back to transparency (i.e., $\Gamma_{stim} \approx 0$). Population increases again and the gain recovers. Finally, after several oscillations with decreasing amplitude over hundreds of picoseconds, a steady-state value of f is reached - that does not depend on the pump rate Γ_{pump}. This aspect reflects the gain pinning already discussed in the previous section 5.6. The square modulus of the coupling polarizations (5.11)-(5.12) shows a behavior closely similar to that of the effective rate of stimulated emission in Fig. 5.3 (hence it is not depicted). The damped oscillation scenario is just the counterpart of the relaxation oscillations that are well known from the usual LASER rate equations [100, 104]. As usual, the relaxation oscillation frequency increases with increasing pump level. This observation emphasizes that our toy model and the usual LASER rate equations share certain similarities. Section 3, however, has also shown aspects that do not occur in the LASER rate equations at all.

5.8 Conclusions

In conclusion, we have presented a discussion and analysis of a simple and intuitive model for a (bosonic) metamaterial resonance coupled to a (fermionic) two-level-system gain resonance via local-field (evanescent-field) interactions. Especially the presented analytic solutions might help experimentalists in getting a feeling for designing actual SPASER structures. The model contains one purely phenomenological parameter $\mathcal{L}$ that describes the strength of the local-field interaction. This parameter needs to be chosen through comparison with numerical calculations of the plasmonic nanostructure via the three-dimensional vector Maxwell equations. The choice of all other model parameters for a given particular configuration is straightforward. Next, analytic results for steady-state gain/occupation pinning have been derived. Furthermore, we have presented numerical solutions for the time-dependent problem that exhibits the usual laser relaxation oscillations. The latter aspect shows that

our toy model for the SPASER shares similarities with the well established LASER rate equations. Broadly speaking, we have seen that one must not assume that gain can be added to a metamaterial just to reduce the losses and leave the metamaterial properties (e.g., magnetic permeability or negative refractive index) unaltered otherwise. Strong coupling to a gain resonance inherently and unavoidably changes the system, resulting in a new effective system with new effective properties that need to be evaluated.

Chapter 6

Negative and anomalous refraction of electrons in graphene

6.1 Motivation

There are several analogies between the physics of photons in optics and that of electrons in condensed matter theory. In particular, we have seen that photonic crystals come from the analogy with semiconductor physics of solid state theory. In this connection, we next apply our previous study of a 2-D PhC to a two dimensional system like graphene, which is a semimetal, likewise, we could apply these ideas to other mesoscopic systems like superconductors where the main physical properties take place in a plane. Hence, in this chapter we apply the technics developed earlier for PhC's with the aim of designing a device for electrons in graphene. First we analyze this kind of metamaterial, recently synthesized [105] as well as its properties which suggest graphene as a new goal in material physics and technology.

6.2 Introduction: Graphene a graphite monolayer

An allotropic compound of carbon is based on the sp^2 hybridization. In this kind of hybridization, the $2s$ atomic orbital mixes itself with two $2p$ orbitals generating three molecular orbitals σ situated in trigonal geometry. The generated structure is an hexagonal lattice called graphene. The remaining π orbital is perpendicular to the σ orbitals, and the electron of this π orbital is weakly bounded and can jump from orbital to orbital,his producing the electronic properties of this material at low energy.

Furthermore, graphene is the generatrix structure of other compounds. For example, the inclusion of 12 pentagons in the lattice of graphene produces a closed molecule: the fullerene or C_{60}. Other structures derived from the graphene are the nanotubes. A nanotube is a monolayer rolled itself forming a cylinder. Finally, the

graphite, the best known structure, is composed by several layers of graphene stratified one up another and attached to each other by Van der Walls forces.

Since its recent synthesis [105], graphene has proved to be a fruitful system in which ideas coming from several areas of physics successfully merge: soft condensed matter [106], *pseudorelativistic* quantum electrodynamics [107] and, more recently, optics [108] and *valleytronics* [109]. The concept of *valleytronics* [109] describes the use of the valley degeneracy in graphene as a degree of freedom to carrying information in the same way as the spin does in spintronics. In the scheme proposed in [109] the generation and detection of the valley polarized current is achieved by means of a quantum point contact in a graphene ribbon. The main difficulty in the experimental realization of this approach comes from the necessity of tailoring the graphene samples into nanoribbons and quantum point contacts with zigzag edges needed to support edge states. In this chapter we attempt to explain the concept of valleytronics and negative refraction in graphene and, finally, we propose an alternative mechanism for getting a different response from each valley using the effect of the trigonal warping [110] that can be tuned by a gate voltage in graphene samples of arbitrary shapes. Now, let us review the main properties of graphene for getting a better knowledge about this material.

6.3 Band structure of graphene and trigonal warping

As we have explained before, the sp^2 hybridization in the carbon atoms generates a hexagonal two-dimensional lattice, (see Fig. 6.1). The hexagonal structure can be understood as a superposition of two triangular sublattices interconnected, this one involves that the unit cell is not really a Bravais lattice and that the unit cell has two atoms from two sublattices separated a distance $a \approx 1.42\mathring{A}$. In the Fig. 6.1 the translation vectors are shown $\vec{a}_1$ and $\vec{a}_2$, while the vectors $\vec{\delta}_i$ for $i = 1, 2, 3$ represent the vectors to the first neighbors. The first neighbors of the atom of the other sublattice are simply $-\vec{\delta}_i$.

Now, we are going to calculate the band structure for the π orbitals using the tight binding approximation [111], at first neighbors, for a perfect and infinite sheet of graphene. In this approximation, an electron situated in a unit cell is described by the following wave function, by means of the Bloch theorem:

$$\Psi(\vec{K}, \vec{r}) = \frac{1}{\sqrt{N}} \sum_{m}^{A,B} \sum_{j_m}^{N} C_m e^{i\vec{K}\vec{R}_{j_m}} \phi_{A,B}(\vec{r} - \vec{R}_{j_m}) \equiv \sum_{m}^{A,B} C_m \Phi_m(\vec{K}, \vec{r}). \tag{6.1}$$

In the wave function (6.1), the index $m = A, B$ represents both sublattices respectively, the index j_m stands for every position $\vec{R}_{j_m}$ of the atoms of one sublattice m in the whole crystal and $\phi_{A,B}(\vec{r})$ is the normalized orbital wave function p in each atom.

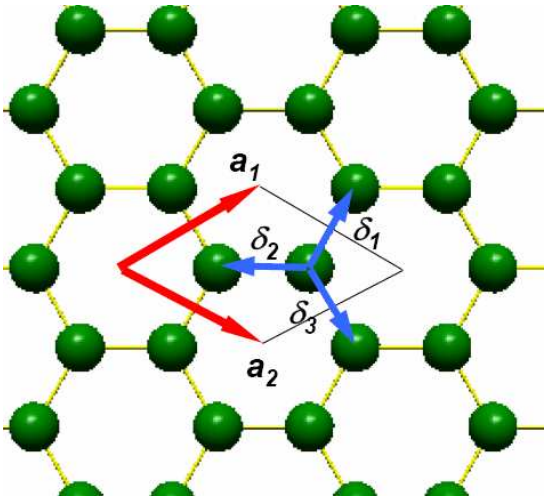

Figure 6.1: Hexagonal structure of graphene. The lattice vectors are $\vec{a}_1 = \sqrt{3}a\left(\frac{3}{2}, \frac{\sqrt{3}}{2}\right)$ and $\vec{a}_2 = \sqrt{3}a\left(\frac{3}{2}, \frac{-\sqrt{3}}{2}\right)$.

the vector $\vec{K}$ is typically quantized in units of $\frac{2\pi}{Na}$. If we know the arrangement of the carbon atoms in the hexagonal lattice and the atomic wave functions for the p orbitals, the problem consists of calculating the coefficients C_m such a way that the wave function (6.1) is an eigenstate of the hamiltonian

$$H(\vec{r}) = -\frac{1}{2m_e}\nabla^2 + V(\vec{r}), \tag{6.2}$$

with the property of periodicity V, $V(\vec{r}) = V(\vec{r} - \vec{R}_j)$:

$$H(\vec{r})\Psi(\vec{K}, \vec{r}) = E(\vec{k})\Psi(\vec{K}, \vec{r}). \tag{6.3}$$

Multiplying Eq. (6.3)by $\Psi^*(\vec{K}, \vec{r})$ and integrating in $\vec{r}$, we have that

$$\sum_{j_m, i_n}^{N} \sum_{n,m}^{A,B} \frac{1}{N} C_n^* C_m e^{i\vec{K}(\vec{R}_{j_m} - \vec{R}_{i_n})} \int d^2\vec{r}\phi^*(\vec{r} - \vec{R}_{i_n}) H(\vec{r}) \phi(\vec{r} - \vec{R}_{j_m}) =$$
$$= E \sum_{j_m, i_n}^{N} \sum_{n,m}^{A,B} \frac{1}{N} C_n^* C_m e^{i\vec{K}(\vec{R}_{j_m} - \vec{R}_{i_n})} \int d^2\vec{r}\phi^*(\vec{r} - \vec{R}_{i_n}) \phi(\vec{r} - \vec{R}_{j_m}). \tag{6.4}$$

At this point, we assume the approximation in which the integral of the right hand in (6.4) is non zero only when $i_n = j_m$ (weak binding between states from different sublattices), so we can write

$$\frac{E}{N} \sum_{j_m, i_n}^{N} \sum_{n,m}^{A,B} e^{i\vec{K}(\vec{R}_{j_m} - \vec{R}_{i_n})} C_n^* C_m \delta_{j_m, i_n} \delta_{nm} = E \sum_{m}^{A,B} C_m^* C_m. \tag{6.5}$$

If we now pay attention to the right hand term of Eq. (6.4), we must take into account that the translation vectors of both sublattices are related to each other, for $i = j$, by

$$\vec{R}_{j_A} - \vec{R}_{j_B} = -\vec{\delta}_2. \tag{6.6}$$

The tight binding approximation at first neighbors involves that the integral

$$\int d^2\vec{r}\phi^*(\vec{r} - \vec{R}_{i_n})H\phi(\vec{r} - \vec{R}_{j_m}) = \int d^2\vec{r}\phi^*(\vec{r})H\phi(\vec{r} - (\vec{R}_{j_m} - \vec{R}_{i_n})) \tag{6.7}$$

will be different from zero in two cases. The first case corresponds to the situation in which $\vec{R}_{j_m} = \vec{R}_{i_n}$, reducing the integral (6.7) to $\epsilon_0 \equiv \int d^2\vec{r}\phi^*(\vec{r})H\phi(\vec{r})$.The left hand term of (6.7) will be expressed by $\epsilon_0 \sum_m^{A,B} C_m^* C_m$.

The second contribution, ascribed to consider first neighbors, $n \neq m$, will have a phase in terms of the vectors $\vec{R}_{i_n}$ from the same base, using the relation (6.6), as

$$\vec{R}_{j_m} - \vec{R}_{i_n} = \vec{R}_{j_m} - \vec{R}_{i_m} - \vec{\delta}_2. \tag{6.8}$$

Both sums being in the same base, and due to the invariance of the wave functions under translations of any vector of the real lattice, we obtain

$$\begin{aligned}\sum_{n\neq m}^{A,B} \frac{1}{N} C_n^* C_m \sum_{j_m,i_m}^{N} e^{i\vec{K}(\vec{R}_{j_m} - \vec{R}_{i_m} - \vec{\delta}_2)} \int d^2\vec{r}\phi^*(\vec{r})H(\vec{r})\phi(\vec{r} - (\vec{R}_{j_m} - \vec{R}_{i_m} - \vec{\delta}_2)) = \\ = \sum_{n\neq m}^{A,B} \frac{1}{N} C_n^* C_m N \sum_{j,i}^{2} e^{i\vec{K}(\vec{a}_i - \vec{a}_j - \vec{\delta}_2)} \int d^2\vec{r}\phi^*(\vec{r})H(\vec{r})\phi(\vec{r} - (\vec{a}_i - \vec{a}_j - \delta_2)).\end{aligned} \tag{6.9}$$

It is sufficient to calculate $\vec{a}_i - \vec{a}_j - \vec{\delta}_2$ for $i, j = 1, 2$, being the result of the possible combinations for i and j of the three vectors $-\vec{\delta}_i$ for $i = 1, 2, 3$. Since the integral $\int d^2\vec{r}\phi^*(\vec{r})H(\vec{r})\phi(\vec{r} - \vec{\delta}_i)$ for $i = 1, 2, 3$ is not dependent on the vector $\vec{\delta}$, we define the *jump* t as $t \equiv \int d^2\vec{r}\phi^*(\vec{r})H(\vec{r})\phi(\vec{r} - \vec{\delta}_i)$ for $i = 1, 2, 3$ ($t \sim 2.8$eV). Finally, the corresponding term in the left hand side of Eq. (6.4) results in:

$$t \sum_{n\neq m}^{A,B} C_n^* C_m \sum_j e^{-i\vec{K}\vec{\delta}_j} \equiv t \sum_{n\neq m}^{A,B} C_n^* C_m f(\vec{K}). \tag{6.10}$$

Joining all the parts of the equation, we can write Eq. (6.4) in form of a matrix equation:

$$\begin{pmatrix} \epsilon_0 & tf(\vec{K}) \\ tf^*(\vec{K}) & \epsilon_0 \end{pmatrix} \begin{pmatrix} C_1 \\ C_2 \end{pmatrix} = E(\vec{k}) \begin{pmatrix} C_1 \\ C_2 \end{pmatrix}. \tag{6.11}$$

The bands being represented by the eigenstates of the eigenvalue equation (6.11), which using the explicit values of the vectors $\vec{\delta}_j$ are

$$E(\vec{k}) = \epsilon_0 \pm t\sqrt{1 + 4\cos\left(\frac{3ak_x}{2}\right)\cos\left(\frac{\sqrt{3}ak_y}{2}\right) + 4\cos^2\left(\frac{\sqrt{3}ak_y}{2}\right)}. \tag{6.12}$$

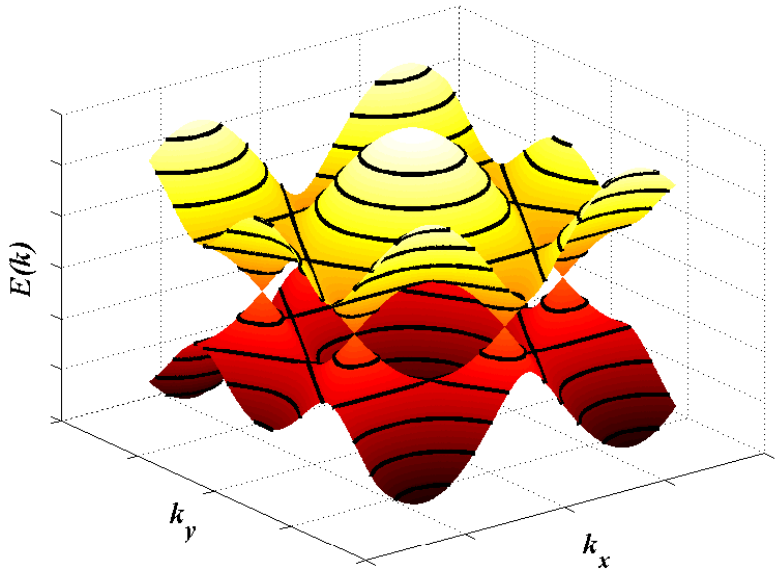

Figure 6.2: Band structure π in graphene.

The band structure is shown in Fig. 6.2. Actually, the parameter ϵ_0 can be eliminated defining the origin of energies in the Eq. (6.11). The Brillouin zone in graphene turn out to be hexagonal, those could be known by the reciprocal lattice vectors, $\vec{b}_1 = \frac{2\pi}{3a}\left(1, \sqrt{3}\right)$ and $\vec{b}_{-1} = \frac{2\pi}{3a}\left(1, -\sqrt{3}\right)$. In Fig. 6.3, the valence and condition bands, represented by the solutions $E(\vec{k}) < 0$ and $E(\vec{k}) > 0$ respectively,are touching in six points, the corners of the Brillouin zone. By periodicity of the reciprocal lattice, the number of independent points is reduced to two: $\vec{K}_1 = \frac{1}{a}\left(0, \frac{4\pi}{3}\right)$ and $\vec{K}_{-1} = \frac{1}{a}\left(0, -\frac{4\pi}{3}\right)$. Both points, in which the bands are touching are called Dirac points. Furthermore, the carbon atom gives an electron to the $2p$ orbital to the bands, and then we have that the valence band is fully filled and the conduction band is empty, being the Fermi level, in the neutral material, in the Dirac points, and the electronics excitations at low energy near of those points.

6.4 Dirac Hamiltonian

If the energy excitation is low we have a wavevector near one of these points, and the Hamiltonian at low energy can be obtained by developing around these Dirac points $\vec{K}_{1,-1}$ in Eq. (6.11). Since we have two Dirac points, we will have two states

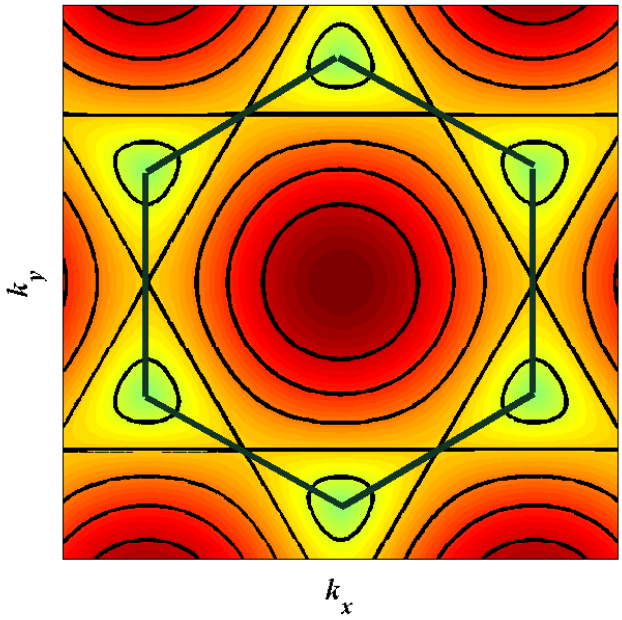

Figure 6.3: Band structure π in graphene. The hexagonal Brillouin zone is overprinted.

at low energy, depending on the environment of the two point in which we are:

$$H = t \begin{pmatrix} 0 & f(\vec{K}) \\ f^*(\vec{K}) & 0 \end{pmatrix} \simeq v_F \begin{pmatrix} 0 & sk_x - ik_y \\ sk_x + ik_y & 0 \end{pmatrix} + O(k^2), \tag{6.13}$$

where the parameter $s\pm1$ gives us information of which Dirac point we are developing, and $v_F = \frac{3ta}{2}$ is a parameter with velocity dimensions, which is approximately $v_F \sim 10^6 m/s$, called Fermi velocity. We can write Eq. (6.13) more compactly by defining fourdimensional matrices $\boldsymbol{\gamma}$ from Pauli matrices $\boldsymbol{\sigma}$ y $\boldsymbol{\tau}$:

$$\gamma^1 = \tau_3 \otimes \sigma^1, \qquad \gamma^2 = \mathbf{1} \otimes \sigma^2, \tag{6.14}$$

The hamiltonian

$$H = v_F \boldsymbol{\gamma} \vec{k}, \tag{6.15}$$

being the Dirac Hamiltonian in two dimensions. We thus reach the following conclusion: the electronic states at low energy in the π bands are those that satisfy the massless Dirac equation, acting the sublattice structure as a degree of freedom for the spin. It is very common in graphene literature that this degree of freedom be called *pseudospin* or *spin AB*, referencing the structure of sublattice in the hexagonal lattice.

6.5 Klein paradox and chirality

The Klein paradox refers to a counterintuitive relativistic process in which an incoming electron starts penetrating through a potential barrier if its height, V_0, exceeds the electron rest energy, mc^2 (where m is the electron mass and c is the speed of light). In this case, the transmission probability, T, only weakly depends on the barrier height, approaching the perfect transparency for very high barriers, in contrast to the conventional, non-relativistic tunneling where T exponentially decays with increasing V_0. This relativistic effect can be attributed to the fact that a sufficiently strong potential, being repulsive for electrons, is attractive for positrons and results in positron states inside the barrier, which align in energy with the electron continuum outside. Matching between electron and positron wavefunctions across the barrier leads to the high-probability tunneling described by the Klein paradox. The essential feature of quantum electrodynamics (QED) responsible for the effect is the fact that states at positive and negative energies (electrons and positrons) are intimately linked (conjugated), being described by different components of the same spinor wavefunction. This fundamental property of the Dirac equation is often referred to as the charge-conjugation symmetry. Although Klein's gedanken experiment is now well understood, the notion of paradox is still widely used, perhaps because the effect has never been experimentally observed. Katnelson et al. [107] show that graphene provides an effective medium ("vacuum") where relativistic quantum tunneling described by the Klein paradox and other relevant QED phenomena can be tested experimentally.

The fact that charge carriers in graphene are described by the Dirac-like Eq. (6.15) involves that quasiparticles in graphene exhibit the linear dispersion relation $E = \hbar k v_F$, as if they were massless relativistic particles (for example, photons) but the role of the speed of light is played here by the Fermi velocity $v_F \approx c/300$.

Above zero energy, the current carrying states in graphene are, as usual, electron-like and negatively charged. At negative energies, if the valence band is not full, its unoccupied electronic states behave as positively charged quasiparticles (holes), which are often viewed as a condensedmatter equivalent of positrons. Note however that electrons and holes in condensed matter physics are normally described by separate Schrödinger equations, which are in no way connected. By contrast, electron and hole states in graphene are interconnected, exhibiting properties analogous to the charge-conjugation symmetry in QED. For the case of graphene, the latter symmetry is a consequence of its crystal symmetry because graphene quasiparticles have to be described by two-component wavefunctions, needed to define relative contributions of sublattices A and B in quasiparticles make-up. The two-component description for graphene is very similar to the one by spinor wavefunctions in QED but the "spin" index for graphene indicates sublattices rather than the real spin of electrons and is usually referred to as pseudospin σ.

The conical spectrum of graphene is the result of intersection of the energy bands

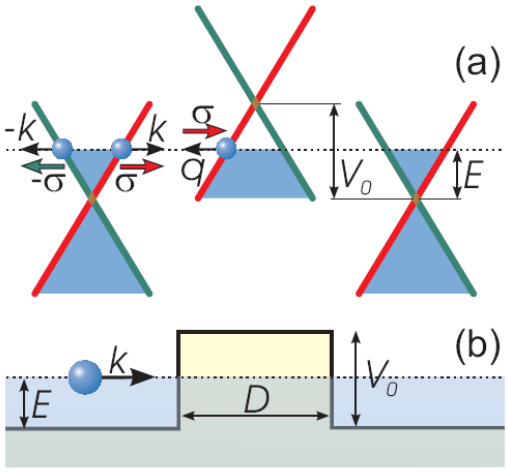

Figure 6.4: Tunnelling through a potential barrier in graphene. (a)- Schematic diagrams of the spectrum of quasiparticles in single-layer graphene. The spectrum is linear at low Fermi energies ($< 0.6eV$). The red and green curves emphasize the origin of the linear spectrum, which is the crossing between the energy bands associated with crystal sublattices A and B. The three diagrams schematically illustrate the positions of the Fermi energy E across the potential barrier of height V_0 and width D shown in (b). The Fermi level (dotted lines) lies in the conduction band outside the barrier and the valence band inside it. The blue filling indicates occupied states. The pseudospin denoted by vector σ is parallel (antiparallel) to the direction of motion of electrons (holes), which also means that σ keeps a fixed direction along the red and green branches of the electronic spectrum (After Ref. [107]).

originating from sublattices A and B (see Fig. 6.2) and, accordingly, an electron with energy E propagating in the positive direction originates from the same branch of the electronic spectrum (shown in red) as the hole with energy -E propagating in the opposite direction. This yields that electrons and holes belonging to the same branch have pseudospin σ pointing in the same direction, which is parallel to the momentum for electrons and antiparallel for holes (see Fig. 6.4 (a)). This allows one to introduce chirality, which is formally a projection of pseudospin on the direction of motion, which is positive and negative for electrons and holes, respectively. The term chirality is often used to refer the additional built-in symmetry between electron and hole parts of graphene spectrum (as indicated by color in Fig. 6.4).

Because quasiparticles in graphene accurately mimic Dirac fermions in QED, this condensed matter system makes it possible to set up a tunneling experiment similar to that analyzed by Klein. The general scheme of such an experiment is shown in Fig. 6.4, where we consider the potential barrier that has a rectangular shape and is

infinite along the y-axis:

$$V(x) = \begin{cases} V_0 & \text{if} \quad 0 < x < D \\ 0 & \text{if} \quad otherwise \end{cases} \tag{6.16}$$

This local potential barrier inverts charge carriers underneath it, creating holes playing the role of positrons, or vice versa. It is straightforward to solve the tunneling problem sketched in Fig. 6.4(b). We assume that the incident electron wave propagates at an angle ϕ with respect to the x axis and then try the components of the Dirac spinor ψ_1 and ψ_2 for the Hamiltonian $H = H_0 + V(x)$ in the following form:

$$\psi_1(x,y) = \begin{cases} \left(e^{ik_x x} + re^{-ik_x x}\right) e^{ik_y y} & \text{if} \quad x < 0 \\ \left(ae^{iq_x x} + be^{-iq_x x}\right) e^{ik_y y} & \text{if} \quad 0 < x < D \\ te^{ik_x x + ik_y y} & \text{if} \quad x > D \end{cases} \tag{6.17}$$

$$\psi_2(x,y) = \begin{cases} s\left(e^{ik_x x + i\phi} - re^{-ik_x x - i\phi}\right) e^{ik_y y} & \text{if} \quad x < 0 \\ s'\left(ae^{iq_x x + i\theta} - be^{-iq_x x - i\theta}\right) e^{ik_y y} & \text{if} \quad 0 < x < D \\ ste^{ik_x x + ik_y y + i\phi} & \text{if} \quad x > D \end{cases} \tag{6.18}$$

where $k_F = 2\pi/\lambda$ is the Fermi wavevector, $k_x = k_F \cos\phi$ and $k_y = k_F \sin\phi$ are the wavevector components outside the barrier, $q_x = \sqrt{(E - V_0)^2/(\hbar^2 v_F^2) - k_y^2}$, $\theta = \arctan(k_y/q_x)$ is the refraction angle, $s = sgnE$ and $s' = sgn(E - V_0)$. Requiring the continuity of the wavefunction by matching up coefficients a, b, t, r, we find the following expression for the reflection coefficient r:

$$r = 2e^{i\phi} \sin(q_x D) \frac{\sin\phi - ss' \sin\theta}{ss'[e^{-iq_x D}\cos(\phi + \theta) + e^{iq_x D}\cos(\phi - \theta)] - 2i\sin(q_x D)} \tag{6.19}$$

Equations yield that under resonance conditions $q_x D = N, N = 0, \pm 1, ...$ the barrier becomes transparent ($T = 1$). More significantly, however, the barrier remains always perfectly transparent for angles close to normal incidence $\phi = 0$. The latter is the feature unique to massless Dirac fermions and directly related to the Klein paradox in QED. One can understand this perfect tunneling in terms of the conservation of pseudospin σ. Due to the isospin conservation, electrostatic potential cannot scatter chiral fermions in backward direction.

6.6 Negative refraction and valleytronics

It is easy to see [108] from the previous section that the Fermi surface and the dispersion relation at low energies can be used to focuses electron beams. If we consider a p-n junction at low energies we can see from Fig. 6.5 that one electron in the conduction band with energy E_i, wavevector $\vec{k_i} = |E_i|(\cos\theta_i, \sin\theta_i)$, and group

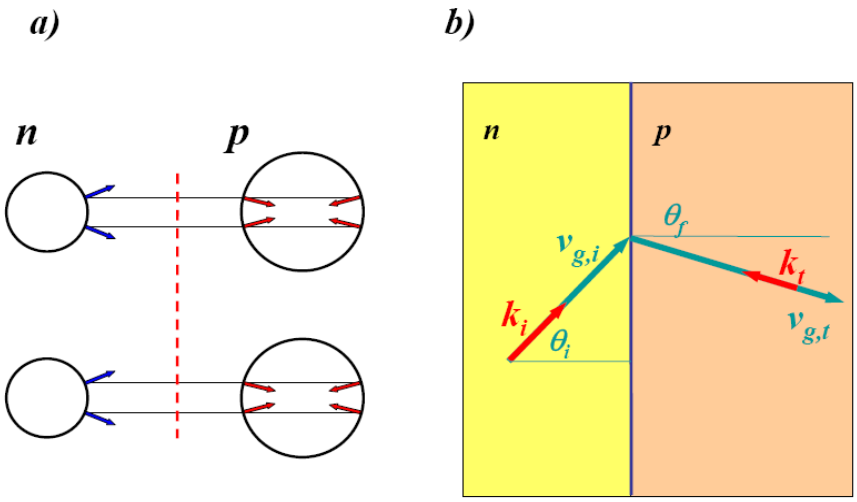

Figure 6.5: (a) Conservation on the parallel component of the moment. Both cones in the Dirac regime giving the same transmitted wavevector. (b) Cinematics of the transmission.

velocity $\vec{v}_{g,i} = v_F(\cos\theta_i, \sin\theta_i)$ goes through the barrier to a valence band state with energy $E_t = E_i - V_0 = -v_F\left|\vec{k}_t\right|$. By conservation of the parallel component of the wavevector to the barrier, The possible values of the transmission angle are θ_t and $\theta'_t = \pi - \theta_t$, with $\cos\theta_t = \cos\theta'_t$ but $\sin\theta'_t = -\sin\theta_t$ (Fig. 6.5,a). Necessarily, the group velocity must point towards the p zone of the barrier, this involves that θ_t be in the second quadrant and $|E_i|\sin\theta_i = -|E_f|\sin\theta_f$. Take into account that this equation is independent of the valley (6.5.(a)).

Focusing of electrons by a sharp p-n junction in graphene can be used to turn the n-p-n junction into a Veselago lens for electrons. In such a device (Fig. 6.6), the density of charge carriers in the p-region (of width D) can be controlled by the top gate. Fig. 6.6 illustrates another graphene-based device in which a prism-shaped top-gate (a triangular shape to the p region in the n-p-n junction) may be used as a focusing beam splitter. For example, electrons emitted from contact B (Fig. 6.6 B) are distributed between the contacts b and β, whereas the signal sent from contact A (Fig. 6.6 C) is replicated into the pair of contacts a and α.

On the other hand, Rycerz, Tworzyd*l*o and Beenakker [109] suggest that the independence and degeneracy of the valley degree of freedom might be used to control an electronic device, in much the same way as the electron spin is used in spintronics or quantum computing. A key ingredient for *valleytronics* would be a controllable way of occupying a single valley in graphene, thereby producing a valley polarization. A

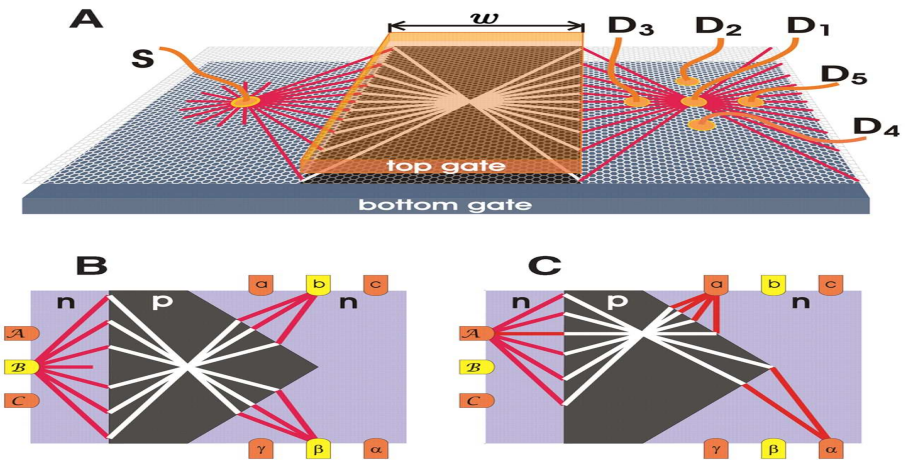

Figure 6.6: **A** Electron Veselago lens and (**B** and **C**) prism-shaped focusing beam splitter in the ballistic n-p-n junction in graphene-based transistor (after Ref. [108]).

device was suggested based on a point contact junction with among graphene ribbons with special termination (zigzag edges) Fig. 6.7.

Both previous proposals require a quite precise tailoring of the graphene samples which hardens their experimental realization. In our work we combine the two former ideas and propose a very simple way to construct a beam splitter where each of the electronic beams is fully polarized in the valley quantum number. In what follows we will describe the mechanism based on an n-p-n junction in detail and show how it can be tested in an optical device. As we will see, the present mechanism allows to obtain fully polarized currents in graphene samples of arbitrary shapes.

6.7 Trigonal warping: Energy and group velocity

Up to now, in this chapter and in the literature, most of the excitement on graphene has been centered around the very low energy region where the dispersion is linear and the elementary excitations are described by massless Dirac spinors, a relativistic description for a condensed matter system [112]. We will notice however that at intermediate energies of the order of $0.6 - 0.7eV$ easily accessible with a gate voltage, the constant energy curves acquire a non-trivial distortion [110], trigonal warping (TW), which is different in the two valleys (Fig. 6.8).

We can obtain the dispersion relation writing again the hamiltonian by means of a tight binding approximation for the graphene π electrons, including both valleys:

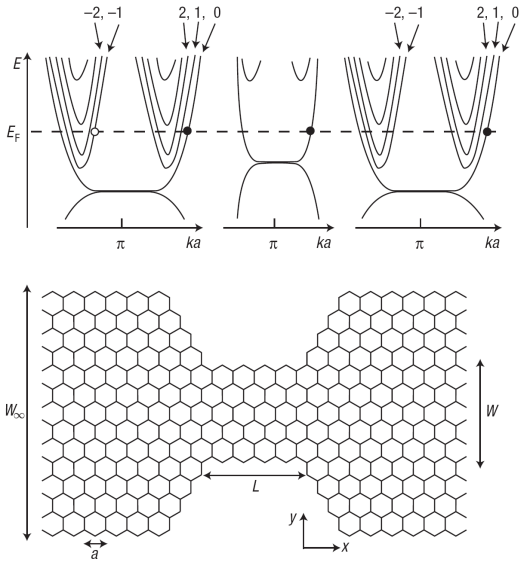

Figure 6.7: Schematic diagram of the valley filter from [109]. Middle panel: Honeycomb lattice of carbon atoms in a strip containing a constriction with zigzag edges. Top panel: Dispersion relation in the wide and narrow regions. An electron in the first valley (modes n=0,1,2,...) is transmitted (filled circle), whereas an electron in the second valley (modes n=-1,-2,...) is reflected (open circle). The polarity of the valley filter switches when the potential height in the constriction crosses the Fermi energy, E_F.(After Ref. [109])

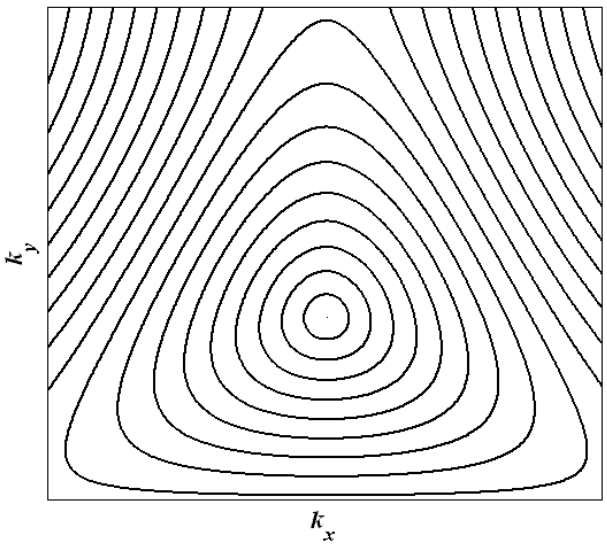

Figure 6.8: Contour lines of the dispersion relation around the Dirac point K. The contour lines around the other Dirac point, K', can be obtained making a specular reflection over the k_x axis.

$$H(\vec{k}) = \begin{pmatrix} 0 & \phi_K(\vec{k}) & 0 & 0 \\ \phi_K^*(\vec{k}) & 0 & 0 & 0 \\ 0 & 0 & 0 & \phi_{K'}(\vec{k}) \\ 0 & 0 & \phi_{K'}^*(\vec{k}) & 0 \end{pmatrix},$$

being $\phi(\vec{k}) = -t\left(e^{ik_x a} + e^{-\frac{i}{2}k_x}\cos(\frac{\sqrt{3}}{2}k_y a)\right)$. Now, we are going to develop around both Dirac points by means of small moments ϕ, and we are going to maintain the two first terms:

$$H(\vec{k}) \simeq \quad v_F \begin{pmatrix} 0 & k_x - ik_y & 0 & 0 \\ k_x + ik_y & 0 & 0 & 0 \\ 0 & 0 & & -k_x - ik_y \\ 0 & 0 & -k_x + ik_y & 0 \end{pmatrix} - \\ -\frac{v_F a}{4} \begin{pmatrix} 0 & (k_x + ik_y)^2 & 0 & 0 \\ (k_x - ik_y)^2 & 0 & 0 & 0 \\ 0 & 0 & & (k_x - ik_y)^2 \\ 0 & 0 & (k_x + ik_y)^2 & 0 \end{pmatrix} \quad (6.20)$$

The first term is the one corresponding to Dirac, and the second term is about TW.

Hence, in the tight-binding approximation of the low energy band structure for graphene, the dispersion relation including both the Dirac and the TW terms, is:

$$E_s(\vec{k}) = \pm\hbar v_F \sqrt{k^2 + \frac{a^2}{16}k^4 + \frac{a}{2}s\left(k_x^3 - 3k_x k_y^2\right)}, \tag{6.21}$$

where v_F is the Fermi velocity, a is the lattice constant and the short notation $k^2 = k_x^2 + k_y^2$ is used. The parameter $s = \pm 1$ refers to the two valleys.

The average current moving trough the sample is $\langle \vec{J}_s \rangle = \frac{e}{\hbar}|t_s|^2 \vec{v}_{g,s}$,where t_s represents the transmission coefficient and $\vec{v}_{g,s}$ stands for the group velocity in each valley. When the TW term is considered, $\vec{v}_{g,s}$ has the form

$$\vec{v}_{g,s} = \frac{1}{\hbar}\nabla_{\vec{k}} E_s(\vec{k}) = \pm\frac{v_F^2}{2E_s(\vec{k})}\left((2 + \frac{a^2}{4}k^2)\vec{k} + \frac{a}{2}s\vec{F}\right), \tag{6.22}$$

where $\vec{F} = (3k_x^2 - 3k_y^2, -6k_x k_y)$. When TW is considered, $|t_s|^2$ does not essentially differ from that obtained when only the linear term is considered in the whole $p-n$ junction [107, 113], having almost the same shape for both valleys. The major role in the different behavior of $\langle \vec{J}_s \rangle$ for each valley is played by the group velocity $\vec{v}_{g,s}$, since it explicitly depends on s. The main idea relies on the fact that at energies where the trigonal warping is noticeable, the Fermi surfaces around each valley are different and anisotropic. This allows us to suggest a device based on a p-n junction where the response is valley asymmetric. (Figs. 6.9 and 6.10).

In Fig. 6.9 we show a field effect $n - p^+$ device in graphene. In the p^+ area, the applied gate voltage is such that the chemical potential is located at energies where the TW effect becomes relevant (according to ARPES data [114] this happens for energies of $0.6 - 0.7eV$). When the TW term is considered, the band is no longer isotropic around each K point. We have then to care about the relative orientation between the lattice and the deposited gate. Due to the symmetry of the honeycomb lattice, all the possible orientations lie between the two limiting cases shown in Figs. 6.9(a),(b). Fig. 6.9(c) shows the direction of $\vec{v}_{g,s}$ determined by conservation of the momentum parallel to the potential barrier interfaces when the boundary is parallel to the zigzag orientation. Due to the s dependence of $\vec{v}_{g,s}$ the currents associated to each valley travel in different directions leading to two different currents polarized in the valley index. Fig. 6.9(d) represents the parallel momentum conservation when the gate is oriented along the armchair direction. The current associated to one of the valleys (valley K) is fully collimated because, by momentum conservation, the accessible area of the energy surface is almost plane. The current belonging to the other valley is more dispersed because the accessible area has a higher curvature.

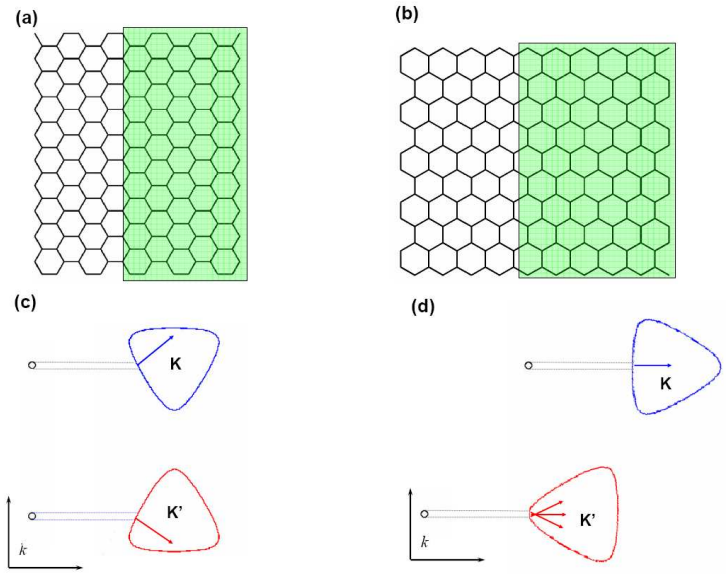

Figure 6.9: The two limiting cases for the deposition of the gate over the graphene sample. The green area denotes the region doped with holes at energies where the TW becomes relevant. (a) Interface of the gate parallel to the zigzag orientation and (b) the armchair interface. (c) and (d) represent the corresponding isofrequency lines showing the conservation of the parallel wavevector for the zigzag and armchair interface, respectively. We obtain two directions of refraction for the zigzag orientation parallel to the interface depending on whether the chosen valley is K or K'. For the armchair interface, a forward direction of refraction appears due to the little dispersion produced by the second valley.

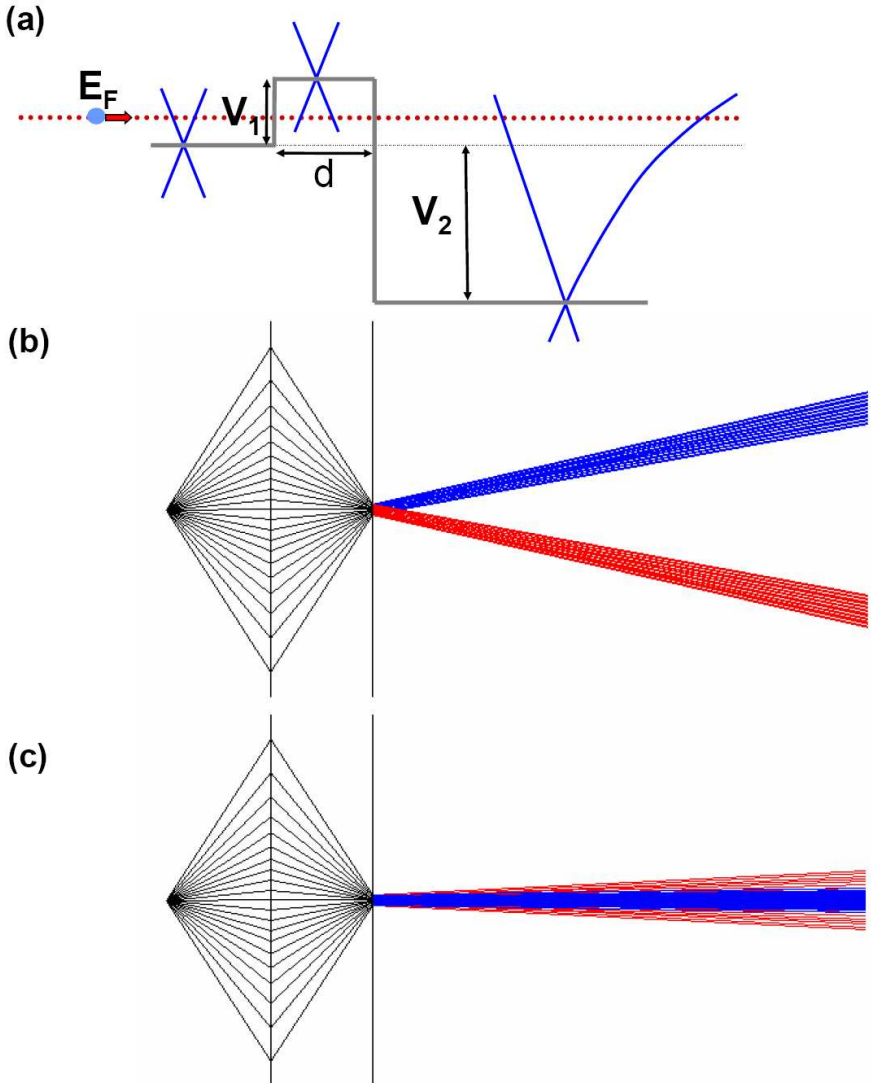

Figure 6.10: (a) Potential profile of a $n-p-n^-$ junction and schematic band structure of one valley. (b) Theoretical ray tracing of the beams coming from a point source in a junction with the interface parallel to the zigzag orientation. $E_F = 0.05eV$, $V_1 = 0.10eV$ and $V_2 = -1.5eV$. The beam splitting is noticeable. (c) Armchair junction. We now obtain a collimation perpendicular to the interface.

6.8 Beam splitter, collimator and valley polarization

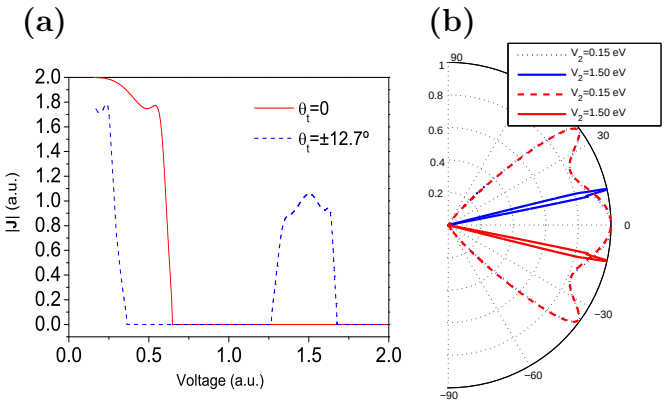

Figure 6.11: (a) Current versus Voltage for two transmission angle θ_t of observation. (b)Transmission probability for the K (blue lines) and K'(red lines) as a function of the output angle θ_t for different negative potentials V_2. The parameters are: barrier width: $d = 100nm$, initial energy: $E_F = 0.05eV$, initial potential: $V_1 = 0.14eV$.

With these characteristics, we can design a device to achieve the realization of a beam splitter with an $n - p - n^-$ junction (Fig. 6.10(a)) with the interface parallel to the zigzag orientation. In the first zone, we introduce an electron source. In this region, the Fermi level E_F is at low energy in the conduction band, where the Fermi surface is circular and the linear Dirac regime is valid. This area is separated from a zone of low chemical potential (p-region) in the valence band, by a barrier with a potential V_1 . In the interface we have both negative refraction and focusing [108]. The last step with negative potential V_2 is placed immediately before the electron focusing in order to get a very small illuminated zone. In this way, we have narrower exit beams avoiding the formation of caustics which would appear if the position of the focus were reached before the last interface. Finally, the last region is at high voltages in the conduction band (n^--region) i.e. it has a strong TW. A polarization of valley occurs, this giving rise to a beam splitting of the electronic beams belonging to different valleys (Fig. 6.10(b),(c)).

In Fig. 6.11(a) we show current versus voltage for: normal transmission, observing that the beams are totally separated at moderate voltages (zero current for normal transmission), and at angle of transmission $\theta_t = 12.7°$ showing a valley-polarized peak at high voltages. A realistic transmission probability for the beam splitter is shown in Fig. 6.11(b). We observed that the high transmission obtained for low energies [107] is conserved when TW term is included. The two beams obtained for a potential $V_2 = -1.5eV$ (TW case) 25.4° apart from each other for maximum of transmission.

A different situation occurs if the interface is parallel to the armchair orientation. In this configuration,(Fig. 6.9(b)) the beam of one valley is strongly collimated and waveguided (blue color in Fig. 6.10(c)) due to the flat portion of the isofrequency line. The other valley slightly disperses the beam. Due to the big difference of curvatures between the Dirac and the TW isoenergies, the allowed wavevectors **k** are situated in a zone of the TW isoline with small curvature involving a low dispersion (red color in Fig. 6.10(c)).

Let us make a comment on the possible experimental realization of the proposed device. Up to day, the most efficient way of identifying graphene samples is by optical contrast [115]. The maximum of this contrast depends both on the thickness of the substrate and on the wavelength of the monochromatic radiation used to illuminate the sample, usually in the visible range. For this range, the maximum contrast corresponds to a thickness of $300nm$ and the values reached for the chemical potential are of the order of $0.3eV$. However, it has been proposed [116] that another maximum in the contrast appears at a thickness of $90 - 100nm$. With this range, it is possible to get values of the chemical potential up to $0.6eV$, just in the threshold where the TW starts to be appreciable. The effect discussed here can then be effectively observed with minor experimental changes in current samples, namely, increasing the gate voltage and decreasing the substrate thickness. In large doping, the screening is efficient and Coulomb interaction can be neglected, so that one-particle model (Fermi liquid) is appropriate. The electron-electron Coulomb interaction could slightly distort the isoenergy lines as was shown both experimentally [117] and theoretically [118]. However this distortion only increases the separation of the beams.

6.9 Optical analogy

Control of beam propagation, collimation and focusing in PhC's is already well developed as discussed in previous chapters as well as in several works [119, 70, 71, 87, 120], thus one can assess the validity of the above analysis for graphene by putting forward its analogy with this photonic system. In fact, an optical analogy of the graphene system was previously described [121, 122]. We can realize it with a 2-D PhC with honeycomb, kagome or trigonal structure where the gap between the first and second bands is replaced by a Dirac point in the K point of symmetry. As an example, we have used a trigonal lattice, with parameter a_{PhC}, of air cylinders of radius $r = 0.33a_{PhC}$ inside a dielectric matrix with refractive index n (Fig. 6.12(a)). We notice that, in the case of the trigonal lattice, the Brillouin zone (BZ) (Fig. 6.12(b)) coincides with the real lattice, while in the graphene honeycomb lattice the BZ is rotated 30 degrees with respect to the real lattice, which implies that the zigzag and armchair situations described in graphene are exchanged in the PhC. Now we cannot change the light frequency throughout the crystal like we change the chemical potential in a transistor of field effect in graphene, but we can displace the frequency

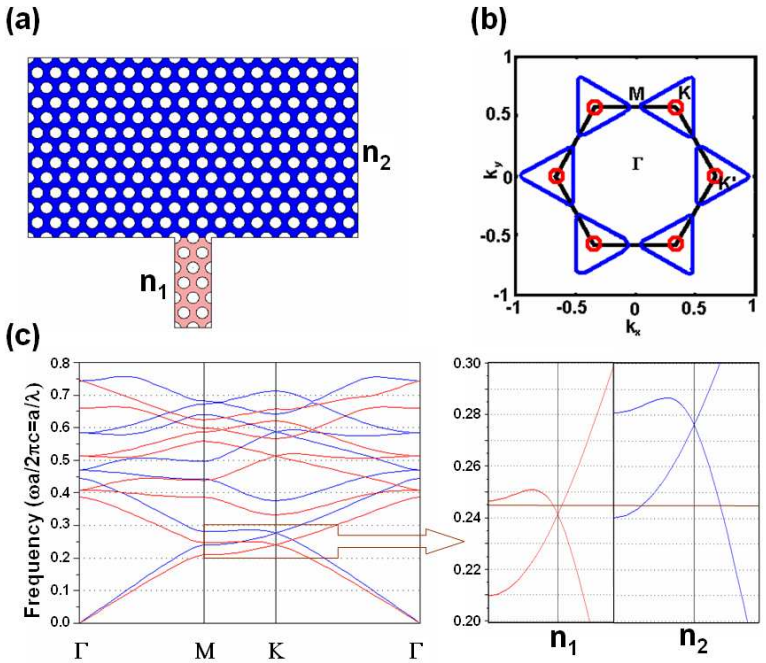

Figure 6.12: (a) Geometry of the trigonal photonic crystal (PC) of air holes and optical analogy of a p-n junction in graphene. (b) Brillouin zone and isofrequency lines for the two PCs for n_1 (red circles) and for n_2 (blue triangles). (c) Band diagram for a trigonal photonic crystal of air holes with radius $r = 0.33a_{PC}$ in a dielectric matrix with refractive index $n_1 = 3.04$ (red bands) and $n_2 = 2.65$ (blue bands). The two insets show details of the zone around the K point where we observe that for the wavelength $\lambda = 4.08a_{PC}$, n_1 corresponds to the conduction band, whereas n_2 is located at the TW valence band.

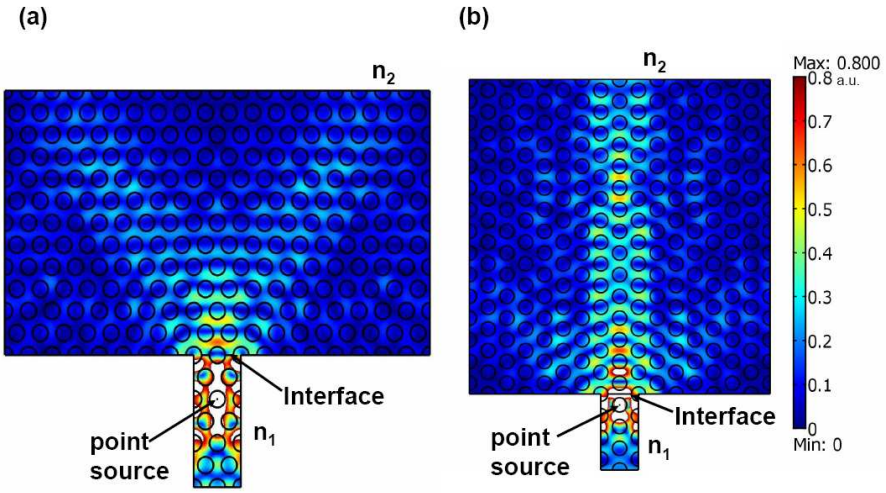

Figure 6.13: Maps of the electric field modulus of a wave originated at a point source located inside a photonic crystal with refraction index n_1 and propagating through another photonic crystal of dielectric matrix n_2. (a) Armchair orientation, illustrating the beam splitting of the two different valleys K and K'. (b) Zigzag orientation. We can see a collimation of the beams since the curvature in the trigonal distorted band is smaller than the one of the circular isoline in the proximity of the Dirac point. The angular dispersion is low.

position of the Dirac point in the band diagram by slightly varying the refractive index of the dielectric matrix (Fig. 6.12(c)). In this way, a junction of two PhCs with the same trigonal structure but with slightly different refractive index, mimics the field effect transistor in graphene.

Fig. 6.13 shows a finite elements numerical simulation (see appendix A) of the electric field modulus distribution from a point source, emitting TE polarized light (i.e. the electric field is parallel to the long axis of the air holes) with a wavelength $\lambda = 4.08a_{PhC}$ in a dielectric matrix with refractive index $n_1 = 3.04$ together with another PhC of the same structure but a slightly smaller refractive index $n_2 = 2.65$ for the two limiting cases: armchair (Fig. 6.13(a)) and zigzag (Fig. 6.13(b)). The creation of a beam splitter in the latter PhC for the armchair situation is illustrated by the fact that the two isofrequency curves in the K and K' points are triangles pointing in opposite directions from each other (right and left). Conversely, if we put the zigzag structure parallel to the interface, we obtain a collimation of the beams.

6.10 Conclusions

To summarize, this chapter describes how we have proposed an efficient way to get *valley polarized* beams using the trigonal warping effect in the graphene bands. We have shown a possible design of a beam splitter and a collimator device. This formation of valley polarized beams, is a key ingredient for the use of this new polarization in graphene as an effective information carrying degree of freedom. Besides, the transport properties of graphene can constitute a useful and novel device in future nanoelectronics. Finally, we have checked the validity of these phenomena, by means of an optical analogy with two dimensional photonic crystals and proposed a theory of isofrequency lines as a useful tool to simulate these kind of processes in graphene systems.

Appendix A

Numerical methods

A.1 Introduction

For the design and analysis of LHM's, numerical Maxwell solvers are highly valuable for two kinds of tasks, (1) the detailed analysis of various configurations containing LHM's and (2) the design of metamaterials exhibiting a negative index of refraction in a certain frequency range. The Maxwells equations can be numerically solved either in the time domain or in the frequency domain. Each method has its strong points and its disadvantages. The frequency domain method, which assumes that the time-dependence is harmonic, plays an important role in calculating the eigenstates and band structures of regular structures such as photonic crystals. On the other hand, the time domain method, which solves the time-dependent Maxwell equations directly on spatial grids, is well-suited for computing problems that involve the evolution of electromagnetic fields and for systems containing complex materials.

A.2 Finite elements method

The Finite Elements Method (FEM) is an old technique based on space discretization with unstructured meshes.It was first used for other disciplines of physics and closely related to variational integral formulations. In electrodynamics it became highly attractive when vector elements were introduced. We have used the commercial software implementation FEMLAB.

An important problem of all domain methods is the truncation of space. All commercial codes contain reasonable implementations of absorbing boundary conditions. Beside this, the main problem for FEM and similar methods with structured grids is the generation of appropriate grids, i.e., meshes. All modern FEM codes contain some automatic or even adaptive mesh generators. The quality of the results is heavily affected by the mesh generators. Fig. A.1 shows three different meshes obtained from FEMLAB the initial mesh is not sufficiently fine for obtaining accurate results,

after 3 automatic mesh refinement steps, the mesh is fine enough but it huge, which affects memory requirement and computation time. As one can see, the mesh is more or less uniformly refined and not mainly in those areas where the field is strong, i.e., along the LHM boundaries and near the focus points. FEMLAB allows the user to influence the mesh generation as also shown in Fig. A.1, but this is tedious work and requires some experience.

In addition to the mesh generator, the order of the elements and the matrix solver may heavily affect the accuracy of the results. This considerably depends on the loss of the LHM: The smaller the losses, the more problems are encountered.When the loss tangent for the complex permittivity and permeability is below $\epsilon = \mu = 0.01$ inaccurate results are also obtained with the direct matrix solvers that are much more robust. Then, very fine meshes are required and the computation time becomes extremely long since it grows with the cube of the nodes of the mesh for direct matrix solvers. Furthermore, one can see that inaccurate results are also obtained for first order elements. Note that the sparsity of the FEM matrix decays and the condition number increases with increasing order. Thus, iterative matrix solvers would work best for first order elements, but in this case the number of elements turns out to be too high for a computation on a personal computer. Since post-processing is relatively easy with FEMLAB, there is some noise due to the inaccuracy of the computation and this noise increases when the loss tangent decreases. Furthermore, the curves shown are not symmetric although the configuration is symmetric. This is also an effect of the inaccuracy of the results. Both effects cause difficulties when one wants to automatically extract position results by some numerical procedure.When the noise is too strong, such automatic procedures detect local minims at completely wrong positions.

Hence, upon analyzing several configurations, we have chosen a grid with a mesh growth rate of 1.55 and a mesh curvature factor of 0.65, where the geometrical resolution parameters consist of 10 vertices per edge by default. This configuration is adapted to the geometry and optimizes the convergence of the solution. The final mesh approximately has $50,000$ elements and $20,000$ nodes. To solve the elliptic Helmholtz equation, the Good Broyden iterative solver is employed. The convergence of this method is ensured on comparison of the nth-step solution in a new refined mesh with that of the previous iteration. We also verify with the tangential and normal boundary conditions of the magnetic field $\vec{H}$ [124] and the conservation of energy. Furthermore, we have checked calculations on comparing with the distribution of transmitted and reflected waves in cases already known of both left and right-handed materials. This determination of convergence is global, however the local errors are distinguishable by changing the number of elements in the mesh like for instance as reported in Ref. [64]. Also, we check that the FEM method used provides identical results to the Finite-difference time domain method which we explain next.

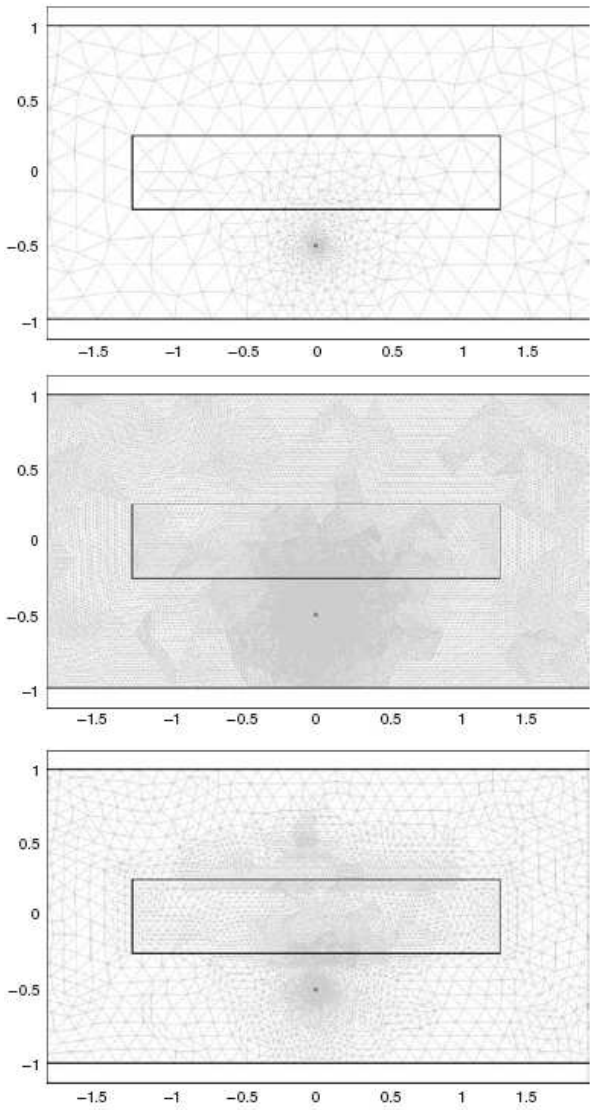

Figure A.1: Meshes for a rectangular LHM illuminated by a point source (below the rectangle) generated by the FEMLAB mesh generator. Top: Initial mesh, center: After 3 automatic mesh refinements, bottom with user-guided mesh refinement. After Ref. [123]

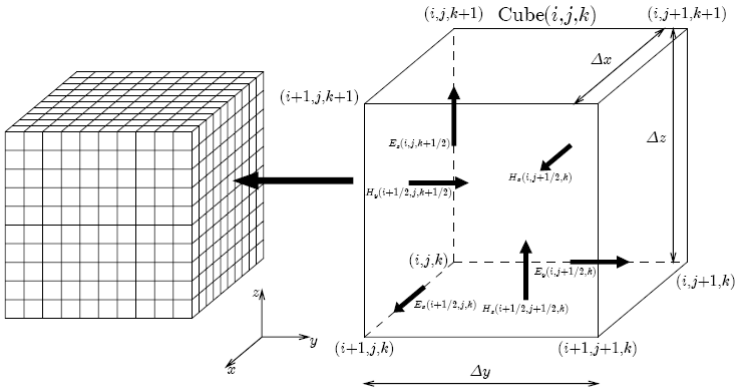

Figure A.2: Position of the electric and magnetic field vector components in a Yee cell.

A.3 Finite-difference time domain procedure

In 1966, Yee proposed a method to solve the time-dependent Maxwell equations using the finite-difference time domain (FDTD) technique [125]. In the FDTD technique the time dependent Maxwell equations are solved by propagating the electromagnetic fields in the time domain and by modelling the interaction of the electromagnetic fields with the medium. Since its introduction, the original algorithm has been refined and optimized for specific problems, but the concept has essentially stayed the same. Yee's algorithm solves for both the electric and magnetic fields in time and space using the coupled Maxwells curl equations, rather than solving for the electric or magnetic field alone using the wave equation. In Yee's algorithm the electric $\vec{E}$ and magnetic $\vec{H}$ field components in three-dimensional space are placed so that each $\vec{E}$ component is surrounded by four circulating $\vec{H}$ components and every $\vec{H}$ component is surrounded by four circulating $\vec{E}$ components (see Fig. A.2). In this way the electromagnetic fields are sampled in a highly efficient manner. The coordinates of the fields are labelled according to $(i, j, k) = (i\Delta x, j\Delta y, k\Delta z)$, where Δx, Δy and Δz are the mesh sizes for each dimension in this uniform, cubic lattice. By choosing this specific arrangement, the three-dimensional space lattice is effectively an interlinked array of Faradays Law and Ampere's Law contours [126] under the central-difference method. Yee's algorithm is flexible, robust, fast, easy to implement and is widely accepted as a reliable computational tool in computational electromagnetism. Despite the great success of the Yee−based FDTD algorithms, one limitation of them is that their stability is conditional, depending on the mesh size of the spatial discretization and the time step of the time integration [126, 127]. For the basic Yee algorithms in three-dimensional, the Courant factor, defined as $S = c\Delta t/|\Delta\vec{r}|$, where $|\Delta\vec{r}| = p(1/\Delta x)^2 + (1/\Delta y)^2 + (1/\Delta z)2$ and c denotes the velocity of light, must be

smaller than one to guarantee the stability of the algorithm [126, 127]. Therefore, a fine spatial mesh size $\Delta\vec{r}$ requires a fine time step Δt to maintain the desired accuracy.

As regards the FDTD used here is a commercial procedure (Fullwave [128]), the simulation was run until a stationary state was reached, which involved times $ct = 3000\mu m$. Time steps $\Delta t = a/1200$ where run with the space discretized into cells of side length $a/30 \times a/30$. Stability of the solution was checked for different discretization sizes. Absorbing boundary conditions (PML) are set at the boundaries of the calculation space.

Bibliography

[1] R.A. Shelby, D.R. Smith, and S. Schultz. Experimental verification of a negative index of refraction. *Science*, **292**:77, 2001.

[2] V.G. Veselago. The electrodynamics of substances with simultanenous negative values of ϵ and μ. *Sov. Phys. Usp.*, **10**:509, 1968.

[3] C. Caloz and T. Itoh. *Electromagnetic metamaterials : transmission line theory and microwave applications*. John Wiley & Sons, Inc, 2006.

[4] L.D. Landau and E.M. Lifshitz. *Electrodynamics of Continuous Media*. Oxford: Pergamon, 1975.

[5] L. Brillouin. *Wave Propagation and Group Velocity*. Academic Press, 1960.

[6] J.B. Pendry. Negative refraction makes a perfect lens. *Phys. Rev. Lett.*, **85**:3966, 2000.

[7] D. R. Smith, W. J. Padilla, D. C. Vier, S. C. Nemat-Nasser, and S. Schultz. Composite medium with simultaneously negative permeability and permittivity. *Phys. Rev. Lett.*, **84**:4184, 2000.

[8] J.B. Pendry. Negative refraction. *Contemp. Phys.*, **45**:191, 2004.

[9] J. B. Pendry and D.R. Smith. Reversing light with negative refraction. *Physics Today*, **57**:37, 2004.

[10] M. Born and E. Wolf. *Principles of Optics*. Cambridge University Press, 7th edition, 2002.

[11] J. D. Kraus and R. J. Marhefka. *Antennas*. McGraw Hill, 2001.

[12] J.S. Toll. Causality and the dispersion relation: Logical foundations. *Phys. Rev.*, **104**:1760, 1956.

[13] D. Hawley S. Zhu, A. W. Yu and R. Roy. Frustrated total internal reflection: a demonstration and review. *Am. J. Phys.*, **54**:601, 1986.

[14] C. K. Carniglia and L. Mandel. Quantization of evanescent electromagnetic waves. *Phys. Rev. D*, **3**:280, 1971.

[15] R. Ruppin. Surface polaritons of a left-handed material slab. *J. Phys.: Condens. Matter*, **13**:1811, 2001.

[16] N. Garcia and M. Nieto-Vesperinas. Left-handed materials do not make a perfect lens. *Phys. Rev. Lett.*, **88**:207403, 2002.

[17] M. Nieto-Vesperinas. Problem of image superresolution with a negative-refractive-index slab. *J. Opt. Soc. Am. A*, **21**:491, 2004.

[18] N. Fang, H. Lee, C. Sun, and X. Zhang. Sub-diffracction-limited optical imaging with a silver superlens. *Science*, **308**:534, 2005.

[19] D. O. S. Melville, R. J. Blaikie, and C. R. Wolf. Submicron imaging with a planar silver lens. *Appl. Phys. Lett.*, **84**:4403, 2004.

[20] R. J. Blaikie and D. O. S. Melville. Imaging through planar silver lenses in the optical near field. *J. Opt. A: Pure Appl. Opt.*, **S176**:2005, 7.

[21] M. M. Alkaisi, R. J. Blaikie, S. J. McNab, R. Cheung, and D. R. S. Cumming. Sub-diffraction-limited patterning using evanescent near-field optical lithography. *Appl. Phys. Lett.*, **75**:3560, 1999.

[22] D. Melville and R. Blaikie. Super-resolution imaging through a planar silver layer. *Opt. Express*, **13**:2127, 2005.

[23] Z.W. Liu, S. Durant, H. Lee, Y. Pikus, N. Fang, Y. Xiong, C. Sun, and X. Zhang. Far-field optical superlens. *Nano Lett*, **7**:403, 2007.

[24] Z. Liu, H. Lee, Y. Xiong, C. Sun, and X. Zhang. Far-field optical hyperlens magnifying sub-diffraction-limited objects. *Science*, **315**:1686, 2007.

[25] J.D. Jackson. *Classical Electrodynamics*. New York: Wiley, 1975.

[26] M. Nieto-Vesperinas. *Scattering and Diffraction in Physical Optics*. World Scientific Publishing Co. Pte. Ltd., 2006.

[27] M.I. Stockman. Criterion for negative refraction with low optical losses from a fundamental principle of causality. *Phys. Rev. Lett.*, **98**:177404, 2007.

[28] J. B. Pendry, A. J. Holden, W. J. Stewart, and I. Youngs. Extremely low frequency plasmons in metallic mesostructures. *Phys. Rev. Lett.*, **76**:4736, 1996.

[29] D. F. Sievenpiper, M. E. Sickmiller, and E. Yablonovitch. 3d wire mesh photonic crystals. *Phys. Rev. Lett.*, **76**:2480, 1996.

[30] S. Linden, C. Enkrich, G. Dolling, M.W. Klein, T. Koschny J. F. Zhou, C.M. Soukoulis, S. Burger, F. Schmidt, and M. Wegener. Photonic metamaterials: Magnetism at optical frequencies. *IEEE J. Sel. Top. Quant.*, **12**:1097, 2006.

[31] M. C. K. Wiltshire, J. B. Pendry, I. R. Young, D. J. Larkman, D. J. Gilderdale, and J. V. Hajnal. Microstructured magnetic materials for rf flux guides in magnetic resonance imaging. *Science*, **291**:849, 2001.

[32] www.nanotechnology.bilkent.edu.tr/researchhanded.htm.

[33] T. J. Yen, W. J. Padilla, N. Fang, D. C. Vier, D. R. Smith, J. B. Pendry, D. N. Basov, and X. Zhang. Terahertz magnetic response from artificial materials. *Science*, **303**:1494, 2004.

[34] S. Linden, C. Enkrich, M. Wegener, J. Zhou, T. Koschny, and C. M. Soukoulis. Magnetic response of metamaterials at 100 terahertz. *Science*, **306**:1351, 2004.

[35] C. Enkrich, M. Wegener, S. Linden, S. Burger, L. Zschiedrich, F. Schmidt, J. Zhou, T. Koschny, and C.M. Soukoulis. Magnetic metamaterials at telecommunication and visible frequencies. *Phys. Rev. Lett.*, **95**:203901, 2005.

[36] J. Valentine, S. Zhang, T. Zentgraf, E. Ulin-Avila, D. A. Genov, G. Bartal, and X. Zhang. Three−dimensional optical metamaterial with a negative refractive index. *Nature*, **455**:376, 2008.

[37] W. J. Padilla, D. N. Basov, and D. R. Smith. Electromagnetic metamaterials for negative refractive index. *Materials Today*, **9**:28, 2006.

[38] K. Aydin, K. Guven, M. Kafesaki, L. Zhang, C. M. Soukoulis, and E. Ozbay. Experimental observation of true left-handed transmission peaks in metamaterials. *Opt. Lett.*, **29**:2623, 2004.

[39] S. Zhang, W. Fan, B. K. Minhas, A. Frauenglass, K. J. Malloy, and S. R. J. Brueck. Midinfrared resonant magnetic nanostructures exhibiting a negative permeability. *Phys. Rev. Lett.*, **94**:037402, 2005.

[40] S. Zhang, W. Fan, K. J. Malloy, S. R. J. Brueck, N.C. Panoiu, and R.M. Osgood. Near−infrared double negative metamaterials. *Opt. Express*, **13**:4922, 2005.

[41] D. Schurig, J. J. Mock, B. J. Justice, S. A. Cummer, J. B. Pendry, A. F. Starr, and D. R. Smith. Metamaterial electromagnetic cloak at microwave frequencies. *Science*, **314**:977, 2006.

[42] M. Rahm, D. A. Roberts, J. B. Pendry, and D. R. Smith. Transformation-optical design of adaptive beam bends and beam expanders. *Opt. Express*, **16**:11555, 2008.

[43] S. Enoch, G. Tayeb, P. Sabouroux, N. Guerin, and P. Vincent. A metamaterial for directive emission. *Phys. Rev. Lett.*, **89**:213902, 2002.

[44] G. V. Eleftheriades, A. K. Iyer, and P. C. Kremer. Planar negative refractive index media using periodically l-c loaded transmission lines. *IEEE trans. Microwave Theory Tech.*, **50**:2702, 2002.

[45] A.K. Iyer, P.C. Kremer, and G.V. Eleftheriades. Experimental and theoretical verification of focusing in a large, periodically loaded transmission line negative refractive index metamaterial. *Opt. Express* **11**, 696 (2003).

[46] A. Grbic and G. V. Eleftheriades. Experimental verification of backward-wave radiation from a negative refractive index metamaterial. *J. Appl. Phys*, **92**:5930, 2002.

[47] A. Grbic and G. V. Eleftheriades. Growing evanescent waves in negative-refractive-index transmission-line media. *Appl. Phys. Lett.*, **82**:1815, 2003.

[48] A. Grbic and G. V. Eleftheriades. Subwavelength focusing using a negative-refractive-index transmission line lens. *IEEE Antennas Wireless Propagat. Lett.*, **2**:186, 2003.

[49] A. Grbic and G.V. Eleftheriades. Overcoming the diffraction limit with a planar left-handed transmission-line lens. *Phys. Rev. Lett.*, **92**:117403, 2004.

[50] S.C. Nemat-Nasser R.A. Shelby, D.R. Smith and S. Schultz. Microwave transmission through a two-dimensional, isotropic, left-handed metamaterial, *Appl. Phys. Lett.* **78,** 489-91 (2001).

[51] J.B. Pendry, A.J. Holden, D.J. Robbins, and W.J. Stewart. Magnetism from conductors and enhanced nonlinear phenomena, *IEEE Trans. Microwave Theory Tech.* **47**, 2075-2074 (1999).

[52] P.Markos and C.M. Soukoulis. Transmission studies of left-handed materials, *Phys. Rev. B* **65**, 033401 (2001).

[53] P. Markos and C.M. Soukoulis. Numerical studies of left-handed materials and arrays of split ring resonators, Phys. Rev. E 65, 036622 (2002).

[54] R.W. Ziolkowski and E. Heyman. Wave propagation in media having negative permittivity and permeability, *Phys. Rev. E* **64**, 056625 (2001).

[55] N.Garcia and M.Nieto-Vesperinas. Is there an experimental verification of a negative index of refraction yet? *Opt. Lett.*, **27**:885, 2002.

[56] P.M. Valanju, R.M.Walser, and A.P. Valanju. Wave refraction in negative-index media: always positive and very inhomogenous, *Phys. Rev. Lett.* **91**, 187401 (2002).

[57] M.W. McCall, A. Lakhtakia, and W.S. Weiglhofer. The negative index of refraction demystified, *European Journal of Physics*, **23,** 353 - 359, (2002).

[58] .G. Parazzoli, R.B. Greegor, K. Li, B.E.C. Koltenbach, and M. Tanielian. Experimental verification and simulation of negative index of refraction using Snell's law. *Phys. Rev. Lett.*, **90**:107401, 2003.

[59] R.B. Greegor, C.G. Parazzoli, K. Li, and M.H. Tanielian. Origin of dissipative losses in negative index of refraction materials, *Appl. Phys. Lett.* **82**, 2356-2358 (2003).

[60] A.A. Houck, J.B. Brock, and I.L. Chuang. Experimental observations of a left-handed material that obeys Snell's law. *Phys. Rev. Lett.*, **90**:137401, 2003.

[61] J.B. Pendry. Comment on "Left-handed materials do not make a perfect lens," *Phys. Rev. Lett.* **91**, 099701 (2003).

[62] M. Nieto-Vesperinas and N. Garcia. Nieto-Vesperinas and Garcia reply, *Phys. Rev. Lett.* **91**, 099702 (2003).

[63] A.L. Pokrovsky and A.L. Efros. Electrodynamics of metallic photonics crystals and the problem of left-handed materials, *Phys. Rev. Lett.* **89**, 093901 (2002).

[64] P. Kolinko and D.R. Smith. Numerical study of electromagnetic waves interacting with negative index materials, *Opt. Express* **11**, 640-648 (2003), http://www.opticsexpress.org/abstract.cfm?URI=OPEX-11-7-640.

[65] D.R. Smith, D. Schurig, M. Rosenbluth, S. Schultz, S.A. Ramakrishna, and J.B. Pendry. Limitations on sub-diffraction imaging with a negative refractive index slab. *Appl. Phys. Lett.*, **82**:1506, 2003.

[66] A.A. Houck. Harvard University, Department of Physics, Cambridge, Massachusetts 02138 (personal communication, 2003).

[67] J.W. Goodman. *Intoduction to Fourier Optics*. New York: McGraw-Hill, 1968.

[68] C. Luo, S. G. Johnson, J. D. Joannopoulos, and J.B. Pendry. Subwavelength imaging in photonic crystals. *Phys. Rev. B*, **68**:045115, 2003.

[69] J. L. Garcia-Pomar and M. Nieto-Vesperinas. Transmission study of prisms and slabs of lossy negative index media. *Opt. Express*, **12**:2081, 2004.

[70] M. Notomi. Theory of light propagation in strongly modulated photonic crystals: Refractionlike behavior in the vicinity of the photonic band gap. *Phys. Rev. B*, **62**:1069, 2000.

[71] X. Wang, Z.F. Ren, and K. Kempa. Improved superlensing in two-dimensional photonic crystals with a basis. *Appl. Phys. Lett.*, **86**:061105, 2004.

[72] T. Decoopman, G. Tayeb, S. Enoch, D. Maystre, and B. Gralak. Photonic crystal lens: From negative refraction and negative index to negative permittivity and permeability. *Phys. Rev. Lett.*, **97**:073905, 2006.

[73] A.L. Efros, C. Y. Li, and A. L. Pokrovsky. Evanescent waves in photonic crystals and image of Veselago lens. *cond-mat/0503494*, 2005.

[74] R. Moussa, S. Foteinopoulou, L. Zhang, G. Tuttle, K. Guven, E. Ozbay, and C. M. Soukoulis. Negative refraction and superlens behavior in a two-dimensional photonic crystal. *Phys. Rev. B*, **71**:085106, 2005.

[75] F. Ramos-Mendieta and P. Halevi. Surface electromagnetic waves in two-dimensional photonic crystals: Effect of the position of the surface plane. *Phys. Rev. B*, **59**:15112, 1999.

[76] W. M. Robertson, G. Arjavalingam, R. D. Meade, K. D. Brommer, A. M. Rappe, and J. D. Joannopoulos. *Opt. Lett.*, **18**:528, 1993.

[77] R. D. Meade, K. D. Brommer, A. M. Rappe, and J. D. Joannopoulos. *Phys. Rev. B*, **44**:10961, 1991.

[78] E. Cubukcu, K. Aydin, E. Ozbay, S. Foteinopolou, and C.M. Soukoulis. Subwavelength resolution in a two-dimensional photonic-crystal-based superlens. *Phys. Rev. Lett.*, **91**:207401, 2003.

[79] C. Luo, S.G. Johnson, J.D. Joannopoulos, and J.B. Pendry. All-angle negative refraction without negative effective index. *Phys. Rev. B*, **65**:201104, 2002.

[80] H-T. Chien, H-T. Tang, C-H. Kuo, C-C. Chen, and Z. Ye. Directed diffraction without negative refraction. *Phys. Rev. B*, **70**:113101, 2004.

[81] W. M. Robertson, G. Arjavalingam, R. D. Meade, K. D. Brommer, A. M. Rappe, and J. D. Joannopoulos. Measurement of the photon dispersion relation in two-dimensional ordered dielectric arrays. *J.Opt.Soc.Am. B*, **10**:322, 1993.

[82] F. Goos and H. Hänchen. *Ann. Physik* **436**, 333 (1947); *Ann. Physik* **5**, 251-252 (1949); C. Imbert and Y. Levy, *Nouv. Rev. Opt.* **6**, 285 (1975); F. Bretenaker, A. L. Floch, and L. Dutriaux, *Phys. Rev. Lett.* **68**, 931 (1992); K. Artmann, *Ann. Phys.* **2**, 87 (1948); H. K. V. Lotsch, *J. Opt. Soc. Am.* **58**, 551 (1968); H.

R. Horowitz and T. Tamir, *J. Opt. Soc. Am.* **61**, 586 (1971); F. Falco and T. Tamir, *J. Opt. Soc. Am. A* **7**, 185 (1990); J. J. Crowan and B. Anicin, *J. Opt. Soc. Am.* **67**, 1307 (1977); M. Wong, G. E. Reesor, and L. A. A. Read, *Can.J. Phys.* **55**, 1061 (1977); J. Ptich, *Ann. Phys.* **3**, 433 (1929); *Optik* **12**, 41 (1955); R. H. Renard, *J. Opt. Soc. Am.* **54**, 1190 (1964).

[83] D. Felbacq, A. Moreau, and R. Smaâli. Goos-Hänchen effect in the gaps of photonic crystals. *Opt. Lett*, **28**:1633, 2003.

[84] D. Felbacq and R. Smaâli. Bloch modes dressed by evanescent waves and the generalized Goos-Hänchen effect in photonic crystals. *Phys. Rev. Lett*, **92**:193902, 2004.

[85] K. Iizuka. *Elements of Photonics, Volume I: In Free Space and Special Media.* John Wiley & Sons, Inc, 2002.

[86] J.L. Garcia-Pomar, J. Gollub, A. Thapa, D.R. Smith, and M. Nieto-Vesperinas. Experimental visualization of total internal reflection beam lateral shift in a self-collimated photonic crystal. *to be published.*

[87] J.L. Garcia-Pomar and M. Nieto-Vesperinas. Waveguiding, collimation and subwavelength concentration in photonic crystals. *Opt. Express*, **13**:7997, 2005.

[88] F. Ramos-Mendieta and P. Halevi. Surface electromagnetic waves in two-dimensional photonic crystals: Effect of the position of the surface plane. *Phys. Rev. B*, **59**:15112, 1999.

[89] W. M. Robertson, G. Arjavalingam, R. D. Meade, K. D. Brommer, A. M. Rappe, and J. D. Joannopoulos. Observation of surface photons on periodic dielectric arrays. *Opt. Lett.*, **18**:528, 1993.

[90] R. D. Meade, K. D. Brommer, A. M. Rappe, and J. D. Joannopoulos. Electromagnetic Bloch waves at the surface of a photonic crystal. *Phys. Rev. B*, **44**:10961, 1991.

[91] E. Moreno, F. J. García-Vidal, and L. Martín-Moreno. Enhanced transmission and beaming of light via photonic crystal surface modes. *Phys. Rev. B*, **69**:121402(R), 2004.

[92] P. Kramper, M. Agio, C. M. Soukoulis, A. Birner, F. Muller, R. B. Wehrspohn, U. Gosele, and V. Sandoghdar. Highly directional emission from photonic crystal waveguides of subwavelength width. *Phys. Rev. Lett.*, **92**:113903, 2004.

[93] T. Hashimoto and T. Yoshino. Optical heterodyne sensor using the Goos-Hänchen shift. *Opt. Lett.*, **14**:913, 1989.

[94] L. Wu, M. Mazilu, T. Karle, and T. F. Krauss. Superprism phenomena in planar photonic crystals. *IEEE Journal of Quantum Electronics*, **38**:915, 2002.

[95] H. Kosaka, T. Kawashima, A. Tomita, M. Notomi, T. Tamamura, T. Sato, and S. Kawakami. Superprism phenomena in photonic crystals. *Phys. Rev. B*, **50**:10096R, 1998.

[96] S. Y. Lin, V. M. Hietala, L. Wang, and E. D. Jones. Highly dispersive photonic band-gap prism. *Opt. Lett.*, **21**:1771, 1996.

[97] Z.Y. Li and L.L. Lin. Evaluation of lensing in photonic crystal slabs exhibiting negative refraction. *Phys. Rev. B*, **68**:245110, 2003.

[98] D.J. Bergman and M.I. Stockman. Surface plasmon amplification by stimulated emission of radiation: Quantum generation of coherent surface plasmons in nanosystems. *Phys. Rev. Lett.*, **90**:027402, 2003.

[99] N.I. Zheludev, S.L. Prosvirnin, N. Papasimakis, and V.A. Fedotov. Coherent metamaterials and the lasing spaser. *Nature Photonics*, in press, 2008.

[100] W. Schäfer and M. Wegener. *Semiconductor Optics and Transport Phenomena*. Springer, New York, 2002.

[101] V.M. Shalaev. "Optical negative-index metamaterials", *Nature Photon.* **1**, 41 (2007).

[102] K. Busch, G. von Freymann, S. Linden, S. Mingaleev, L. Tkeshelashvili, and M. Wegener. "periodic nanostructures for photonics". *Phys. Rep*, **444**:101–202, 2007.

[103] M.W. Klein, T. Tritschler, M. Wegener, and S. Linden. Lineshape of harmonic generation on metal nanoparticles and metallic photonic crystal slabs. *Phys. Rev. B*, **72**:115113, 2005.

[104] S.W. Koch W.W. Chow and M. Sargent III. *Semiconductor-Laser Physics*. Springer, New York, 1994.

[105] K. S. Novoselov, A. K. Geim, S. V. Morozov, D. Jiang, M. I. Katsnelson, I. V. Grigorieva, S. V. Dubonos, and A. A. Firsov. Two-dimensional gas of massless Dirac fermions in graphene. *Nature*, **438**:197, 2005.

[106] A. Fasolino, J. H. Los, and M. I. Katsnelson. Intrinsic ripples in graphene. *arXiv.org:cond-mat/0704.1793*, 2007.

[107] M. I. Katsnelson, K. S. Novoselov, and A. K. Geim. Chiral tunneling and the Klein paradox in graphene. *Nature Physics*, **2**:620, 2006.

[108] V. V. Cheianov, V. Fal'ko, and B. L. Altshuler. Veselago lens for electrons: Focusing and caustics in graphene p-n junctions. *Science*, **315**:1252, 2006.

[109] A. Rycerz, J. Tworzydło, and C. W. J. Beenakker. Valley filter and valley valve in graphene. *Nature Physics*, **3**:172, 2007.

[110] R. Saito, G. Dresselhaus, and M. S. Dresselhaus. Trigonal warping effect of carbon nanotubes. *Phys. Rev. B.*, **61**:2981, 2000.

[111] P. R. Wallace. The band theory of graphite. *Phys. Rev.*, **71**:622, 1947.

[112] A. H. Castro Neto, F. Guinea, N. M. R. Peres, K. S. Novoselov, and A. K. Geim. The electronic properties of graphene. *arXiv:0709.1163v2*, 2008.

[113] V. V. Cheianov and V. I. Falk'o. Selective transmission of dirac electrons and ballistic magnetoresistance of *n-p* junctions in graphene. *Phys. Rev. B*, 74:041403(R), 2006.

[114] S. Y. Zhou, G.-H. Gweon, J. Graf, A. V. Fedorov, C. D. Spataru, R. D. Diehl, Y. Kopelevich, D.-H. Lee, Steven G. Louie, and A. Lanzara. First direct observation of dirac fermions in graphite. *Nature Physics*, **2**:595, 2006.

[115] K. S. Novoselov, A. K. Geim, S. V. Morozov, D. Jiang, Y. Zhang, S. V. Dubonos, I. V. Grigoreva, and A. A. Fisov. Electric field effect in atomically thin carbon films. *Science*, **306**:666, 2004.

[116] P. Blake, K. S. Novoselov, A. H. Castro Neto, D. Jiang, R. Yang, T. J. Booth, A. K. Geim, and E. W. Hill. Making graphene visible. *Appl. Phys. Lett.*, **91**:063124, 2007.

[117] J.L. McChesney, A. Bostwick, T. Ohta, K. V. Emtsev, T. Seyller, K. Horn, and E. Rotenberg. Massive enhancement of electron-phonon coupling in doped graphene by an electronic singularity. *arXiv:0705.3264*, 2007.

[118] R. Roldan, M. P. Lopez-Sancho, and F. Guinea. Effect of electron-electron interaction on the Fermi surface topology of doped graphene. *Phys. Rev. B*, **77**:115410, 2008.

[119] H. Kosaka, T. Kawashima, A. Tomita, M. Notomi, T. Tamamura, T. Sato, and S. Kawakami. Self-collimating phenomena in photonic crystals. *Appl. Phys. Lett.*, **74**:1212, 1999.

[120] P. T. Rakich, M. S. Dahlem, S. Tandon, M. Ibanescu, M. Soljac, G. S. Petrich, J. D. Joannopoulos, L. A. Kolodziejski, and E. P. Ippen. Achieving centimetre-scale supercollimation in a large-area two-dimensional photonic crystal. *Nature Materials*, **5**:93, 2006.

[121] F.D.M. Haldane and S. Raghu. "one-way waveguides": Analogs of quantum Hall edge-states in photonic crystals. *arXiv.org:cond-mat/0503588*, 2005.

[122] R. A. Sepkhanov, Ya. B. Bazaliy, and C. W. J. Beenakker. Extremal transmission at the Dirac point of a photonic band structure. *Phys. Rev. A.*, **75**:063813, 2007.

[123] V. Veselago, L. Braginsky, V. Shklover, and C. Hafner. Negative refractive index materials. *J. Comput. Theor. Nanoscience*, **3**:1, 2006.

[124] C. Caloz, C.-C. Chang, and T. Itoh. Full-wave verification of the fundamental properties of left-handed materials in waveguide configurations. *J.Appl.Phys.*, **90**:5483, 2001.

[125] K. S. Yee. Numerical solution of initial boundary value problems involving Maxwell's equations. *IEEE Trans. Antennnas Prop.*, **14**:1966, 302.

[126] A. Taflove and S. C. Hagness. *Computational Electrodynamics - The Finite-Difference Time-Domain Method*. Artech House, Boston, 2005.

[127] K. S. Kunz and R. J. Luebbers. *Finite-Difference Time-Domain Method for Electromagnetics*. CRC Press, 1993.

[128] Fullwave©. *w*ww.rsoftonic.com.